

Description of Gauge Theory Phenomena from Topological Objects

A Dissertation presented

by

Rasmus Normann Larsen

to

The Graduate School

in Partial Fulfillment of the

Requirements

for the Degree of

Doctor of Philosophy

in

Physics

Stony Brook University

August 2017

Stony Brook University

The Graduate School

Rasmus Normann Larsen

We, the dissertation committee for the above candidate for the

Doctor of Philosophy degree, hereby recommend

acceptance of this dissertation

**Edward Shuryak - Dissertation Advisor
Distinguished Professor, Department of Physics**

**Jacobus Verbaarschot - Chairperson of Defense
Professor, Department of Physics**

Roy Lacey, Adjunct Professor, Department of Chemistry

Robert D. Pisarski, Senior Scientist, Nuclear Theory Group, BNL

This dissertation is accepted by the Graduate School

Charles Taber
Dean of the Graduate School

Abstract of the Dissertation

Description of Gauge Theory Phenomena from Topological Objects

by

Rasmus Normann Larsen

Doctor of Philosophy

in

Physics

Stony Brook University

August 2017

We explore two of the most interesting phenomena in gauge field theories, confinement and chiral symmetry breaking, using an ensemble of 64 interacting instanton-dyons. Instanton-dyons are components of the finite temperature instantons with non-trivial Polyakov loop ($P \neq 1$). Classical dyon-antidyon interactions are obtained from the streamline approach and included in the ensemble. The dyon interactions with other dyons and with the vacuum drive the Polyakov loop towards the confining value $P = 0$.

There are N_c (Number of colors) types of dyons. Including fermions create fermionic zero modes on only one of the dyon types, and corrections to these zero modes introduce a linear attraction. Changing the boundary conditions of the fermions, change which types of dyons have the fermionic zero modes. This affects both confinement and chiral symmetry breaking.

From the interacting ensemble of instanton-dyons we numerically obtain the temperature dependence of the Polyakov loop in the quenched case (no fermions) and also the chiral condensates for the case of 2 standard fermions and for the case of 1 periodic and 1 anti-periodic fermion, all for 2 colors. We find that as temperature decreases the ensemble tries to maximize the entropy by making the size of M and L dyons the same. This forces the Polyakov loop towards the confining value and the densities of the dyons toward the

same density. This increases the range of the fermionic zero modes, which together with the increased densities, create a non-zero chiral condensate. Changing the boundary condition of one of the two fermions to periodic, restores center symmetry and results in chiral symmetry never being restored. We thus find that the mechanisms that drive the confinement-deconfinement and chiral symmetry breaking transitions are different, but related to each other through the interactions of the instanton-dyons.

Table of Contents

Contents

1	Introduction	1
2	Path integral and Topological Objects	6
2.1	Path integral in QCD	6
2.2	Classical solutions	7
2.3	Axial and Vector Symmetry	9
2.4	Zero modes	10
2.4.1	Bosonic zero modes	10
2.4.2	Fermionic zero modes	11
2.5	Calorons and Dyons	12
2.5.1	Zero modes of the dyons	15
2.5.2	Dyons and antidyons	17
2.6	Quantum Weight of the caloron	17
2.7	Ensemble of dyons	19
3	Programming	20
3.1	Graphic Processing Unit	20
3.2	c++	21
3.3	CUDA	22
3.3.1	Memory	22
3.3.2	Functions	23
3.4	Programs	26
3.4.1	Gradient Flow	26
3.4.2	Interacting Ensemble	27
3.4.3	Single and Double precision	29
3.5	The Metropolis Algorithm	29
4	Classical dyon interactions	31
4.1	The setting	31
4.1.1	Instanton-dyons and their superposition	31
4.1.2	The gradient flow	34
4.2	Dyons on the lattice	34
4.2.1	The gauge fields	34

4.2.2	Lattice details	37
4.3	Results	38
4.3.1	Qualitative features of the streamline	38
4.3.2	Parameterization of the M and \bar{M} Streamline	40
4.3.3	Details of the Streamline	44
4.3.4	$L\bar{L}$ pairs	50
5	Ensemble of Instanton-Dyons	53
5.1	An excluded volume model	53
5.2	The instanton-dyon interactions	58
5.3	The setup	60
5.4	The dyon weights in the partition function	62
5.5	Units and holonomy	64
5.6	The dyon back reaction: holonomy potential	65
5.7	Self Consistency	68
5.8	The physical results	69
5.9	Possible improvements	75
6	Dyons and Fermions	80
6.1	The Zero Mode Zone	81
6.1.1	The hopping amplitudes	82
6.2	The general setting	83
6.3	Eigenvalue distributions and the chiral condensate	86
6.3.1	The finite size effects	88
6.3.2	The effect of the quark mass	91
6.3.3	Gaps of the eigenvalue distribution	92
6.4	Data and analysis	93
6.4.1	Data Analysis	94
6.5	Physical Results	95
6.5.1	Parameterization A for T_{ij}	96
6.5.2	Parameterization B for T_{ij}	100
7	Dyons and Boundary conditions	105
7.1	Z_{N_c} -symmetric QCD and the instanton-dyons	105
7.2	The setting of the simulations	106
7.3	The holonomy potential and confinement	109
7.4	Chiral symmetry breaking	113
7.4.1	Dirac eigenvalue distribution	116

Acknowledgements

The text of this dissertation contains in part material published by me together with Edward Shuryak in [1, 2, 3, 4]

Section 4 contains material published in [1]:

R. Larsen and E. Shuryak, “Classical interactions of the instanton-dyons with antidyons,” Nucl. Phys. A **950**, 110 (2016) doi:10.1016/j.nuclphysa.2016.03.013 [arXiv:1408.6563 [hep-ph]].

Section 5 contains material published in [2]:

R. Larsen and E. Shuryak, “Interacting ensemble of the instanton-dyons and the deconfinement phase transition in the SU(2) gauge theory,” Phys. Rev. D **92**, no. 9, 094022 (2015) doi:10.1103/PhysRevD.92.094022 [arXiv:1504.03341 [hep-ph]].

Section 6 contains material published in [3]:

R. Larsen and E. Shuryak, “Instanton-dyon Ensemble with two Dynamical Quarks: the Chiral Symmetry Breaking,” Phys. Rev. D **93**, no. 5, 054029 (2016) doi:10.1103/PhysRevD.93.054029 [arXiv:1511.02237 [hep-ph]].

Section 7 contains material published in [4]:

R. Larsen and E. Shuryak, “Instanton-dyon ensembles with quarks with modified boundary conditions,” Phys. Rev. D **94**, no. 9, 094009 (2016) doi:10.1103/PhysRevD.94.094009 [arXiv:1605.07474 [hep-ph]].

Acknowledgements. I would like to thank T. Iritani for useful discussions. This work was supported in part by the U.S. D.O.E. Office of Science, under Contract No. DE-FG-88ER40388.

1 Introduction

Topological objects in euclidean gauge theories are solutions to the equation of motion. The most well known solutions are the instantons [5] which are 4-dimensional topological objects in $SU(N_c)$ theories. The standard approach of perturbation theory assumes that the only local ~~minima~~ is that of all fields equal to zero. This is not true when topological objects are present. The fact that the objects are solutions to the equation of motion, means that one has to include expansions around these objects also.

minimum of the action

The topological charge of the instantons require, according to the Atiyah - Singer index theorem [6], that the objects should have fermionic zero modes. This was shown by 't Hooft [7, 8] for instantons to lead to effective interactions that explicitly break the axial $U_A(1)$ symmetry, and thus solves the question of why the η' is so much heavier than the Goldstone bosons (π , K , η). This does not explain the spontaneous breaking of $SU_A(N)$ chiral symmetry. To understand the spontaneous breaking of $SU_A(N)$ chiral symmetry, the Interacting Instanton Liquid Model (IILM) was developed in the 90s (See [9] for a review). The important part in the breaking of $SU_A(N)$ was a collective interaction of all the instantons in the ensemble, creating small fermionic eigenvalues. This picture is supported by lattice works [10, 11], where removing the smallest eigenvalues, which are much smaller than the typical scale of the particles, restores both $SU_A(N_f)$ and $U_A(1)$ chiral symmetries.

While instantons give a simple explanation for chiral symmetry breaking, i.e. the existence of zero modes, the objects cannot explain the finite temperature transition of confinement-deconfinement that happens around $200MeV$, dependent on the amount of colors and flavors. Confinement can be seen in different ways, one is to say that no free quarks are observed, another is that the Wilson loops obey an area law, while another often used measure is to look at the expectation value of the Polyakov loop P

$$P = \frac{1}{N_c} \text{tr}[L] = \frac{1}{N_c} \text{tr}(\text{Path}[\exp(i \oint A_4 d\tau)]), \quad (1)$$

which is an order parameter for confinement in the quenched case. While one could argue that confinement and chiral symmetry breaking are unrelated and therefore that topological objects might be unrelated to confinement, it is remarkable how close the temperature of the two transitions are. This "coincidence" begs for an answer.

Several attempts to explain confinement from topological objects have been done. For instance in [12, 13] where solitons were used to show how they can disorder the vacuum such to create a Wilson loop that follows the area law. Other groups have looked at vortices [14] due to their simple explanation of the area law of the Wilson loop. It has been shown in [15] that certain vortices contain zero modes similar to instantons.

For this work, the main focus is on the finite temperature transitions, and trying to explain both the breaking of chiral symmetry and the confinement-deconfinement transition. In order to do this I have worked with topological objects at finite temperature in $SU(2)$ QCD. The first step towards the needed objects was done by [16] where the finite temperature instanton, the caloron, was found. This can be seen as an infinite amount of instantons sitting at a temporal separation of $1/T$ from each other, such that the solution becomes periodic in $1/T$, which is the standard way of introducing finite temperature in gauge theories for bosons. The next and more non-trivial step was done in [17, 18], who introduced a Higgs field into the solution through the non-zero expectation value of the A_4 field. The size of this non-zero A_4 field is normally referred to as the holonomy. This solution was based on the ADHM construction, where an infinite ~~dimension~~ vector is constructed, such that the field will be self-dual, which therefore at the same time will also be a solution to the equation of motion. The dimension of the vector is infinite since one needs the solution to be periodic. dimensional

This holonomy field is important, as it makes configurations with Polyakov loop expectation value different from one ($\langle P \rangle \neq 1$) possible. This is important, since as lattice studies has shown [19] the Polyakov loop needs to be close to zero, for the confined phase. These solutions made it possible to use the topological objects for any value of P , instead of only $P = 1$, as only was possible with the standard calorons.

The work done in [18] showed some surprising features of the caloron with non-trivial holonomy (i.e. $P \neq 1$). It was observed that the N_c (Number of colors) solution could be described by N_c positions, thus corresponding to N_c individual objects. When far separated from each other, the objects were shown to behave like they had both an electric and magnetic charge. For this reason the objects in this work is called instanton-dyons. Another name used in the literature is "BPS monopoles" [20], since the solutions are essentially the same as the monopoles due to a real Higgs potential, which was used in [21, 22]. This is important since these monopoles have in these papers, among others, been argued to be responsible for confinement. It is therefore

straightforward to imagine that the instanton-dyons (dyons for short) are responsible for both confinement through the monopole like behavior, and chiral symmetry breaking from the zero modes, due to being topological objects. Whether this is the case, is the main topic in this dissertation.

This idea has been studied in several papers. In [23] they showed how the dyons can disorder the Wilson loop and thus obtain the expected area law falloff. While interesting, this result was highly dependent on long range behavior, and is thus not very robust. Another explanation has been found in supersymmetric theories [20] where the instanton-dyons have been shown to produce confinement. This though rely on the cancellation of the fermionic and bosonic determinant, where the GPY potential (the cost in energy to introduce a non-zero expectation value of A_4) disappear, such that even small densities of dyons can cause confinement.

This work follows the same reasons, though we (me and my advisor Edward Shuryak), has looked at confinement through the change in holonomy, and not in the behavior of the Wilson loop. This change in the holonomy comes about due to the interactions between the dyons with other dyons and with the vacuum itself. This follows the same ideas as the Instanton Liquid Model which was done in the 90s[24, 25], though expanded in scope due to the inclusion of holonomy.

My work done on instanton-dyons has been focused on $SU(2)$, meaning two color QCD. The results have been published in [1, 2, 3, 4]. For $SU(2)$ the amount of dyons per caloron is 2. We call the dyons M and L and the antidyons \bar{M} and \bar{L} . L dyons are M dyons with holonomy $v \rightarrow 2\pi T - v$ which has been rotated by 2π in time, such that L dyons have anti-periodic fermionic zero modes, while M dyons have periodic fermionic zero modes.

The reason we work with dyons individually instead of the full caloron is that the different densities of M and L dyons are important in driving the confinement-deconfinement transition.

The dyons have been used in an ensemble in order to find the free energy of the system, and thus find the most likely configuration of the vacuum. While $A_\mu = 0$ has the lowest energy, the increase in possible configurations(entropy) leads to configurations where dyons dominate the vacuum. To find the specific configuration, we had to understand the interactions of the dyons first.

The interactions due to the leading order fluctuation around the dyons and the metric for LM pairs was done in [26] for $SU(2)$. Diakonov also proposed a more general form for the metric for many M and L dyons in

[27]. All of these results are only for dyons or antidyons, where classical interactions cancel. For interactions between dyons and antidyons, this is not the case, and no analytic formula exist. This problem was numerically solved for an instanton and an antiinstantons in [28]. For classical interactions of the dyons, this was calculated numerically in [1] by me and Edward Shuryak using the streamline approach, which is the subject in section 4.

These interactions have been fundamental in explaining confinement and chiral symmetry breaking using an ensemble of dyons, as we will see in section 5, 6 and 7. The fundamental part in these explanations are the increased density of dyons as the temperature decreases. At high temperatures, the GPY potential dominate, forcing the Polyakov loop towards the deconfining value of 1. For low temperatures the excluded volumes forces the Polyakov loop towards zero, though how this happens depend on the amount of quark flavors, the representation[29, 30, 31] and the boundary conditions.

The interacting dyon ensemble done in the papers [2, 3, 4] by me and Edward Shuryak follow the conceptual idea done in [32] of an excluded volume, though expands the model greatly, by simulating interactions, and by finding the density of the dyons from the simulation itself, instead of using data from lattice. Technically the ensemble follows the work done in [33], but expands the scope to include a description of confinement through the value of the Polyakov loop and by increasing the amount of configurations explored many fold.

Inclusion of fermionic interactions in the dyon ensemble was done by me and Edward Shuryak in [3] through corrections to the fermionic zero modes. The simulations at massless quarks, results in a linear attraction between L and \bar{L} dyons, due to the fermionic determinant being the product of all eigenvalues. The fermionic interactions and eigenvalue distribution were calculated by expanding in the set of fermionic zero modes of the dyons. From the eigenvalue distribution we obtained the chiral condensate which is the order parameter of chiral symmetry breaking, and is non-zero when chiral symmetry is broken. At finite volume, at which the simulation was performed at, one can not extract the chiral condensate from the limit of zero eigenvalue. The finite volume effect is explained by random matrix theory [34] and tells us that as the volume increases, a rift between zero and the eigenvalue distribution closes. Using this we obtained the chiral condensate as a function of temperature.

We have also explored what happens if one changes the boundary conditions of the fermions. This was inspired by the work done in [35] and later

also lattice work in [36]. In terms of dyons, this is interesting since there are N_c dyons for one caloron, but only one fermionic zero mode. Which dyon the zero mode sits on, depends on the boundary condition and the Polyakov loop. Changes to boundary conditions therefore are expected to change the behavior of both confinement and chiral symmetry breaking. If dyons indeed are responsible for these phenomena, then the interacting dyon ensemble should be able to describe this change to the theory. Me and Edward Shuryak did this in [4] for $SU(2)$ (see section 7), which qualitatively showed similar results to lattice[36] for $SU(3)$.

2 Path integral and Topological Objects

We will in this section introduce the objects and structures which we will need in order to understand how the instanton-dyon ensemble was done. We start by introducing the path integral at finite temperature in euclidean space, followed by the basic idea of topological objects/configurations. After that, the vector and axial part of the Lagrangian density is explained. We then explain what zero modes are and how they differ for bosons and fermions. Having shown the properties of topological object, we introduce the solution for instanton-dyons. The instanton-dyons are the main topological objects of interest in this work. Instanton-dyons appear only at finite temperature when we require the Polyakov loop to be non-trivial ($P \neq 1$). The contribution of one caloron to the path integral is shown. After this, we show the explicit form of the fermionic dyon zero modes. Last, we explain how the ensemble of dyons is constructed.

2.1 Path integral in QCD

The main object we want to study is the path integral in euclidean space

$$Z = \int D\bar{\psi}D\psi DA_\mu \exp(- \int d^4x \mathcal{L}(\bar{\psi}, \psi, A_\mu)). \quad (2)$$

The Lagrangian density \mathcal{L} is given as

$$\mathcal{L} = \bar{\psi}(\gamma_\mu D_\mu)\psi + \frac{1}{4g^2} F_{\mu\nu}^a F_{\mu\nu}^a \quad (3)$$

$$F_{\mu\nu} = \partial_\mu A_\nu^a - \partial_\nu A_\mu^a + f_{abc} A_\mu^b A_\nu^c \quad (4)$$

$$D_\mu = \partial_\mu - iA_\mu^a \tau_a, \quad (5)$$

where f_{abc} is the structure constant for $SU(N)$ that tells how the matrices commute. τ_a are the $SU(N)$ generators.

Finite temperature using the path integral formalism is introduced as boundary conditions in temporal direction

$$\Psi(t + 1/T) = -\Psi(t) \quad (6)$$

$$A_\mu(t + 1/T) = A_\mu(t). \quad (7)$$

The path integral therefore becomes

$$Z = \int D\bar{\psi}D\psi DA_\mu \exp(- \oint_{1/T} dt \int d^3x \mathcal{L}(\bar{\psi}, \psi, A_\mu)). \quad (8)$$

This means that the vibrational modes in the temporal direction has to come in factors of $\omega_n = 2\pi n/T$ for bosons and $\omega_n = 2\pi n/T + \pi/T$ for fermions.

It is observed that \mathcal{L} goes to $T^{-4}\mathcal{L}$ under the transformation $A_\mu \rightarrow T^{-1}A_\mu$, $\psi \rightarrow T^{-3/2}\psi$ and $x_\mu \rightarrow Tx_\mu$. One can thus remove the obvious temperature dependence, and only the temperature dependence in the running coupling constant g remains.

It should be noted, that the running of g is different when adding fermions. Another thing, is that introducing a mass term

$$\mathcal{L}_m = m\bar{\psi}\psi, \quad (9)$$

breaks this transformation, as the mass would have to transform also, which it can't due to it being a constant. This also means that as long as the temperature is small compared to the mass, the theory will look like a quenched theory, i.e. as with no fermions, since the dimensionless mass goes as m/T and thus grows for smaller temperatures.

2.2 Classical solutions

Topological objects can be found from non-trivial classical solutions to the equation of motion in euclidean space, which means that they obey

$$(D_\mu F_{\mu\nu})^a = 0. \quad (10)$$

While this is the standard definition, it is rarely the way they are derived. The simplest solution is the zero temperature solution called an instanton. To find the instanton solution (we here follow Diakonov's review [27]) one typically guess a shape, thus reducing the problem, in case the guess is correct. For the instanton solution a good guess is

$$A_\mu^a = \eta_{\mu\nu}^a x_\nu (1 + B(x^2))/x^2, \quad (11)$$

where $\eta_{\mu\nu}^a$ is the 't Hooft symbol defined as

$$\eta_{ij}^a = \bar{\eta}_{ij}^a = \epsilon_{aij} \quad (12)$$

$$\eta_{4j}^a = -\eta_{j4}^a = -\bar{\eta}_{4j}^a = \bar{\eta}_{j4}^a = -\delta_{aj}. \quad (13)$$

This simplifies the solution to a one dimensional problem with the solution

$$A_\mu^a = \eta_{\mu\nu}^a x_\nu [1 + \tan(\ln[x^2/p^2]/2)]/x^2 \quad (14)$$

$$= \eta_{\mu\nu}^a x_\nu \frac{2}{[x^2 + p^2]}. \quad (15)$$

This is seen to be a localized solution. This solution is called a 1 charge configuration, since if one plugs it into the formula for the topological charge Q_T

$$Q_T = \frac{1}{32\pi^2} \int d^4x F_{\mu\nu}^a \tilde{F}_{\mu\nu}^a = \frac{1}{64\pi^2} \int d^4x F_{\mu\nu}^a \epsilon_{\mu\nu\mu'\nu'} F_{\mu'\nu'}^a, \quad (16)$$

one obtains 1. $\epsilon_{\mu\nu\mu'\nu'}$ is the Levi-Civita symbol. Plugging the solution into the bosonic action gives

$$\frac{1}{4g^2} \int d^4x F_{\mu\nu}^a F_{\mu\nu}^a = \frac{8\pi^2}{g^2}, \quad (17)$$

which is the classical action of one instanton.

There are several other things to note about the instanton solution. First, one can move the solution around to any position in space without changing the action of the solution simply by putting $x \rightarrow x - x_0$. One can also rotate the orientation in color space. This is important when one starts to look at the instanton contribution to the path integral since such transformations are special. They correspond to zero eigenvalues of the bosonic matrix, and are therefore called zero modes. Another special feature which we will explain in section 2.4.2, is that topological objects do not only have zero modes in the bosonic sector, but also one for the fermionic sector.

While one instanton is interesting, one can also construct instanton solutions with k charge. The k -charge instanton in general is a much more complicated solution, and is thus not constructed from the equation of motion, but instead under the requirement of the solution being self-dual (+) or anti-self-dual (-)

$$F_{\mu\nu}^a = \pm \tilde{F}_{\mu\nu}^a = \pm \frac{1}{2} \epsilon_{\mu\nu\mu'\nu'} F_{\mu'\nu'}^a. \quad (18)$$

The instanton solution is self-dual and the antiinstanton is anti-self-dual. This shows that the antiinstanton has $Q_T = -1$. A solution cannot be self-dual and anti-self-dual at the same time unless $A_\mu = 0$. No analytic result exists (though a really good guess does) for instantons and antiinstantons in the same configuration. Configurations of an instanton and an antiinstanton were numerically studied by Verbaarschot [28] as a function of distance. We will do this for instanton-dyons in section 4.

2.3 Axial and Vector Symmetry

It is seen that all fermionic terms, excluding the mass term, contains some type of gamma matrix between $\bar{\psi}$ and ψ . We can therefore construct a projection in spin space as [37]

$$P_{R/L} = \frac{1}{2}(I \pm \gamma_5), \quad (19)$$

where γ_5 is a combination of gamma matrices that anti-commutes with all the standard gamma matrices and has $(\gamma_5)^2 = I$. The two projections are referred to as right and left and have the properties

$$P_{R/L}^2 = P_{R/L} \quad (20)$$

$$P_R P_L = P_L P_R = 0 \quad (21)$$

$$I = P_R + P_L. \quad (22)$$

Using this, one can rewrite the fermionic part of the Lagrangian into

$$\mathcal{L} = \bar{\psi}_L(\gamma_\mu D_\mu)\psi_L + \bar{\psi}_R(\gamma_\mu D_\mu)\psi_R + m\bar{\psi}_R\psi_L + m\bar{\psi}_L\psi_R \quad (23)$$

$$\psi_R = P_R\psi \quad (24)$$

$$\psi_L = P_L\psi. \quad (25)$$

We thus observe that for massless fermions, there is a symmetry where one rotate only the left or right hand.

One typically write these transformations in two different ways. The first is simply as we see it above as a $U_R(N)$ times $U_L(N)$ symmetry. The second is to combine it into a symmetry where you do the same operation on both the right and left part, which one denote as vector $U_V(N)$, and the other where one does the opposite, which is called axial $U_A(N)$

$$\psi \rightarrow \exp(\epsilon_a I \tau_a)\psi \quad (26)$$

$$\psi \rightarrow \exp(\epsilon_a I \gamma_5 \tau_a)\psi, \quad (27)$$

where $\tau_a \in u(N)$ works on the flavor index and γ_5 on the spin index of ψ .

These are simply linear combinations of the right and left handed transformations, but they are useful since the axial gets broken by mass terms, or mass like terms, while the vector symmetry stays a symmetry.

The axial symmetry is typically called chiral symmetry. If the mass is small compared to the temperature, chiral symmetry looks like it is restored,

but actually chiral symmetry is broken at energies much higher than that of the quark masses. This is one of the important things one study with topological objects, and is due to fermionic zero modes, who only couples to either the left or right handed part of the spinor.

Another important thing to note is that we will generally talk about the breaking of $SU_A(N)$ and not $U_A(N)$, the reason for this is that any tiny number of topological objects destroy the $U(1)$ axial symmetry [7, 8]. This is also the reason for the η' meson being more massive than the rest of the $SU(3)$ pseudo scalar particles, i.e. π , K , η .

2.4 Zero modes

Generally speaking there are two types of zero modes, bosonic and fermionic. While both are seen as zero eigenvalues of the bosonic and fermionic matrix, the way one handles them are quite different.

2.4.1 Bosonic zero modes

When calculating the bosonic contribution to the path integral, one expands to second order around the soliton solution and performs the Gaussian integral

$$\int Da \exp(-a_\mu^b W_{\mu\nu}^{bc} a_\nu^c) \propto \frac{1}{\sqrt{\det(W)}}. \quad (28)$$

One therefore wrongly divides by zero if there are any zero modes. There is a nice and physical interpretation of why this occurs. Zero modes for the bosonic determinant corresponds to deformations of the solution that does not change the action. The bosonic zero modes therefore have to be treated separately from the rest of the eigenvalues. One has to extract the direction in the space of all possible configuration that corresponds to the zero mode [9]

$$dA = \frac{dA_{cl}}{dx} dx. \quad (29)$$

$\frac{dA_{cl}}{dx}$ is typically proportional to $\sqrt{S_{cl}}$ (The action of the classical configuration). This means that the contribution of the zero mode is proportional to the space it lives in. This is typically the volume of the physical space, or the surface of a sphere, for color rotations.

The contribution of the bosonic determinant therefore takes the form

$$\int Da \exp(-a_\mu^b W_{\mu\nu}^{bc} a_\nu^c) \propto \frac{1}{\sqrt{\det(W')}} \int d^N x \sqrt{S_{cl}}^N \quad (30)$$

where W' is W but with the zero modes removed, and N is the amount of zero modes.

2.4.2 Fermionic zero modes

The fermionic zero modes are found from the Dirac equation [6]

$$\mathcal{D}\psi = \mathcal{D}(\psi_R, \psi_L) = 0. \quad (31)$$

The Dirac equation can then be written as

$$\mathcal{D}\psi_R \equiv \sigma_\mu D_\mu \psi_R = 0 \quad (32)$$

$$\bar{\mathcal{D}}\psi_L \equiv \bar{\sigma}_\mu D_\mu \psi_L = 0, \quad (33)$$

where $\sigma_\mu = (I, i\sigma_i)$ and $\bar{\sigma}_\mu = (I, -i\sigma_i)$. By using another \mathcal{D} or $\bar{\mathcal{D}}$ this can be rewritten as

$$\bar{\mathcal{D}}\mathcal{D}\psi_R = (D^2 + \frac{1}{2}\bar{\sigma}_{\mu\nu}F_{\mu\nu})\psi_R \quad (34)$$

$$\mathcal{D}\bar{\mathcal{D}}\psi_L = (D^2 + \frac{1}{2}\sigma_{\mu\nu}F_{\mu\nu})\psi_L \quad (35)$$

$$\sigma_{\mu\nu} = \frac{1}{2}(\sigma_\mu\bar{\sigma}_\nu - \sigma_\nu\bar{\sigma}_\mu) \quad (36)$$

$$\bar{\sigma}_{\mu\nu} = \frac{1}{2}(\bar{\sigma}_\mu\sigma_\nu - \bar{\sigma}_\nu\sigma_\mu). \quad (37)$$

$\bar{\sigma}_{\mu\nu}$ is self-dual while $\sigma_{\mu\nu}$ is anti-self-dual ($\bar{\sigma}_{\mu\nu}$ and $\sigma_{\mu\nu}$ corresponds to the 't Hooft symbols contracted with the $SU(2)$ generators), so the second term is zero for $\sigma_{\mu\nu}$, if $F_{\mu\nu}$ is self-dual and same with $\bar{\sigma}_{\mu\nu}$ and anti-self-dual fields. Also D^2 is definite positive, and therefore does not have a solution that is 0 by itself.

One therefore have that self-dual fields only can have zero modes on the right part of the fermionic field, and anti-self-dual fields on the left part. We know a solution should exist due to the Atiyah-Singer index theorem[6].

2.5 Calorons and Dyons

The generalization of an instanton to finite temperature is called a caloron. The caloron can be understood as an infinite amount of instantons that sit separated with a distance of $1/T$ in the temporal direction, such that the caloron becomes periodic in temporal direction as is required. The caloron is therefore not symmetric in all 4 directions.

The caloron maintains the properties of having topological charge of 1 and has also one zero mode in the right or left handed sector, for the caloron and anticaloron. The standard caloron solution has $A_4(\infty) = 0$. In order to relate the caloron to confinement, we need a solution with $A_4(\infty) \neq 0$. The reason for this is that confinement, atleast in the quenched case, is related to center-symmetry breaking through the Polyakov loop

$$P = \frac{1}{N_c} \text{Tr}(L(x)) = \frac{1}{N_c} \text{tr}(\text{Path}[\exp(i \oint A_4 d\tau)]), \quad (38)$$

which is a type of Wilson loop that instead of going in a circle within space itself, uses that space is periodic in temporal direction and loops around one time, and thus is still a closed loop. N_c is the amount of colors. Path stands for path ordered.

Without fermions the Polyakov loop is an order parameter for confinement. With fermions it is not, but lattice studies still show it to be an important measurement for confinement, and it is still important that the configuration gives the correct value for P .

One typically parameterizes $L(x)$ by its eigenvalues as

$$L = \exp(i \times \text{diag}(\mu_1, \mu_2, \dots, \mu_N)), \quad (39)$$

where we order such that $\mu_{i+1} > \mu_i$ and $\mu_{i+N} = 2\pi + \mu_i$. A useful quantity is the difference between two μ 's which we define as $v_i = \mu_{i+1} - \mu_i$. For 2 colors we for instance have

$$P = \cos\left(\frac{v}{2}\right). \quad (40)$$

We therefore need a caloron solution with specific values of μ_i 's. A solution with these properties was found by P. van Baal and T. Kraan [18], and L. Lee and C. Lu [17]. We call it the caloron with non-trivial holonomy. The

solution uses the ADHM construction, where one constructs configurations which are self-dual (or anti-self-dual) using vectors of rank $K + 1$ that obey

$$\Delta^\dagger v = 0 \tag{41}$$

$$v(x)^\dagger \partial_\mu v(x) = A_\mu(x) \tag{42}$$

$$\text{Im}[\Delta^\dagger \Delta] = 0, \tag{43}$$

where Δ is defined as

$$\Delta = (\lambda_k, B_{k,k'} - xI_{k,k'}) \tag{44}$$

$$x = x_\mu \sigma_\mu \tag{45}$$

$$\sigma_\mu = (I, i\sigma_i). \tag{46}$$

σ_i are the Pauli matrices and the entries in λ_k and $B_{k,k'}$ are $U(2)$ matrices. The caloron with non-trivial holonomy is constructed by requiring the solution to be periodic up to a phase in the temporal direction, where the phase decides the value of the Polyakov loop. One therefore has that the rank of the vector v is infinite, and the caloron with non-trivial holonomy is therefore found from differential equations. The resulting solutions are very long, but are well described in [38].

Just like the instanton, the caloron with non-trivial holonomy is found to be dependent on the size ρ . The interesting thing about this caloron is that in case ρ is large, then one observes that the caloron splits into N_c localized bumps. In the limit $\rho \rightarrow \infty$, it is found that each of these bumps themselves are a solution to the equation of motion. Also since the caloron was constructed to be self-dual, then all the bumps will also be self-dual. These bumps are what we call the instanton-dyons (or dyons for short), and they lead to the interpretation that the caloron is made up of N_c dyons.

The dyon itself is a $SU(2)$ construction and can be written as [27]

$$A_4^a = \pm \hat{r}_a \left(\frac{1}{r} - v \coth(vr) \right) \tag{47}$$

$$A_i^a = \epsilon_{aij} \hat{r}_j \left(\frac{1}{r} - \frac{v}{\sinh(vr)} \right), \tag{48}$$

such that the size of the A_4 field approaches the constant v as one gets further and further away from the core around zero. The \pm are for dyons and antidyons. It is important to note that the distance r is only for the x ,

y and z components. This simple form of the dyon field is in the hedgehog gauge, whose name comes from the observation that the A_4 field points away from 0 as a hedgehog. We will typically work with the gauge where we have rotated the A_4 field to point in the τ_3 direction, which introduces a Dirac string. We show how this is done in section 4.

The dyon configuration is completely constant in time. The time dependence of the caloron therefore comes from the overlap between the different dyons, as shown in Fig. 1.

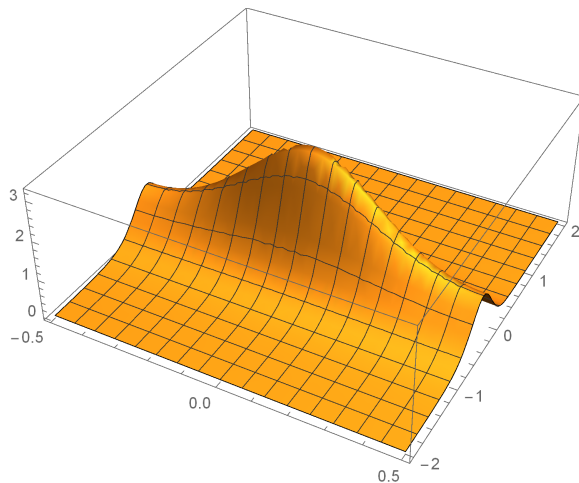


Figure 1: Caloron density for $T = 1$ and a separation of $r_{LM} = 0.2$ between the M and L dyon in x direction plotted along $t \in [-0.5, 0.5]$ and $z \in [-2, 2]$.

One needs that the distance between the dyons should be small compared to the temperature, in order to see the time dependence of the caloron. For $SU(2)$ we have two dyons which we call M and L . We denote the distance between the two dyons as r_{LM} .

The topological charge of a caloron is, just like the instanton, 1. The sum of topological charges for the M and L dyon therefore has to be 1. The solution in eq. (47) has $Q_T = \nu = v/(2\pi T)$. We call ν dimensionless holonomy. This is the M dyon solution. The L dyon solution have $v \rightarrow 2\pi T - v$ and is rotated by a phase of 2π , such that

$$\nu \rightarrow 1 - \nu \equiv \bar{\nu} \tag{49}$$

$$|A_4(\infty)| = v, \tag{50}$$

and

$$\nu + \bar{\nu} = 1. \tag{51}$$

Away from the core, the configuration in eq. (47) looks like an electric and magnetic charge of size 1. The 2π gauge rotation for the L dyons changes the sign of the electric and magnetic color fields, such that M dyons have $(+1, +1)$ Abelian electric and magnetic charge, while L dyons have $(-1, -1)$. This also secures that the sum will look like a chargeless configuration. For the antidyon solutions one picks the opposite sign in (47) compared to the dyon solution, which results in the same electric charge but opposite magnetic charge. We call the antidyons for \bar{M} and \bar{L} . Last, plugging the dyon solutions into $S = \frac{1}{4g^2} \int d^4x F_{\mu\nu}^a F_{\mu\nu}^a$ gives $\nu 8\pi^2$ for M and \bar{M} dyons, while it gives $\bar{\nu} 8\pi^2$ for L and \bar{L} dyons. We summarize the properties in Table 1.

	M	\bar{M}	L	\bar{L}
$g^2 S_{cl}/(8\pi^2)$	ν	ν	$1 - \nu$	$1 - \nu$
Q_T	ν	$-\nu$	$1 - \nu$	$\nu - 1$
e	1	1	-1	-1
m	1	-1	-1	1

Table 1: Quantum numbers of the four different kinds of instanton-dyons for SU(2) gauge theory. The rows are classical action S_{cl} , topological charge Q_T , electric charge e and magnetic charge m . The antidyons have a bar over the letter.

2.5.1 Zero modes of the dyons

The fermionic dyon zero mode is special in the sense that it only exists for some dyons. This is in sharp contrast to the caloron which always has one zero mode. To understand the zero mode of the dyon, one first has to define the boundary condition of the fermions.

$$\psi(t + 1/T) = \psi(t) \exp(iz). \tag{52}$$

The standard case is to choose $z = \pi$ which results in an anti-periodic boundary condition as is required for fermions. But dyons only have normalizable zero modes in case that $\mu_i < z < \mu_{i+1}$ [39, 40, 41]. This means that for the

case of $SU(2)$, the L dyon will have the zero mode, since μ can maximally be π in $SU(2)$, such that the M dyon can never have large enough μ in order to have a normalizable zero mode. On the other hand if $z = 0$, then only the M dyon will have a zero mode. This has a large impact on the fermionic interactions. This is discussed in section 7.

The solution for the zero mode for the dyons was found by T. Sulejmanpasic and E. Shuryak in [39] by solving

$$(\sigma_\mu)_{\alpha\beta}(D_\mu)_{AB}\psi_\beta^B = 0, \quad (53)$$

which is the Dirac equation for zero mass and right handed part of the spinor. The solution was found using the ansatz

$$-\psi_\beta^A \epsilon_{\beta\alpha} = \eta_{A\alpha} \quad (54)$$

$$\eta = \alpha_1(r)I + \alpha_2(r)\hat{r}_i\sigma_i, \quad (55)$$

from which it was found that

$$\alpha_1(r) = c_1 \left(\frac{\tanh(rv/2) \cosh(r\phi) - 2\phi \sinh(r\phi)}{\sqrt{rv \sinh(rv)}} \right) \quad (56)$$

$$\alpha_2(r) = c_1 \left(\frac{-\coth(rv/2) \sinh(r\phi) + 2\phi \cosh(r\phi)}{\sqrt{rv \sinh(rv)}} \right), \quad (57)$$

where $\phi = zT$. It is seen that the behavior for large distances go to

$$\psi \sim \frac{\exp(-r(v/2 - \phi))}{\sqrt{r}}, \quad (58)$$

such that the exponential fall off is dependent on the holonomy and the boundary condition. This means that the exponential fall off for periodic zero modes will go as $v/2$ and will sit on M dyons. L dyons start with holonomy $\bar{v} = 2\pi T - v$ which is rotated by a 2π gauge rotation. The fermions gain a phase of π from this and the solution therefore becomes antiperiodic and falls off as $\bar{v}/2 = (2\pi T - v)/2$. This shows that the shape of the zero modes follows that of the dyon themselves, i.e. when the holonomy for $M(v)$ and $L(\bar{v})$ dyons become small, the dyons and their zero modes grow in size, but get a smaller amplitude, due to the normalization constant.

2.5.2 Dyons and antidyons

While nice analytic equations exist for the cases of only dyons or only antidyons, the actual vacuum that we want to explain is rarely only one or the other, it is a combination of both dyons and antidyons. This is a much less trivial case since the previous solutions was only found due to being self-dual or anti-self-dual. In order to explain the interactions that happen we therefore have to numerically calculate the contributions. This was done for the classical action for instantons by Verbaarschot [28] and is the approach we follow in section 4, where we put a dyon and an antidyon on a lattice and find the action of the system as a function of distance between the dyons.

The same is true for the case of the fermionic zero modes. The Atiyah-Singer index theorem tells that their should be as many fermionic zero modes as the total topological charge [6]. In case that we have both dyons and antidyons, the total topological charge can be zero. This is a good thing, since the determinant of the Dirac operator for massless quarks can be written as the product of all eigenvalues

$$\det(\mathcal{D}) = \prod_i \lambda_i, \quad (59)$$

which means that configurations with zero modes do not contribute. When we have both dyons and antidyons, the zero modes are only almost-zero modes, which create a strong linear like potential between the dyons and antidyons. This becomes important in section 6 when we start to explain an ensemble of dyons and antidyons with fermions included.

2.6 Quantum Weight of the caloron

In the end what we want to calculate is the path integral

$$Z = \int D\bar{\psi} D\psi DA_\mu \exp(-S_f(\bar{\psi}, \psi, A_\mu) - S_b(A_\mu)) \quad (60)$$

$$= \int DA_\mu \det(\mathcal{D}(A_\mu)) \exp(-S_b(A_\mu)). \quad (61)$$

To obtain the quantum weight, one expands around the classical solution $A_{cl,\mu}$, as $A_\mu = a_\mu + A_{cl,\mu}$ [27]

$$S_b = S_{cl} + \frac{1}{g^2} \int d^4x (D_\mu F_{\mu\nu})^b a_\mu^b + \frac{1}{2g^2} \int d^4x a_\mu^b W_{\mu\nu}^{bc} a_\nu^c + O(a^3), \quad (62)$$

where the constant S_{cl} is the classical action of the soliton one expands around and the linear term is zero, due to the equation of motion. To second order we therefore obtain the following result for the bosonic part only

$$Z_{boson} \propto \exp(-S_{cl}) \frac{1}{\sqrt{W_{\mu\nu}}}, \quad (63)$$

which is mostly a formal formula. To actually calculate the result, one has to extract the zero modes from $W_{\mu\nu}$ as discussed in section 2.4.1, since it looks like one divides by 0, but in reality obtains an integral over the entire space, and therefore will get contributions proportional to the volume. After that is done, regularization is still needed. The typical approach is to normalize to the free propagator and normalize that result, to the same result but with a cutoff μ , which gives 4 determinants. Last, one then has to actually calculate the determinant. All of this was done in [26] for the caloron with non-trivial holonomy in $SU(2)$, which produced the result

$$\begin{aligned} Z_{Boson} &= \int d^3 z_1 d^3 z_2 T^6 C \left(\frac{8\pi^2}{g^2} \right)^4 \exp(-8\pi^2/g^2) \left(\frac{1}{Tr_{LM}} \right)^{5/3} \\ &\times (2\pi + v\bar{v}r_{LM}/T)(vr_{LM} + 1)^{\frac{4v}{3\pi T} - 1} (\bar{v}r_{LM} + 1)^{\frac{4\bar{v}}{3\pi T} - 1} \\ &\times \exp\left(-\frac{Vv^2\bar{v}^2}{12\pi^2 T} - \frac{2r_{LM}}{\pi T} \left[\pi T \left(1 - \frac{1}{\sqrt{3}} \right) - v \right] \left[\bar{v} - \pi T \left(1 - \frac{1}{\sqrt{3}} \right) \right] \right), \end{aligned} \quad (64)$$

where z_i are the positions of the dyons, r_{LM} (sometimes also called r_{12}) is the distance between the dyons and C is an overall constant. We will use this formula in the limit $r_{LM} \rightarrow \infty$ such that we can divide the contribution into one for M dyons and one for L dyons.

For the determinant of the Dirac operator we will need to calculate the corrections to the zero modes, since we otherwise have a contribution of 0. We explain this in section 6, when we add fermions to the interacting ensemble.

2.7 Ensemble of dyons

Following [27] the path integral can then be written as a sum over all contributions to the path integral from all different amount of dyons

$$\begin{aligned}
Z &= f(V) \sum_{N_M, N_L, N_{\bar{M}}, N_{\bar{L}}} \frac{1}{(N_M!), (N_L!), (N_{\bar{M}}!), (N_{\bar{L}}!)} \\
&\times (d_\nu)^{N_M+N_{\bar{M}}} (d_{\bar{\nu}})^{N_L+N_{\bar{L}}} \int d^N x J(x_i, N_M, N_L, N_{\bar{M}}, N_{\bar{L}}), \quad (65)
\end{aligned}$$

where N is the total amount of degrees of freedom coming from bosonic zero modes. N_i is the amount of dyons of type i . $f(V)$ is the contribution that depends only on the volume. For a constant A_4 field, which the dyons are corrections to, $f(V) = \exp(-\frac{V4\pi^2\nu^2\bar{\nu}^2}{3})$ [42] which is called the Gross-Pisarski-Yaffe (GPY) potential. d_ν is the contribution from the specific M or \bar{M} dyons and $d_{\bar{\nu}}$ is the contribution from L or \bar{L} dyons. The factorial factors is in order to not double count, since for instance two M dyons at position x_i and x_j , are the same as two M dyons at position x_j and x_i . We generally will work with $N_M = N_{\bar{M}}$ and $N_L = N_{\bar{L}}$. This means that the total magnetic and topological charge will be zero. The factor J is a correction to the path integral, which depends on the position of all the dyons. This will include the classical interactions which we will find in section 4, the metric where we follow [27], and the corrections to the fermionic zero modes, which we do in section 6. The integral $Z_{changed} = \int d^N x J(x_i, N_M, N_L, N_{\bar{M}}, N_{\bar{L}})$ is not possible to solve analytically and is therefore solved numerically instead using the Metropolis algorithm, while the rest, which we will call $Z_{unchanged}$, is simply constants that depend on volume, holonomy and density of the dyons. We thus write the total contribution as $Z = Z_{unchanged} Z_{changed}$. This is further explained in section 5.

3 Programming

The region around 100-1000MeV is extremely rich in physical phenomena that change behavior with only small changes in temperature, or density of the specific system. It is this region where the construction of the particles we know of takes place. From the elegant formulation of quarks and gluons, into a complicated description of Baryons and Mesons. This is a highly complicated transition, which is not described by standard perturbation theory. In order to explore this region, computer simulations has become an important tool.

This work has been a combination of numerical and analytic results in order to better understand the mechanics behind the non-perturbative results. Computations has been performed using a single graphics card (GTX 980). We will focus in this section on what a graphics card is and how it has helped obtain the numerical results. We will also talk about the basic of programming with graphics card, which was done using CUDA, which require the code to be run on NVIDIA graphics cards. We will also mention c++ which was the choice of basic code.

3.1 Graphic Processing Unit

The graphics processing unit, or GPU for short, is a processing unit in computers specialized in altering large amount of memory in a short amount of time. One can think of it as a specialized version of the central processing unit (CPU), which has to be able to handle a large amount of processes. For this reason, a GPU is never used by itself, but instead is ordered by the CPU to perform different tasks.

The GPU also tend to have its own smaller memory located close to the GPU. This means that an important part in using the GPU is to make sure that the memory is ready for use, when a task requires it, or one has to wait for the memory to be send.

Another keen difference in using the GPU is that the GPU is split into a lot more small cores, that each processes the task allocated to it. This means that one has to make sure that the code is highly parallel when using the GPU. By parallel we mean that different tasks are not dependent on each other. A typical example of this is multiplying matrices. If one multiplies two matrices of size N , then this can be seen as N^2 vector products, each

independent of each other (though some will use the same memory). One can therefore make each core handle one of the N^2 vector products. To get an idea of how large the matrix should be, for the GPU to be useful, lets use the example of the GTX 980, which has 2048 cores. One needs to multiply atleast a 50 times 50 matrix to proper utilize the GPU. Another way to utilize the GPU is to run 20 different matrix multiplications of size 10 times 10 at the same time. Of course not all cores tend to finish at exactly the same time, so in general, it is better to give more commands, than the amount of cores of the GPU, since cores that fishing early then can begin on the next job, which in general creates less downtime, i.e. time where the cores are waiting without doing anything.

3.2 c++

There are several programming languages that can be used to work with CUDA, which is the language used to control the GPU in this work. Due personal preference, this work has been done using c++.

c++ is good for defining and handling different structures and groups and is also one of the faster programming languages when it comes to execution speed. This of course depends on the project at hand, but since the main computations were done in CUDA on the GPU the important thing for me was a language which I find easy to use.

c++ besides easy group definitions have the range of standard functions like *while* and *for* that contain loop structures. Other important uses are the *if* function that check if a statement is true or not. Another useful property is the dynamic definitions of functions which can be declared and defined in different positions.

c++ also have an easy way to handle dynamic memory which is created using the *new* statement. This allows for creating extra memory for specific tasks when needed.

All of these functions works in almost exactly the same way when working with the GPU and so for a person used to work with c++, the jump to GPU programming is not that big. There are of course some small differences, which is related to calling functions and moving memory which I will discuss in the next subsection.

One of c++ strengths is also its weakness. While being a high level programming language, it still allows for strong control of addresses using pointers. This can make the use of arrays much easier. On the other hand

this leaves the program vulnerable to memory leaks, where you are changing data in wrong places. This can sometimes be hard to detect and is something one has to be careful about.

c++ also require you to make all the definitions for the used variables. I personally find this to be a positive, since it helps you in knowing what you are working with, and not passing something stupid to a function, but it is extra work. One also has to be sure to destroy dynamic memory after one is finished using it, or you might break the program, run out of memory.

3.3 CUDA

CUDA is a programming language developed by NVIDIA in order to do computations on the GPU. For this reason it is also restricted to only GPU's produced by NVIDIA. CUDA is not a standalone language, but instead adds some extra commands to already existing languages which makes it possible to control the CPU and the GPU at the same time. Since I use c++ together with CUDA, this will be the angle from which I discuss CUDA, but it is also possible to use Fortran or Python.

I will in this part discuss the most essential differences there exist when using CUDA. I will do this by giving small examples where I describe what the code does.

3.3.1 Memory

The biggest difference in my opinion is that GPU's have their own independent memory away from the CPU. This means that if one wants to use memory from the CPU on the GPU, then one has to allocate space for the memory in both the CPU and the GPU and then move the memory one way or the other. The first thing is to allocate the memory in both the CPU and the GPU which one wants to use

```
double * V = new double[size];  
double * dV;  
cudaMalloc(&dV, sizeof(double) * size);
```

The first line is the standard c++ call to create an array of size "size" of the type double. * V means that the array is identified by a pointer called V, which shows where in the memory the array is located. Second line is

an undefined pointer, which will be used to point to the GPU memory. The last line creates the same size memory in the GPU. I follow the naming convention that anything which is on the GPU gets the same name as the CPU equivalent, but with a d in front. This is because in CUDA the GPU is referred to as the "Device", while the CPU is the "Host"

When finished with the memory one needs to delete it again using

```
delete[] V;  
cudaFree(dV);
```

When one wants to move the memory in between the CPU and GPU one uses one of the following commands

```
cudaMemcpy(dV, V, sizeof(double) * size, cudaMemcpyHostToDevice);  
cudaMemcpy(V, dV, sizeof(double) * size, cudaMemcpyDeviceToHost);
```

The first line copies from the Host(CPU) to the Device(GPU), while the second line does the opposite way. Also the pointer which you copy to, is always the first argument, and the third argument is the size of the moved object.

When moving memory, the standard is to block everything else until the memory is moved. In case the program is heavy on movement between the CPU and GPU one can do asynchronous movement, which means that the GPU and CPU do calculations while moving the memory. One can still not use the same memory while moving it, but it can be used to prepare other parts while doing calculations. This will not be discussed in details.

One can move other things than just simple arrays. For instance classes in c++ (a construction that can hold several different types of variables and functions) can be moved using the same code. While moving the class is exactly the same, one has to change the code for the functions in the class, and for functions in general, for them to work on the GPU.

3.3.2 Functions

When making functions in CUDA there are in general 3 differences.

- 1) Specify where the code will run, CPU or GPU
- 2) Define the amount of threads used when calling the function

3) Allocate tasks for each thread

It is part number 3 that is the hardest.

1) When defining where the code will run, one puts `--host--` or `--device--` in front of the function name, when defining it, which has two underscores on each side.

```
--host-- --device-- void Times(double);
```

In the above example we want to be able to use the function called "Times" on the CPU and the GPU and therefore uses both. This means that we can also call the function within another function running on the GPU. One can also use `--global--` for similar results.

2) The way to call a function to run on the GPU is done in a standard c++ way, but with the extra added part in between the name and the arguments, which is enclosed by `<<<...>>>`.

```
FunctionName<<<ntreads/(Block size)+1, Block size>>>(Arguments);
```

where `ntreads` is the amount of treads one wants to run. A thread is how the GPU divides up the work. For instance using the `Times` function to do 1000 multiplications would look like

```
Times<<<1000/(32)+1, 32>>>(dV);
```

such that we have atleast 1000 different treads each doing multiplication. These treads will then be automatically divided to the different cores in sizes of a block. The block size, is a way that the GPU allocates work, and can be chosen as many different values. A general rule of thumb is that the block size should be dividable by 32. The block size will affect the time it takes to run the program, but will not break it. The +1 is to make sure that there are enough threads for the operation.

3) The last point about using functions on the GPU is to make each thread do its own task, this means that any function that runs multiple threads will have the following code in it always

```
int id = blockIdx.x * blockDim.x + threadIdx.x;  
if(id < ntreads){  
.....
```

```
}
```

The first line creates an integer identification number from the block number, and tread number. This creates a specific value for each of the operations, such that you can assign different tasks, dependent on the value of the id. The second line checks to make sure that the id is within the size of the amount of operations being done. From the previous case we would create $((1000/32)+1)*32=1024$ threads, since $1000/32=31$. The *if* function makes sure that the 24 extra operations doesn't do anything. the will be the actual code that should depend on the id, because otherwise it is a bit of waste running the same code several times. An example of what that code could be is

```
dV[id] = dV[id]*5;
```

This makes the thread with value id obtain the id'th value from dV, multiply it by 5, and then save it back to the same spot again. It is important that it is in the same spot, since an operation like

```
dV[id+1] = dV[id]*5;
```

would mean that the result would depend on which thread got to the memory first. The reason is that if the thread with for instance id =5 goes slightly before the thread with id=6, then it might have changed the value which the 6th thread will get. This will result in a different result compared to if the 6th thread had gone before the 5th thread. Since one cannot control the order this happens in, then this creates unpredictable results. This is something one has to avoid, and is generally the problem with parallelizing code.

Generally any code that runs on the CPU will also work when done on the GPU, so standard functions like *if*, *for*, and *sin* or *exp* can all be used inside the code that runs on the GPU using CUDA. One can also do calls to classes and functions inside the code that runs on the GPU without any changes, as long as the function has been specified to run on the GPU also.

3.4 Programs

While different versions of the programs exist, and extensions, additions and changes have been performed over the progression of work, there have fundamentally been 2 programs which have been used to make the results presented in this dissertation. The first one is the "Gradient Flow" program used in section 4 and the second is the "Interacting ensemble" program used in section 5, 6 and 7. I will below explain the basic construction of the two programs, and for each program discuss the biggest bottlenecks in computation speed.

3.4.1 Gradient Flow

The gradient flow is a program that takes a $SU(2)$ configuration of gauge fields and calculate the current of the action $-\frac{\delta S}{\delta U_\mu}$ at each point in space, and then changes all the $SU(2)$ links, with a change ϵ times the current found for each link.

The program can be broken up into 3 parts. The setup, the gradient flow, and the read off. The first and last part is only done once, and optimization for proper run time is not important. The setup consist of creating the configurations one want to use gradient flow on. The way this is done is explained in section 4. The read off part saves the final configuration to a file.

The important part of the program, is the part that does the actual changes to the configuration. This consist of two parts. The first part calculates the current as explained in section 4.2, while the second part applies the current to each link, by converting the current into an $SU(2)$ matrix, also shown in section 4.2. This is then repeated a lot of times until the action is reduced enough. To monitor this progress and in order to understand the changes, several results are calculated simultaneously at each step. The total action is used to determine when the simulation should stop.

Since the program consist of a lot of small multiplications of $SU(2)$ matrices, the limiting factor in the program, is how quickly memory can be transported from the GPU memory to the cores in the GPU doing the actual work. This problem was tackled in 3 ways.

- 1) The first way is to minimize the actual memory one has to send, by rewriting all $SU(2)$ matrices in terms of $1, i\tau_1, i\tau_2, i\tau_3$. This cut the amount of memory movements and calculations one has to do in half.

- 2) Use some extra time to calculate different combinations and save them

locally in each thread. Certain multiplications occur always in certain combinations. By identifying these, one can limit the amount of times one has to fetch new memory. Also writing mathematical objects like trace as the "1" component of $(1, i\tau_i)$ also reduces memory fetching.

3) Structure of the array can impact memory fetching time quite a bit. One of the reasons is that if the structure is such that several cores need memory adjacent to other cores, a call fetching everything at the same will automatically be performed, greatly increasing speed. It is therefore important to "play" with which of the coordinates you use first in your definition of the arrays, and sometimes, transposing an array can increase speed also.

Almost the entire part of the gradient flow runs on the GPU, with a few things like adding a few numbers to obtain the total action is performed on the CPU. The only limiting factor is therefore the GPU in the program.

3.4.2 Interacting Ensemble

The interacting ensemble program is mostly about getting as many as possible different configurations as possible. The program is therefore about running as many of the same small programs simultaneously. Each small program does the following.

Start up) Generate 64 random positions on a S^3 sphere using Gaussian distributions in each of the 4 dimensions, and normalizing length to 1.

Each Cycle) Change 1 position. Calculate the action and compare with old configuration as $\exp(-\Delta E)$ to get configurations with weight $\exp(-E)$. Measure at each step the action E of the maintained configuration. Do this for all particles.

Finish) Write all configurations to a file.

The part that takes the most time in this program is calculating the eigenvalues, since the metric needs to be only positive eigenvalues. In order to do this, we followed the technique from [43] since the matrix was symmetric. The principle is to first tridiagonalize the matrix. This means that only values on the diagonal and next to it is non-zero. This is done by multiplying the matrix A by the following

$$A \rightarrow (I - uu^T)A(I - uu^T) \quad (66)$$

where u is a vector, such that $\text{Det}(I - uu^T) = \pm 1$ and doesn't change the eigenvalues since $(I - uu^T)(I - uu^T) = I$. The vector u is made out of the row

(or column, since it is symmetric) you want to change. To make the matrix A into a tridiagonal form, one skips the values until value $A_{i,i+1}$. This ensures that the left multiplication and right multiplication will not interfere with each other, and therefore leaves the row and column with zero on all places for $j > i + 1$. u is constructed from A in the following way

$$u = (0, \dots, 0, A_{i,i+1} + L, A_{i,i+2}, \dots, A_{i,N}) / \sqrt{L(L + |A_{i,i+1}|)} \quad (67)$$

$$L = |(0, \dots, 0, A_{i,i+1}, A_{i,i+2}, \dots, A_{i,N})|. \quad (68)$$

When $(1 - uu^T)$ is applied it puts every entry two away from the diagonal to zero in one row or column. This therefore has to be repeated for all rows and columns until the form is tridiagonal (we call the matrix T after this is done).

The eigenvalues are thereafter obtained in a similar manner, where one repeatedly apply

$$T \rightarrow (1 - ww^T)T(1 - ww^T), \quad (69)$$

to the now tridiagonal matrix. w is constructed as u but starts instead at the diagonal. Every time this is applied to all the different rows, the off diagonal becomes smaller and smaller, until one decides it is small enough and stops the calculation, and obtains the eigenvalues on the diagonal. The eigenvalues will first converge in the lower buton, and as they do, the part that converge is cut of, and calculations proceed on the rest that has not yet converged.

Convergence happens from buton to top. By guessing the eigenvalue λ from a 2×2 block at the buton, and shifting the matrix by $-\lambda I$, one can speed up convergence.

There is also another good use of the same formula. In situations where the matrix have small entries, numerical precision can be affected by the standard way of obtaining the determinant by adding lines to make the entries below the diagonal zero. One uses the formula in eq. (67) but only from one side, and starting from the diagonal. This improves the determinant a lot, since the matrix is still made into upper triangular form, but one does this using the length of the vectors, and does not end up dividing by a small number. This was important when calculating the overlap of the fermionic zero modes as explained in section 6, since many of the entries in the matrix are exponentially suppressed.

3.4.3 Single and Double precision

It is important to understand the amount of digits one needs to use, i.e. single or double or even higher precision. This choice can be important since in case your simulation consist of enough steps, then small rounding errors can build up. This is important when doing the gradient flow, where the $SU(N)$ matrices have to obey $\det(U) = 1$. For this type of problem, double precision was needed. One can of course also decide to normalize the matrices all the time instead.

On the other hand the Monte-Carlo simulations randomly changes from step to step, and rounding errors therefore will not affect the answer, and single precision has been perfectly fine.

3.5 The Metropolis Algorithm

When ever one wants to get an average of a measurement, one has to integrate over the space of all possible configuration. This can be a huge space that numerically is impossible to handle. A typically way to handle this problem, which is also how we handled this problem in the "Interacting Ensemble" program, is to do importance sampling instead. As the name indicates, one try to sample only the important part of the integral, while only having small statistics on the part of the integral that does not contribute too much. We do this using the Metropolis algorithm, which is a type random sampling. The Metropolis algorithm includes an acceptance of the random step at each update of the configuration. The way this is done is that we have a multidimensional integral of the form

$$\langle f \rangle = \int d^N x f(x) \exp(-E(x)) / \int d^N x \exp(-E(x)), \quad (70)$$

where we want to use $\exp(-E(x))$ as the probability. Each step in the sampling consist of changing one (one can also do several) coordinate and then calculate the difference in E from one configuration to the other (ΔE). One then decides to use the new configuration if

$$rand < \exp(-\Delta E), \quad (71)$$

where $rand$ is a random number between 0 and 1. This means that in case ΔE is negative, then one always accept the new configuration. After each

step one measure $f(x)$, such that the integral is given by

$$\langle f \rangle = \frac{1}{N} \sum_i f_i, \quad (72)$$

where N is the total amount of random steps and f_i is the i 'th measurement of $f(x)$. In this way one samples the value of $f(x)$ much more rapidly than one otherwise would have done. The precision of random importance sampling is much less for small dimension integrals, but the increase in needed iteration steps does not increase very quickly for higher dimensions, and is therefore good for this type of problem.

Some problems one has to be careful about when using random importance sampling is first, that it only works for always positive measurements, and second, that there can exist different sectors, separated by areas with large E . In such cases one might end up sampling only part of the full integral, since the other part is cut of. One also has to make sure that the probability to go from $x \rightarrow y$ by the random number generator is the same as for going from $y \rightarrow x$. If not, one will create a bias in the simulation, that will produce wrong results. Last, a good random number generator is required.

4 Classical dyon interactions

In this section we explain how the classical correction to the action of a dyon and an antidyon was obtained. We start by explaining how to prepare the state of the two dyons. This is only an initial guess which is fixed when using the streamline procedure. We then explain how we put the configuration on the lattice and use the streamline procedure to minimize the action. The resulting configuration as a function of computer time is shown, and extrapolated to the continuum limit and infinite volume limit, where we obtain the correction to the action as a function of the distance between the dyons. We also present other measurements, such as the A_4 fields in different directions, and the flux along the holonomy through different boxes.

4.1 The setting

4.1.1 Instanton-dyons and their superposition

The configurations we explore are the dyons as explained in section 2.5. In this subsection we explain how to add two dyon configurations. This is only an initial guess, which will be corrected by the streamline approach.

Let us just remind that “Higgsing” the $SU(2)$ gauge theory by a nonzero vacuum expectation value (VEV) of A_4 splits three gluons into two massive and one massless (diagonal) one, according to which the Abelian charges are defined. In the simplest so called hedgehog gauge, in which the color direction of the “Higgs” field at large r is directed along the unit radial vector $A_4^m \rightarrow v\hat{r}_m$, the solutions are

$$\begin{aligned} A_4^a &= \pm\hat{r}_a \left(\frac{1}{r} - v \coth(vr) \right) \\ A_i^a &= \epsilon_{aij} \hat{r}_j \left(\frac{1}{r} - \frac{v}{\sinh(vr)} \right), \end{aligned} \tag{73}$$

where $+$ corresponds to the M dyon and $-$ corresponds to the \bar{M} dyon. r is the length in position space. The L and \bar{L} dyon are obtained by a replacement $v \rightarrow 2\pi T - v$ and a certain time-dependent gauge change.

Any superpositions of the dyons at nonzero A_4 are nontrivial since one should match at large distances not only in magnitude, but also its direction in color space. Those can be achieved by the following four-step procedure:

- (i) “combing”, or going to a gauge in which the “Higgs field” $A_4^3 = v$ (upper index is color generator, lower index is the Lorentz one) at large distances is the same in all directions and for all objects
- (ii) performing a time-dependent gauge transformation which removes v completely
- (iii) superimposing the dyons in this gauge
- (iv) making reverse time-dependent gauge transformation, reintroducing v .

(i) Description of the “combing” procedure can be found in [27]. The gauge matrices are rotations which put a radially directed unit vector into $\pm z$ direction. It is convenient to write those using spherical coordinates r, θ, ϕ instead of Cartesian coordinates x . The plus one is

$$S_+(x) = \begin{pmatrix} \cos(\frac{\theta}{2}) & \sin(\frac{\theta}{2})e^{-i\phi} \\ -\sin(\frac{\theta}{2})e^{i\phi} & \cos(\frac{\theta}{2}) \end{pmatrix},$$

S_- is obtained by setting $\theta \rightarrow \pi - \theta$. It should be noted that this choice of transformation is not unique. The matrix $\Omega = S_{\pm}$ is used in the general gauge transformation of the gauge field

$$A_{\mu} \Rightarrow A'_{\mu} = \Omega A_{\mu} \Omega^{\dagger} - i(\partial_{\mu} \Omega) \Omega^{\dagger}, \quad (74)$$

which is expressed in a standard matrix-valued form

$$A_{\mu} = A_{\mu}^a \frac{\tau_a}{2}, \quad (75)$$

where Pauli matrices divided by two are the SU(2) generators in standard normalization.

- (ii) The next gauge rotation matrix depends on euclidean time and is

$$\Omega_2 = \exp(-ix_4 v \frac{\tau_3}{2}), \quad (76)$$

so the derivative term produces $-v$ and cancels the original expectation value.

- (iii) The rotated dyon and antidyon are simply added together

$$A_{\mu} = A_{\mu}^{dyon} + A_{\mu}^{antidyon}. \quad (77)$$

- (iv) Now one has to perform a gauge rotation, *opposite* to that in point (ii), with $\Omega_3 = \Omega_2^{\dagger}$. Since these rotations commute, they just cancel each

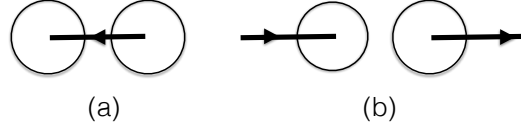


Figure 2: Two extreme positions for the Dirac strings, for the $M\bar{M}$ pair.

other except for the derivative term which puts back v at infinity. (If one would not perform steps (ii) and (iv) but would naively do step (iii), the expectation value of A_4^3 would be $2v$.)

Superimposing two dyons by such a procedure, a sum of the correctly combed potentials, is what we call *the sum ansatz*. Needless to say, it is an approximate solution only at large separation between the dyons, used only as the starting point in our studies.

As is well known, a “combed” monopole or dyon possesses the Dirac string, a singular gauge artifact propagating one unit of magnetic flux from infinity to the dyon center. By selecting an appropriate gauge one can direct the Dirac string to an arbitrary direction. Superimposing two dyons with different directions of the Dirac string, one gets *non-equivalent* configurations: the interference of singular and regular terms make the Dirac strings no longer invisible or pure gauge artifact. (However, this is cured during the gradient flow process, as we will discuss below.)

Two extreme selections for the Dirac strings are: (a) a “minimally connected dipole” when it goes along the line connecting two dyon centers; and (b) a “maximally disconnected” pair, in which two Dirac strings approach two centers from the opposite directions, see Fig. 2. Under the gradient flow the former is supposed to reach magnetically trivial configuration, while the latter relaxes to a (pure gauge) Dirac-string-like state passing the flux through the system, from minus to plus infinity. The former case appears to be simpler: but our experience has shown that the type-(b) configuration generates smaller artifacts, since the Dirac strings interfere less. We will take the type-(b) configuration as our starting configuration.

The sum ansatz possesses certain artifacts, e.g. the Dirac strings become visible in the action plot. This is to be expected due to interference of the singular Dirac string with regular solution for the other dyon. Furthermore, a correct smooth behavior at the center of each dyon is also violated, as well

as a left-right symmetry between the dyon and antidyon.

To cure some of the artifacts one may invent certain improved profiles. For example multiplying the ‘‘Higgs’’ component of the field by the factor

$$A_4^3 \rightarrow A_4^3 \frac{(x - X_M)^2 (x - X_{\bar{M}})^2}{[\rho^2 + (x - X_M)^2][\rho^2 + (x - X_{\bar{M}})^2]}, \quad (78)$$

which forces the field to vanish at the centers.

However, we observed that the gradient flow procedure eliminates such artifacts automatically, with results quite independent of the shape of the starting configuration, so no such improvements are actually needed.

4.1.2 The gradient flow

The ‘‘force’’ driving gradient flow is the current

$$j_\mu^a \equiv -\frac{\delta S}{\delta A_\mu^a} \Big|_{A=A_{\text{ansatz}}} = (D_v^{ab} G_{v\mu}^b) \Big|_{A=A_{\text{ansatz}}} \neq 0. \quad (79)$$

For solutions of the YM equation, such as a single dyon, it vanishes at all points. For dyon-antidyon configurations which we study it is nonzero, showing the direction of the gradient flow towards the reduction of the action.

Introducing the computer time τ we can write the trajectory of the resulting gradient flow according to the equation

$$\frac{dA_\mu^a}{d\tau} = -\frac{\delta S}{\delta A_\mu^a}. \quad (80)$$

4.2 Dyons on the lattice

4.2.1 The gauge fields

On the lattice the representation of the gauge field is given in terms of the so-called link variables

$$U_\mu(x) \equiv \mathcal{P} e^{ig \int_x^{x+\hat{e}_\mu} A_\mu(z) dz} = e^{iga A_\mu(x+\hat{e}_\mu/2)} + \mathcal{O}(a^3), \quad (81)$$

where a is a lattice spacing, assumed small, and

$$U_{-\mu}(x) = U_\mu^\dagger(x - \hat{e}_\mu). \quad (82)$$

The simplest gauge invariant quantity we can build using the gauge link is the plaquette

$$P_{\mu\nu}(x) = U_\mu(x)U_\nu(x + \hat{e}_\mu)U_\mu^\dagger(x + \hat{e}_\nu)U_\nu^\dagger(x) \quad (83)$$

and with the plaquette we can define a lattice gauge action with the correct continuum limit: $S = \frac{1}{4} \int d^4x F^{\mu\nu a} F_{\mu\nu}^a$

$$S = \frac{2N}{g^2} \sum_x \sum_{\mu < \nu} \left(1 - \frac{1}{2N} \text{Tr}[P_{\mu\nu}(x) + P_{\mu\nu}^\dagger(x)] \right). \quad (84)$$

To visualize the gauge field it will be useful to plot the action density using

$$s(x) = \frac{2N}{g^2} \left(1 - \frac{1}{48N} \text{Tr} \left[\sum_{\substack{\pm 4 \\ \mu, \nu = \pm 1 \\ \mu < \nu}} (P_{\mu\nu}(x) + P_{\mu\nu}^\dagger(x)) \right] \right). \quad (85)$$

Let us now translate eq. (80) into the lattice language.

All the transformations explained in section 6.2 will thus be performed on the lattice, with the link gauge transformations

$$U_\mu(x) \rightarrow \Omega(x)U_\mu(x)\Omega^\dagger(x + \hat{e}_\mu). \quad (86)$$

We still call it a “sum ansatz” although the terms are now multiplied instead. (i) We first comb the matrix U_4 by rotating it, such that U_4 has no τ_1 or τ_2 component. (ii) We do a gauge transformation in time to make the asymptotic value of U_4 equal to the identity matrix I . (iii) We multiply the two gauged dyon configurations. (iv) We do another gauge transformation to reintroduce the right value of τ_3 for the asymptotic value of U_4 . This leaves an extra term when we add the two dyons given as the following element of the temporal gauge transformation

$$\delta\Omega_t = \exp(iav\frac{\tau_3}{2}). \quad (87)$$

The time dependent parts cancel when we reintroduce the asymptotic value of A_4 , leaving $\delta\Omega_t$ behind. $\delta\Omega_t$ is not present in U_i since the gauge transformation that remove the asymptotic value of A_4 is simply $\Omega(x)U_i(x)\Omega^\dagger(x)$.

We therefore end with the $SU(2)$ matrices given by

$$U_4(x) = \tag{88}$$

$$S_+(x)U_{1,4}(x)S_+^\dagger(x + \hat{e}_4)\delta\Omega_t S_-(x)U_{2,4}(x)S_-^\dagger(x + \hat{e}_4)$$

$$U_i(x) = \tag{89}$$

$$S_+(x)U_{1,i}(x)S_+^\dagger(x + \hat{e}_i)S_-(x)U_{2,i}(x)S_-^\dagger(x + \hat{e}_i),$$

where $U_{1,\mu}(x)$ and $U_{2,\mu}(x)$ are the links of the \bar{M} and M dyon given in equation (73). It should be noted that the gauge transformation S is defined around the dyon it combs.

All time dependence is canceled, so we decided to work in 3 dimensions only, since the gradient flow will be the same for all times.

For the MM configuration we comb M with S_- and \bar{M} with S_+ . The initial configuration for $L\bar{L}$ is similar. Here we comb L with S_+ and \bar{L} with S_- . This means that the asymptotic value of A_4 becomes negative instead.

Varying the action with an infinitesimal $SU(2)$ rotation $U_\mu(x) \rightarrow (I + i\tau_k \epsilon_k) U_\mu(x)$ one finds the standard current expression

$$J_\mu(x) = \sum_\nu (P_{\mu\nu}(x) - P_{\mu\nu}^\dagger(x))$$

$$- \sum_\nu (P_{\mu\nu}(x - \hat{e}_\nu) - P_{\mu\nu}^\dagger(x - \hat{e}_\nu)), \tag{90}$$

where plaquettes P should be understood as the product of 4 links, always started from the same point x (as needed for correct gauge covariance) in the direction μ . All plaquettes that contain $U_\mu(x)$ come with a plus sign and all plaquettes that contain $U_\mu^\dagger(x)$ come with a minus sign. The next step is a projection onto the $SU(2)$ color generators

$$J_{i,\mu} \equiv dt \text{Tr}[i\tau_i J_\mu(x)]. \tag{91}$$

which eliminates possible contribution proportional to the unit matrix.

The matrix used for actual updates of the link variables is calculated as

$$L_\mu(x) = \sqrt{J_{1,\mu}^2 + J_{2,\mu}^2 + J_{3,\mu}^2} \tag{92}$$

$$\theta_{i,\mu}(x) = J_{i,\mu}/L_\mu \tag{93}$$

$$C_\mu(x) = \cos(L_\mu)I + i \sin(L_\mu) \sum_i \theta_{i,\mu} \tau_i. \tag{94}$$

The multiplication of all links by $C_\mu(x)$

$$U_\mu(x) \rightarrow C_\mu(x)U_\mu(x), \quad (95)$$

is our version of one step of the gradient flow. We checked that, with the double precision code used, the link matrices remain belonging to $SU(2)$ within small errors, even after thousands of time steps needed in the calculation. For small enough $d\tau$ the action should monotonously decrease, and indeed it does at all times.

4.2.2 Lattice details

Since $M\bar{M}$ pairs and $L\bar{L}$ pairs are time independent ($L\bar{L}$ pairs are time independent in the gauge where the Higgs field is $-(2\pi T - v)$), the lattice used is three-dimensional with size N^3 . The fields on it are not periodic. In order to protect the expectation value of A_4^3 during gradient flow, we hold the sides of our cube constant, i.e. we don't update the links on the edges of the lattice.

Most of the calculations are done with 64^3 cubic lattice. Its size in absolute units is $40/v$ in each dimension with $a = 0.625/v$, unless otherwise specified. This might seem like a rough lattice. While all configurations *before* combing have sufficiently small A even at the cores, so that $|aA_\mu| \ll 1$, *after* combing large fields $aA \sim 1$ do appear, coming from the Dirac string: however those are pure gauge and they do not affect the action at the streamline part of the process, as we will explain below.

On this setup the discretized analytic solution of one dyon is stable under gradient flow. Its action is 5% lower than the analytic value of $4\pi v$, which is due to fields outside of our box. The absolute value of electric and magnetic charge, calculated by the Gauss flux integrals over certain cubes near the box surface, are both equal to ± 1 , inside the numerical accuracy of the double precision code we use.

The 4-d gauge action expressed in terms of the 3-dimensional action is

$$S = \frac{1}{g^2} \int_0^{1/T} dx_4 S_3 = \frac{S_3}{g^2 T}, \quad (96)$$

which is itself dimension full and scales as $S_3 \sim v$: thus the M dyon action is $S \sim v/g^2 T$. The actual value of T and the gauge coupling g are irrelevant for our calculation of S_3 since it is just an overall factor in the action S .

Furthermore, since our classical 3d theory is scale invariant $A_\mu \rightarrow v^{-1}A_\mu$ and $r \rightarrow vr$, the absolute units of v are unimportant and we can use $v = 1$. In other words, all distances are in units of $r * v$.

Apart from the action and electric and magnetic charges, we also monitor the presence of the Dirac strings as the system evolves.

The circulation integrals $\oint dx_\mu A_\mu$ around the Dirac string are calculated, by adding the phases of subsequent links in the τ_3 -direction, using the inverse of the parameterization

$$U_\mu(x) = \cos(\phi)I + i \sin(\phi) \sum_i \theta_{i,\mu} \tau_i. \quad (97)$$

We do observe the famous 2π phase circulation at all times of the gradient flow, indicating that the Dirac string flux through our box remains there.

4.3 Results

4.3.1 Qualitative features of the streamline

Before we present our results in detail, we would like to give a brief overview of the findings, starting with a reminder of the streamline for the instanton-antiinstanton case. These configurations, either in quantum mechanical setting [44] or gauge fields [28], have the topological charge zero and a meaning of tunneling forth and back, with only finite time spent in the second well (valley). When this time is small, there is no reason for the configuration itself to be different from zero (path or gauge fields). So, the end of the instanton-antiinstanton streamline are the configurations with a small action $S \sim 1$ which cannot be treated semiclassically.

The case under consideration, with the instanton-dyons, is quite different. While two charges, the magnetic and the topological ones, still add to zero and can annihilate each other, the electric charge remains, which adds to 2. Our definition of charge is based on the flux through a closed surface, and the charge density is the divergence of the field. Since the electric charge is not conserved in this definition, there is no reason that the electric charge has to be equal to 2 throughout the streamline.

One might think that the process is dominated by the electric charge. We found it is not the case, and it is the behavior of the magnetic charge which is most important.

The gradient flow process was found to proceed via the following stages:

- (i) *near initiation*: starting from an ansatz described above one finds rapid reduction of the action and disappearance of artifacts related with the Dirac strings
- (ii) relatively slow and universal evolution along the *streamline set*. The action decrease is small but steady. The dyons basically approach each other, with relatively small deformations: thus the concept of an interaction potential between them makes sense at this stage
- (iii) a *metastable state* at the streamline's end: the action remains practically constant, evolution is very slow and is an internal deformation of the dyons rather than their further approach
- (iv) *rapid collapse* into perturbative fields, plus some zero action (pure gauge) remnants

A sample of computer time histories for the total action is shown in Fig. 3. The stage (i) corresponds to near-vertical initial evolution, stage (ii) to declining universal line, stage (iii) to the horizontal part at the right, followed by another vertical line of total action collapse to zero (not shown).

Crucially important is the observation that, even at the end of the streamline, the action value is not that far from the sum of those of the two separated dyons. In other words, the classical interaction potential we found is in a sense *numerically small*.

We observe an *universality* of the streamline: independent on the initial ansatz and even initial dyon separation we find that our gradient flow proceeds through essentially the same set of configurations at stages (ii-iv). A parameter we found most practical for their characterization is simply their *lifetime*, duration, in our computer time τ , from a particular configuration to the final collapse. To emphasize that, in Fig. 3 we have drawn histories with different initial but the same final times.

The existence of stage (iii) has not been anticipated. All configurations corresponding to it have the same action, and, within our accuracy, the same dyon-antidyon distance. One can perhaps lump all of them into a new metastable configuration, a dyon-antidyon molecule. (Perhaps those can be identifiable in the lattice gauge field ensembles.)

For configurations with the initial separation smaller than $4.2/v$, we observe that dyons move away from each other, to the same metastable configuration.

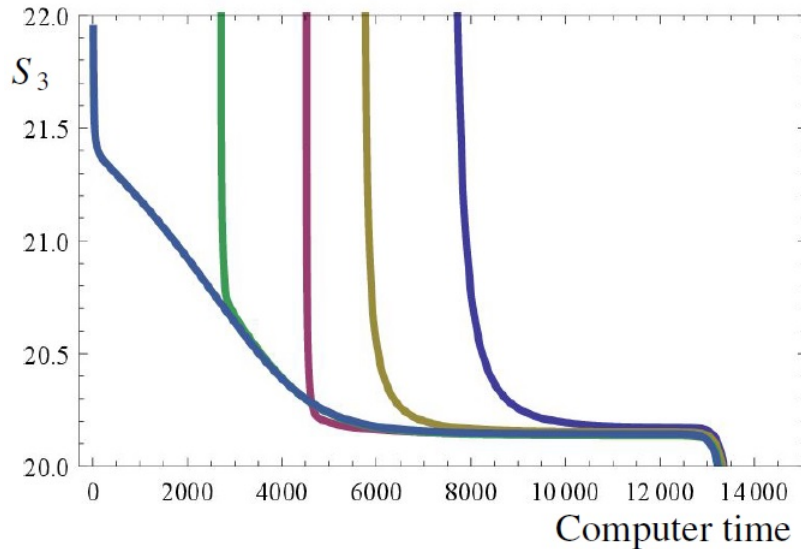


Figure 3: 3d-action S_3 for $v = 1$ as a function of computer time for an initial separation $|r_M - r_{\bar{M}}|v = 0, 2.5, 5, 7.5, 10$ between the M and \bar{M} dyon from right to left in the graph. The action of two well separated dyons is 23.88 for the lattice with 64^3 points.

4.3.2 Parameterization of the M and \bar{M} Streamline

To define the “interaction potential” between dyons and antidyons we need two things. First, we need the action S_3 as a function of computer time, a sample of which was already shown in Fig. 3. Second we need to define the separation between the dyons, and follow it as a function of computer time over the gradient flow. Locations of the dyons at a specific computer time is inferred from the two maxima of the action density. We define it in each configuration by fitting 3 points around each maximum with a second order polynomial.

A sample of action density distribution is shown in Fig. 4.

Combining the actions and dyon separations we obtain the interaction potential. We use the configuration that starts with a separation of $10/v$ between the dyons to obtain the interaction potential, since it was the configuration that started with the largest separation. The range of separations, as always in units of $1/v$, is from (slightly smaller than) $r = 10/v$ to $r = 4.2/v$:

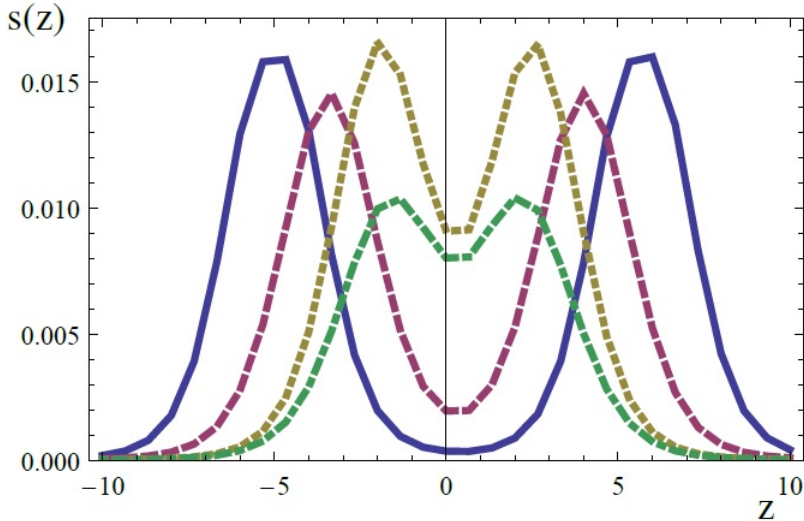


Figure 4: Action density along the z axis in natural units for a separation $|r_M - r_{\bar{M}}|v = 10$ between the centers of the two dyons. The configuration with the maximums furthest from each other is the initial configuration. At computer time $\tau = 3000$ it has moved further towards the center. At $\tau = 12000$ the configuration has reached the metastable configuration with a separation between the maximums of $4.2/v$. At $\tau = 13700$ the configuration has collapsed to a single maximum, which continues to shrink until the action vanishes. Histories shown correspond to those displayed in Fig. 3.

at this last value the configurations collapse to pure gauge with zero action.

To understand the “IR effect” of the finiteness of the box volume, we performed calculations on 3 different lattices, 64^3 , 80^3 and 96^3 , at fixed lattice spacing $va = 40/64$ (as described above for the 64^3 case). In Fig. 5 we extrapolate these results to infinite volume using the function

$$h(r) = \int_{-r+5}^{r+5} dz \int_{-r}^r dy \int_{-r}^r dx \frac{1}{(x^2 + y^2 + z^2)^2}, \quad (98)$$

which is the integral of $1/r^4$ for a dyon sitting at $z = -5$, in a box of half width r . The infinity at the origin was removed since we only needed the long range behavior. The volume effect is found to be in agreement to the expectation that the action density falls off as $1/r^4$.

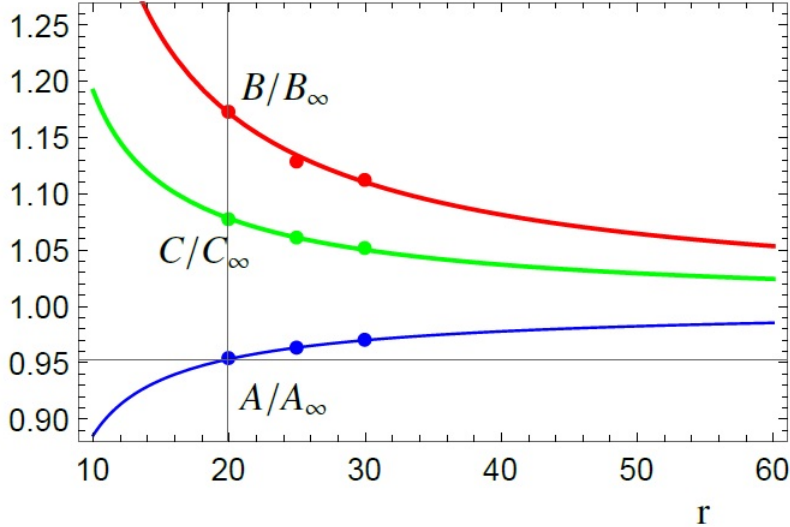


Figure 5: The 3 parameters A , B and C normalized by their value at $r = \infty$ (A_∞ , B_∞ and C_∞) as a function of lattice half width r at $va = 40/64$. We extrapolate using $c + b[h(r) - h(\infty)]$, where $h(r)$ is defined in eq. (98).

In order to understand the “UV effects” of discretization we also make calculations for 3 different lattices, 64^3 , 80^3 and 96^3 , with variable lattice spacing but the same volume (the same as for the 64^3 point setting described in section 4.2.2). In Fig. 6 we extrapolate these results to $a = 0$ with a straight line.

Using those results we extrapolated to zero spacing and infinite box, by assuming that the two effects were independent. The resulting extrapolated curve is shown in Fig. 7 (upper curve, offset), to be compared to the actual data for the largest box (lower line). The offset value is basically the 5% of the action outside the box mentioned earlier. This curve is our main result.

We use the parameterization of the resulting curve of the type

$$S_3(r) = A \left(1 - \frac{1}{r} + B \exp[-Cr] \right), \quad (99)$$

The reason the Coulomb part has no fitted parameter, other than the overall A , is based on the following analytic argument. Classical interaction is known to be zero for interactions between two self-dual (or two anti-self-dual) dyons

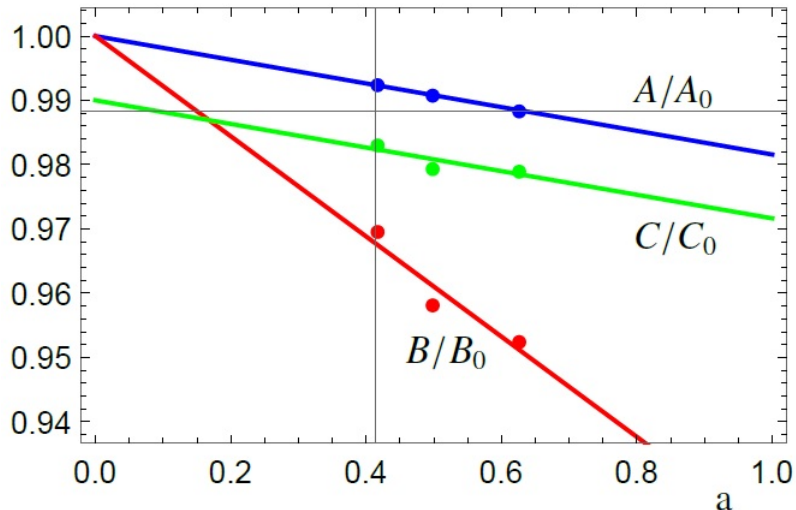


Figure 6: The 3 parameters A , B and C normalized by their value at $a = 0$ (A_0 , B_0 and C_0) as a function of the lattice spacing a . We extrapolate the results to $a = 0$ with a straight line. C/C_0 has been offset by -0.01 because it otherwise completely overlapped A/A_0 .

due to the so called BPS protection. This means that the correction from the non-Abelian part has to cancel both electric and magnetic Abelian Coulomb attractions.

In the case we consider, the interaction of self-dual with anti-self-dual objects, the electric and magnetic Abelian Coulombs cancel each other, while the non-Abelian part is expected to change its sign.

We therefore expect the long range behavior for the action S_3 to behave like

$$S_3(r \rightarrow \infty) = 8\pi v + (m_1 m_2 - e_1 e_2) \frac{4\pi v}{rv}, \quad (100)$$

where m_i and e_i are the magnetic and electric charges of the two dyons and distance is given as rv to show that all terms are proportional to $4\pi v$. The minus sign in front of the electric part, is due to the non-Abelian contribution. For the dyon-antidyon interaction we get

$$S_3(r \rightarrow \infty) = 8\pi v \left(1 - \frac{1}{rv}\right). \quad (101)$$

Since outcome of this argument was found to be in agreement with our numerical data, inside the errors, we decided not to include an extra parameter for the $1/r$ part. The exponential was found to describe the potential nicely in the fitted region, while not affecting long range behavior.

The values of the parameters and the errors obtained from the formal fit (to more than thousand points corresponding to different separation during the gradient flow process) are

$$A = 25.20 \pm 0.01, B = 1.13 \pm 0.03, C = .607 \pm .004 \quad (102)$$

Note that the value of the parameter A is only by 0.07 (or 0.3%) higher than the action of two well separated dyons in continuum, $S_3 = 8\pi \approx 25.13$. This fact confirms that our extrapolations are quite accurate, we did it as a test. In applications, one should of course use the analytic value of A mentioned. Note also that B is about 30 standard deviations from zero, ensuring that an exponential term is absolutely needed.

As a last comment, we want to point out that the curve of the action S_3 never becomes completely flat at $r = 4.2/v$ as otherwise expected. On the other hand, results with starting separations smaller than $r = 4.2/v$ clearly converges to the same point around $r = 4.2/v$. This indicates that the technique is not perfect around this point. This is most likely due to small changes to the shape of the action density, which were used to determine the position. These small changes could very well be caused by the collapse we always saw after enough time had passed.

4.3.3 Details of the Streamline

In this subsection we focus on the properties of the streamline configurations other than the action. We will subsequently discuss: (i) How does the profile of the ‘‘Higgs field’’ A_4^3 change. (ii) How does the charges change; and (iii) What happens with the Dirac strings.

4.3.3.1 Higgs Field A_4^3 Before we turn to the results, let us remind that for an individual dyon, and thus for two at large separation, the Higgs Field

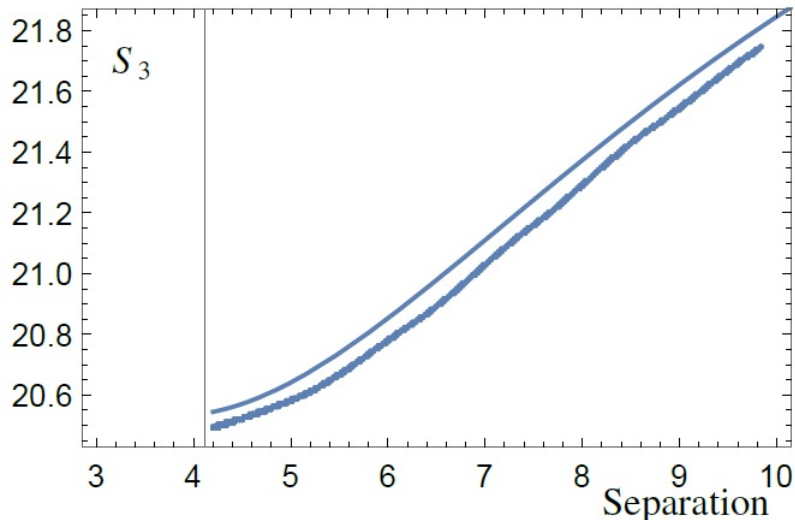


Figure 7: 3d-action S_3 of the $M\bar{M}$ dyon pair vs separation between the dyons $|r_M - r_{\bar{M}}|v$ for $a = 40/64$ for 96^3 points (lower line) and for the extrapolated fit (upper line). The fit has been offset by $\Delta S_3 = -0.9$ so its shape can be visually compared to the data. The separation of the dyons is defined by the maxima of the action density. The configuration starts at the separation of $10/v$ between the dyons. The plot is terminated after the metastable configuration. The plot contains 1243 points (1 every 10 computer times) that makes up the fitted data.

vanishes at the center. At large distances it should be the same value and direction: on the plots we use a positive one. One might expect that the same shape will be maintained during the gradient flow on the streamline.

As shown in Fig. 8, this is not the case: the Higgs Field goes through zero at the centers and gets *negative*, about $-0.5v$, in between the dyons. The upper and lower plots are snapshots for two different evolution histories, for an initial separation of $r = 5/v, 10/v$, which show the same trend.

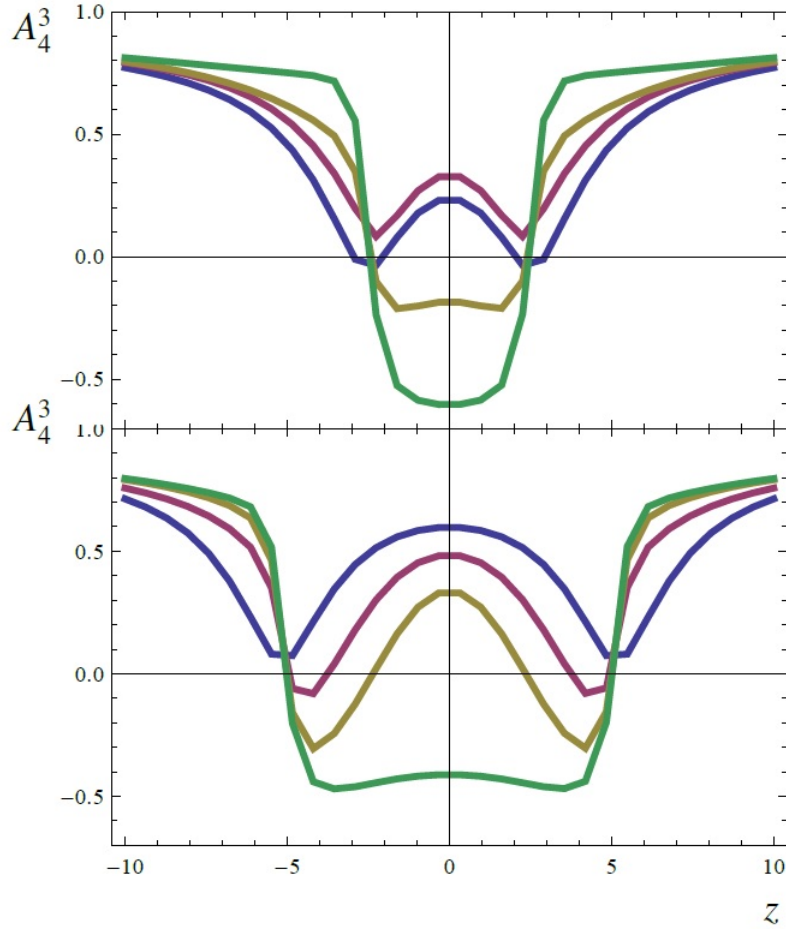


Figure 8: Subsequent snapshots of A_4^3 along the z axis in natural units for an initial separation of $5/v$ (upper) and $10/v$ (lower) between the center of the 2 dyons. (upper) The configuration with the smallest field at the sides of the plotted area is the initial configuration. At computer time $\tau = 5000$ the minimums have risen slightly, but is overall the same shape. At $\tau = 9400$ the configuration has started collapsing. At $\tau = 10000$ the configuration has collapsed to one minimum completely. (lower) The configuration with the smallest field at the sides of the plotted area is the initial configuration. At computer time $\tau = 3000$ the minimums have moved slightly towards the middle and the minimums have become smaller. At $\tau = 10000$ the configuration has reached the stable almost flat area in the action. At $\tau = 14000$ the configuration has collapsed completely to an almost flat region between the initial positions of the dyons.

4.3.3.2 The Charges The electric and magnetic charges inside certain sub-boxes are calculated via the Gauss surface integrals. Total initial charges for the $M\bar{M}$ configuration should be 2 for electric charges, and 0 for magnetic charges.

We further study charge locations using different sized boxes. These sub-boxes are all centered around the origin, with one dyon at $z = 2.5/v$ and one dyon at $z = -2.5/v$. Total widths of the sub-boxes used are $38.75/v$, $28.75/v$, $18.75/v$ and $8.75/v$, while the width of the entire box used is $40/v$. Time evolution of the electric charge inside all sub-boxes is shown in Fig. 9. We observe that all charges are very stable for about 10000 time steps of the gradient flow, though we do see a small decrease in the total electric charge, after which the electric charge quickly goes down for all boxes. This happens at the same time as the action starts to drop as well. The fact that the smallest box shows zero sharply, while the largest sub-box still contains about half of the charge 5000 time steps later, suggests that the electric charge moves out of the box gradually.

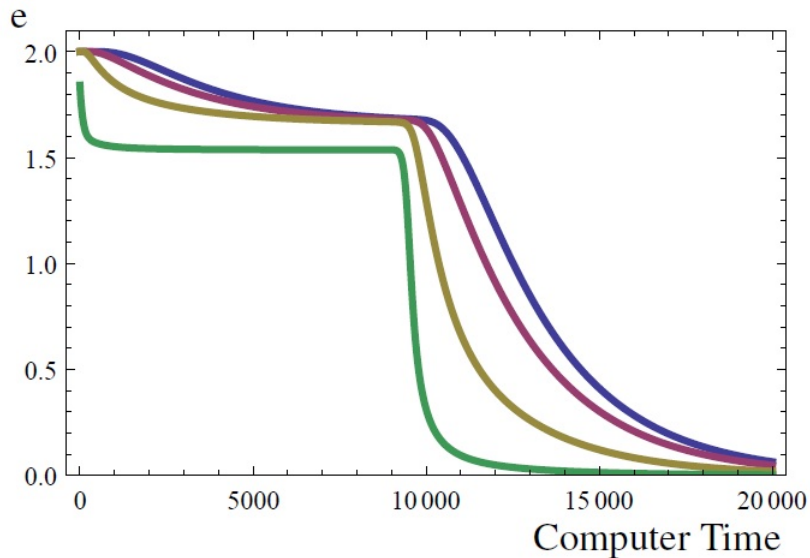


Figure 9: Electric charge for $v = 1$ as a function of computer time for an initial separation $|r_M - r_{\bar{M}}|v = 5$ between the dyons. The electric charge inside sub-boxes of width $38.75/v$, $28.75/v$, $18.75/v$ and $8.75/v$, centered at the origin.

Since the total magnetic charge is zero, we cut each of the boxes described above in half in the xy -plane, through the origin. That meant that only one dyon would be inside the sub-box. The time evolution of the magnetic charge inside the largest half-sub-box is shown in Fig. 10. The magnetic charge is very stable and close to 1, but collapses to 0. The moment is the same as that for the action collapse. We thus conclude that the magnetic structure is crucially important for the preservation of the individual solitons.

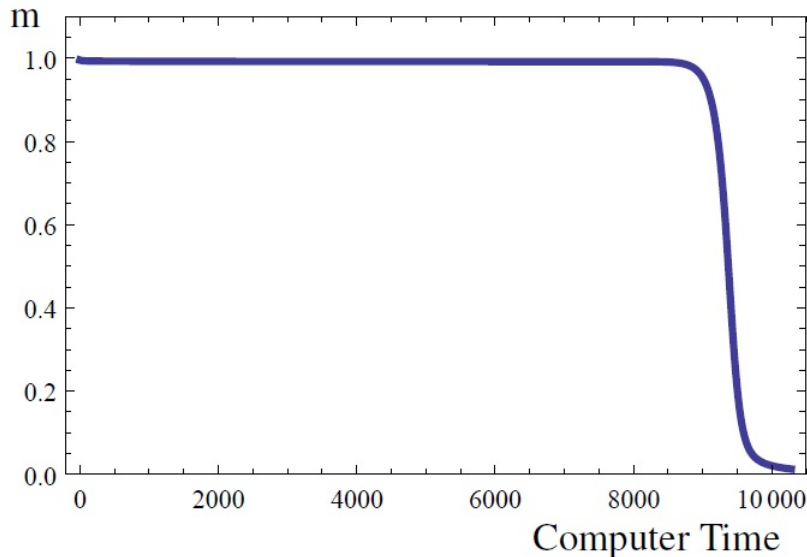


Figure 10: Magnetic charge for $v = 1$ as a function of computer time for an initial separation $|r_M - r_{\bar{M}}|v = 5$ between the dyons. The magnetic charge is found from a sub-box that goes from the middle of our lattice in z (the dyons are separated along the z -axis) and to the edge, while filling up the entire part of the x and y -axis. The drop happens at the same time as the drop in action.

4.3.3.3 The Dirac Strings We now look at the Dirac strings. While those are gauge transformation artifacts, we still wonder whether the magnetic flux they carry is there or not, through the gradient flow process. To observe the Dirac string we evaluate the phase of the spatial square loop $\oint dx_\mu A_\mu / (2\pi)$ winding around a string as explained in section 4.2. We plot the space of the spatial loop along the z -axis for an initial configuration of

$r = 5/v$ in Fig. 11 taken at the beginning (upper plot) and at the end of the process (lower plot), with loops of different size.

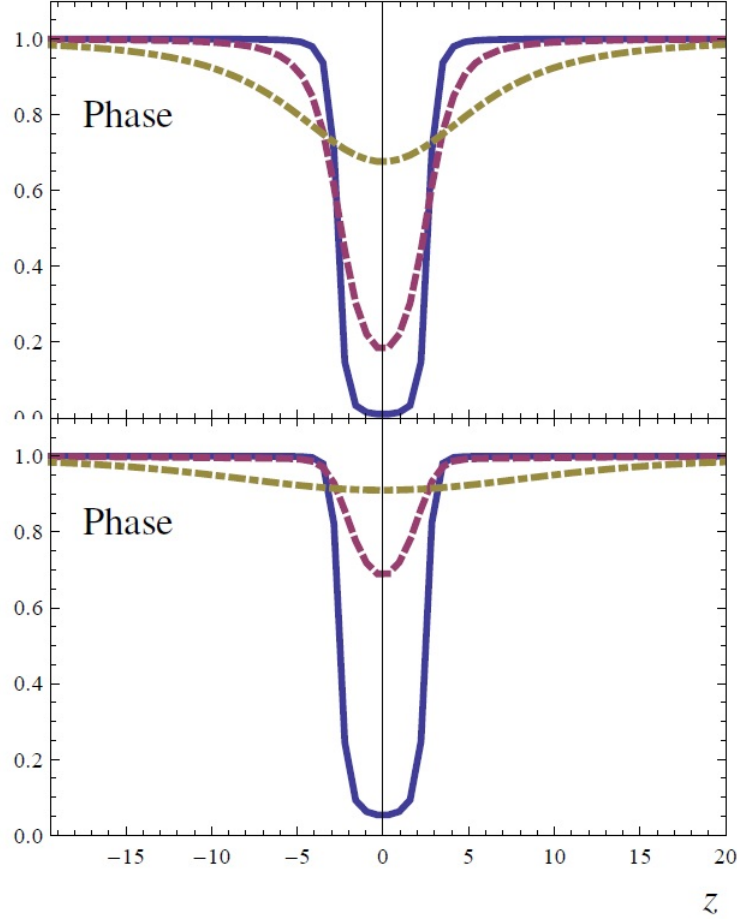


Figure 11: The phase from the strings divided by 2π for a M and \bar{M} dyon at an initial separation $|r_M - r_{\bar{M}}|v = 5$ along the z axis in natural units. (upper) Taken at the beginning of the simulation and (lower) taken at the end of the simulation. The line is for a square loop with the sides of one link, the dashed is for 5 links and the dotdashed is for 21 links.

For the smallest (square) loop used the phase takes a value close to 0 in between the two strings: there is no string there. Increasing the size of the loop, the phase gets closer and closer to 2π , as expected. The pictures are

very similar, and so the conclusion is that Dirac strings hardly change during the gradient flow process.

4.3.4 $L\bar{L}$ pairs

The $L\bar{L}$ pair has been studied in the gauge where the L dyons are constant in time. The overall result is the same as for the $M\bar{M}$ case and we therefore only point out the difference.

While the L and \bar{L} dyons are time dependent in the gauge where $\langle A_4^3 \rangle = v$, we can still explore the configuration in the time independent gauge before the time dependent gauge transformation is done. In the time independent gauge the Higgs field points in the negative direction with a value of $2\pi T - v$. To put $\langle A_4^3 \rangle = v$ we need to do a time dependent gauge transformation, but this should not affect the results.

Since nothing different from the $M\bar{M}$ pairs happens for the charge and action we won't show those graphs. More interesting is the Higgs field which after a time dependent gauge transformation looks like in Fig. 12 for initial configuration (upper) and for the configuration after the rapid drop in the action (lower).

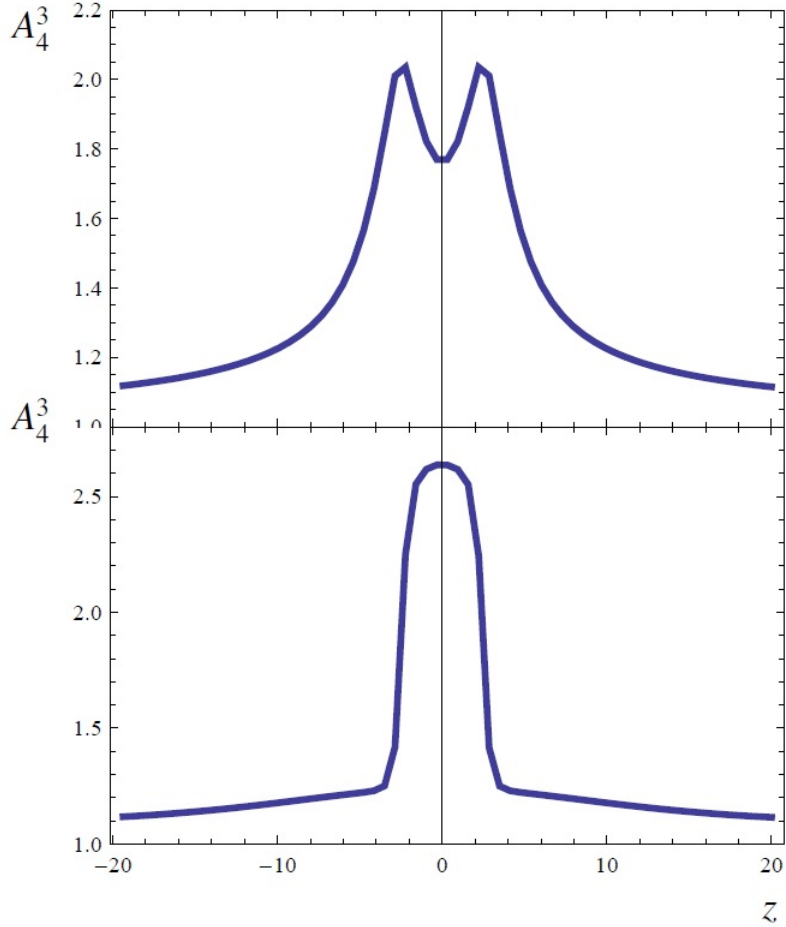


Figure 12: A_4^3 for the $L\bar{L}$ dyon pair along the separation of the two dyons (z-axis), in natural units, at the beginning (upper) and end (lower) of the simulation for an initial separation of $|r_L - r_{\bar{L}}|v = 5$. The dyons had $2\pi T - v = 1$ and the time dependent gauge transformation has been performed to make the Higgs field at infinity equal to 1.

It is seen how the valleys are now instead a mountain for the L and \bar{L} dyons, since we have gauged the results such that $\langle A_4^3 \rangle = 1$. After gauging back to the gauge where $\langle A_4^3 \rangle = v$, we find that A_4^3 have gained a time dependent core. This time dependent core comes from the τ_1 and τ_2 component of A_4 which have become non-zero around the origin as shown in Fig. 13. The

A_4^3 component which is the mountain shown in Fig. 12 (lower), stays time independent.

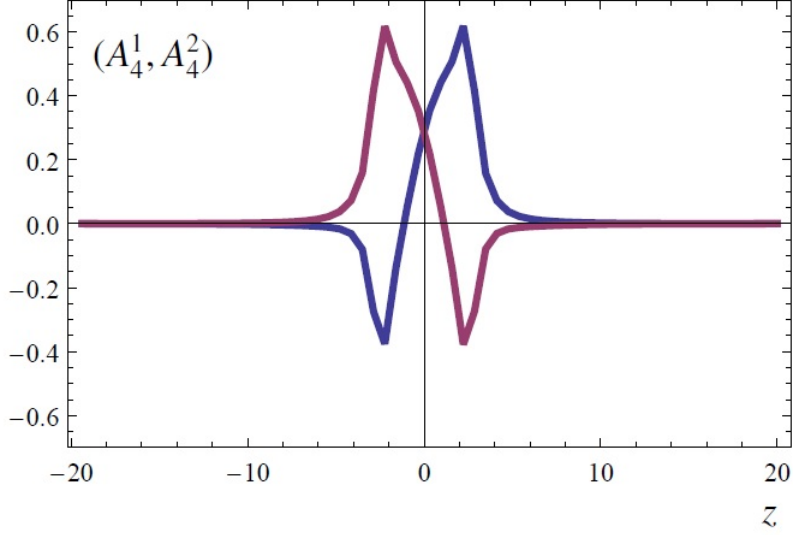


Figure 13: A_4^1 and A_4^2 along the separation of the L and \bar{L} dyon (z -axis) for an initial separation of $|r_L - r_{\bar{L}}|v = 5$, at the end of simulation, before the extra time dependent gauge transformation has been done.

When one do the time dependent gauge transformation, the time dependence that A_4 do gain is only for the τ_1 and τ_2 component of A_4 , since $\exp(i\pi T x_4 \tau_3) \tau_{(1,2)} = \tau_{(1,2)} \exp(-i\pi T x_4 \tau_3)$. This means that the gauge transformation that puts $\langle A_4^3 \rangle = v$ will mix the τ_1 and τ_2 component of A_4 with a time dependent phase.

5 Ensemble of Instanton-Dyons

In this section we build an ensemble of instanton-dyons. We first show a toy model of an excluded volume model. The factors in the toy model partition function are similar to our final goal of an interacting ensemble, and gives therefore a nice idea of the expected behavior. We then explain the interactions which we will use in the interacting ensemble. The main property we want to numerically find is the free energy. This will be done by finding the expectation value of the action for different values of the coupling constant, which will be integrated up to the free energy. We explore the free energy density for a variety of different values of the holonomy, coupling constant, densities of dyons and cutoff mass. By finding the configuration with the smallest free energy density, we find the dominating configuration, and therefore the behavior that dominates the vacuum. This is the main result for this section, and will be presented as a function of coupling constant/temperature. Mainly the Polyakov loop and the density of the dyons are interesting.

5.1 An excluded volume model

To understand the main physics involved and the qualitative behavior of the ensemble, including the confinement phase transition, we start with a discussion of a simplified model in which the only interaction is the repulsive core, making the volume occupied by each particle unavailable to others. It is similar in spirit to that proposed by Shuryak and Sulejmanpasic [32], but is somewhat closer technically to the simulations to follow.

We work with dimensionless quantities, defining the 3-volume as $\tilde{V}_3 = T^3 V_3$, the density $n_i = \frac{N_i}{V_3}$, and the free energy density as $\frac{F}{T\tilde{V}_3} = f$. More information on units and notations can be found in section 5.5.

The effect of the excluded volume is accounted for in a very schematic way, by cutting off the partition function when the amount of available volume vanishes. The volume of the M and L dyons scale as $1/\nu^3$ and $1/\bar{\nu}^3$ respectively, with $\bar{\nu} = 1 - \nu$. We thus define the partition function as a sum

limited from above by some “close packing” condition

$$Z = \sum_{M,L}^{\tilde{V}_3/(\tilde{V}_0) < M/\nu^3 + L/\bar{\nu}^3} \exp\left(-\tilde{V}_3 \frac{4\pi^2}{3} \nu^2 \bar{\nu}^2\right) \quad (103)$$

$$\times \left[\frac{1}{M!L!} (\tilde{V}_3 d_\nu)^M (\tilde{V}_3 d_{\bar{\nu}})^L \right]^2$$

$$d_\nu = \Lambda \nu^{8\nu/3} S^2 \exp(-S\nu) \quad (104)$$

$$S = \frac{8\pi^2}{g^2}. \quad (105)$$

Without the upper limit, the free energy density $\log(Z)/\tilde{V}_3$ is dominated by the maximum $-\frac{4\pi^2}{3}\nu^2\bar{\nu}^2 + 2(d_\nu + d_{\bar{\nu}})$, the perturbative Gross-Pisarski-Yaffe (GPY) potential plus the contribution of the noninteracting dyons. In this non-interacting limit, the parameter d_ν , the semiclassical dyon amplitude, coincides with their density. The parameter S is in fact the classical action of the caloron, or $L + M$ system. The square comes from assuming the same amount of dyons and antidyons.

In the confining phase, $\nu = \bar{\nu} = 1/2$, all dyons have the same sizes, and it is easy to introduce the excluded volume, for N dyons via

$$\tilde{V}_3^N \rightarrow \tilde{V}_3 \left(\tilde{V}_3 - V_{excluded} \right) \dots \left(\tilde{V}_3 - (N-1)V_{excluded} \right).$$

However, in general L, M dyons have different sizes, the analogous expression becomes cumbersome. Experimenting with those, we observe that similar results are obtained by simply cutting out the sum at “closed packing”, when there is no volume left, $\tilde{V}_3 < \tilde{V}_0(M/\nu^3 + L/\bar{\nu}^3)$. where \tilde{V}_0 is the excluded volume normalized for a dyon at $\nu = 1$.

Using Sterlings formula $n! \approx \sqrt{2\pi n} \left(\frac{n}{e}\right)^n$ for a large volume, we rewrite the sum as

$$Z \approx \sum_{M,L}^{\tilde{V}_3/(\tilde{V}_0) < M/\nu^3 + L/\bar{\nu}^3} \exp \left[-\tilde{V}_3 \left(\frac{4\pi^2}{3} \nu^2 \bar{\nu}^2 - 2n_M \ln \left[\frac{d_\nu e}{n_M} \right] - 2n_L \ln \left[\frac{d_{\bar{\nu}} e}{n_L} \right] \right) \right]. \quad (106)$$

The free energy given by $F(\nu) = -T \log Z$ depends on ν , located in the cutoff, in the dyon parameter d_ν , and in the GPY potential V_{GPY} . If dominant, the GPY term would select trivial holonomy $\nu = 0$ or $\bar{\nu} = 0$, so to push

for a nontrivial $\nu \sim 1/2$ needed for confinement, the dyon densities should be large enough.

The expression (106) is put into Mathematica and the maximum is found, for large enough volume, say $V = 900$. One finds a sharp peak in N distribution, defining the density. Finding the maximum as we vary ν , we get $f(\nu) = -\log Z/\tilde{V}_3$ plotted in Fig. 14. At smaller g (larger action S and higher temperature T) the dyons are more suppressed and the free energy density f has a minimum at smaller ν . For increasing coupling g (decreasing S and T), the minimum shifts from zero, eventually to its confining value $\nu = 1/2$. For twice larger excluded volume the density may get too small to have confinement with physically meaningful negative f .

A more familiar plot is obtained if, instead of plotting ν one plots the average Polyakov loop $\langle P \rangle = \cos(\pi\nu)$, versus S , see Fig. 15. The parameter S grows monotonously with T and thus can be mapped to it (see details in section 5.5). So, in this model the Polyakov loop continuously goes to 0, the confinement regime, at some critical S_c , slightly smaller than 6.

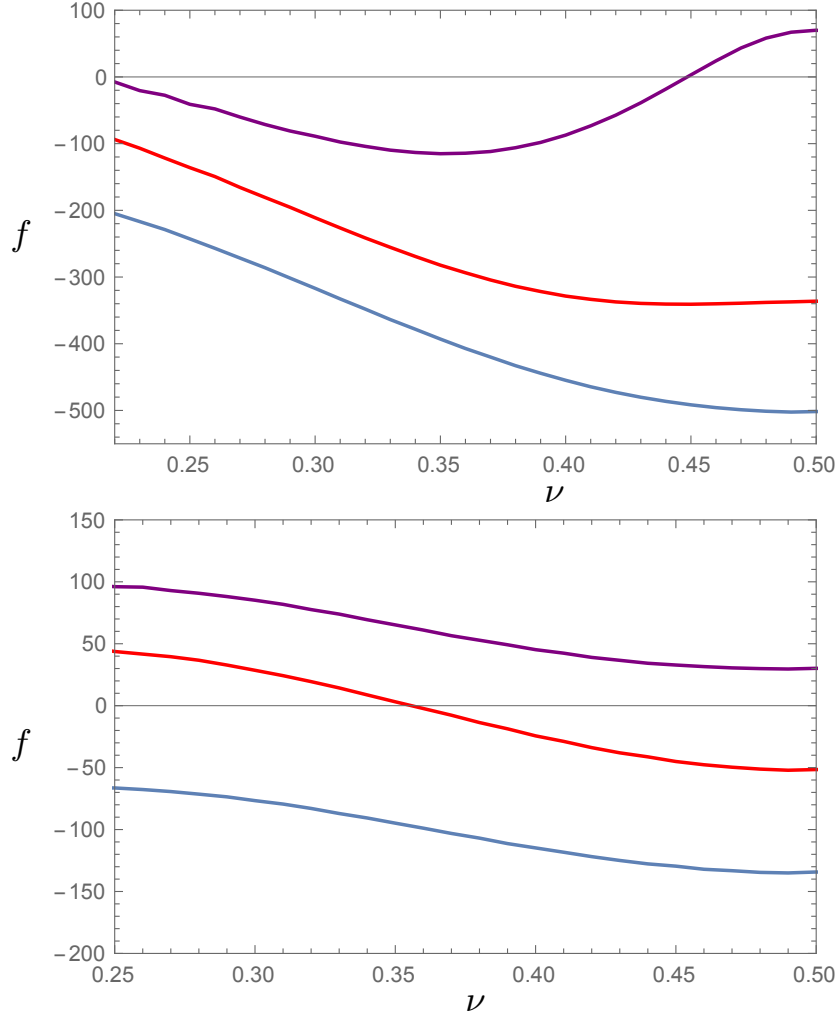


Figure 14: Free energy density f as function of holonomy ν , for $\Lambda = 0.5$ and $\tilde{V}_0 = 0.3$, for upper and $\tilde{V}_0 = 0.6$ for the lower plot. Three curves correspond to $g = 4, 3.5, 3$, bottom to top, in the upper figure and $g = 4, 3.5, 3.25$ in the bottom one. It is seen how the maximum as a function of g goes further and further towards the confining value of $1/2$ as g goes up, and action S and temperature T go down.

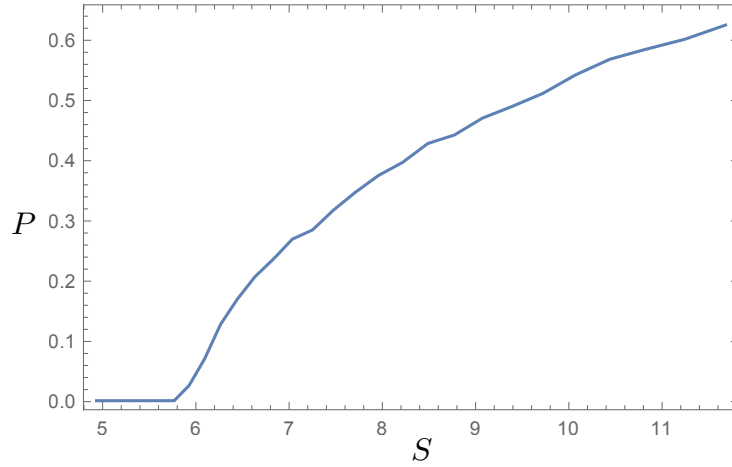


Figure 15: Polyakov loop P as a function of action parameter S for $\Lambda = 0.5$ and $\tilde{V}_0 = 0.3$.

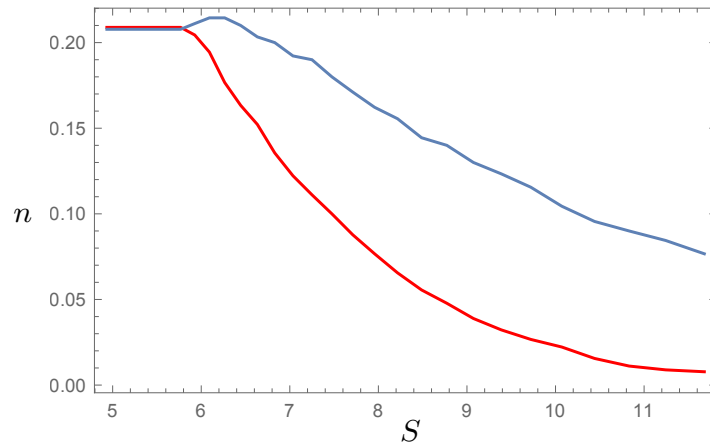


Figure 16: Densities n_i of $i = M$ or $i = L$ dyons as a function of the action parameter S , for $\Lambda = 0.5$ and $\tilde{V}_0 = 0.3$. Note that the two densities are different at $S > 6$.

In Fig. 16 we show the densities of different type (M and L) dyons,

different above the deconfinement transition.

5.2 The instanton-dyon interactions

The *leading order* classical dyon-antidyon interactions, studied in previous section 4 are the central new element in this section. We use a slightly different parameterization of it

$$\begin{aligned}\Delta S_{D\bar{D}} &= -2\frac{8\pi^2\nu}{g^2}\left(\frac{1}{x} - 1.632e^{-0.704x}\right) \\ x &= 2\pi\nu rT,\end{aligned}\tag{107}$$

since this parameterization fit on a couple of points below the metastable configuration at $x = 4.2$. This was needed since cutting off the potential with a hard-core at 4.2 excludes a too large volume. We instead will introduce a hard core at $x_0 = 2$ which is approximately the distance where configurations are immediately pushed out of. It should be noted that the specific value is chosen by us, and should be considered a parameter in the model.

If dyons are put at smaller distances, they repel till distance 4.2, before annihilation. Those configurations were not yet studied in detail, and thus our potential for $x < 4.2$ constitutes a reasonable guess. Below distance $x_0 = r_0T(2\pi\nu)$ the potential is described by

$$\Delta S_{DD} = \frac{\nu V_0}{1 + \exp[\sigma(x - x_0)]},\tag{108}$$

referred to as a “core”. Its scale by ν is due to general scaling behavior of the dyon sizes.

Let us also remind the long-distance behavior of the potentials. Self-dual soliton interacting with anti-self-dual one have Abelian electric and magnetic forces canceling each other. Another long-range interaction comes via A_4 and the non-linearity of the field strength tensor. Its coefficient is fixed in another channel, L+M (calorons) where both electric and magnetic Abelian effects are attractive, and yet the total interaction is zero due to PBS protection

$$V_{LM} = (e_1e_2 + m_1m_2 - 2h_1h_2)\frac{4\pi}{g^2}\frac{1}{r} = 0.\tag{109}$$

Returning to $M\bar{L}, L\bar{M}$ channel, one expect the non-Abelian term simply to change sign as explained in section 4.3.2. We therefore have that $h_i = e_i$.

The volume element of the metric in the space of collective variables is used in the form of the so called Diakonov determinant [27]

$$\sqrt{g} = \det G \quad (110)$$

$$\begin{aligned} G = & \delta_{mn}\delta_{ij}(4\pi\nu_m - 2 \sum_{k \neq i} \frac{1}{T|x_{i,m} - x_{k,m}|} \\ & + 2 \sum_k \frac{1}{T|x_{i,m} - x_{k,p \neq m}|}) \\ & + 2\delta_{mn} \frac{1}{T|x_{i,m} - x_{j,n}|} - 2\delta_{m \neq n} \frac{1}{T|x_{i,m} - x_{j,n}|}, \end{aligned} \quad (111)$$

where $x_{i,m}$ denote the position of the i 'th dyon of type m . This form is an interpolation of the exact metric between a M and L dyon, true at any distance, with the metric of the two dyons of same type at large distances. We introduce a cutoff on the separation via $r \rightarrow \sqrt{r^2 + \text{cutoff}^2}$, such that for one pair of dyons of same type, the diagonal goes to 0 for $\nu = 0.5$, instead of minus infinity. We use the same metric for the antidyons also.

When the density of M and L dyons are different, the total electric charge is nonzero. We therefore regularize all the Coulombic terms and the Diakonov determinant by certain screening $r \rightarrow r e^{M_D r T}$, referred to as the Debye mass. With this the interaction is given by

$$\begin{aligned} \Delta S_{D\bar{D}} &= \frac{8\pi^2\nu}{g^2} \left(-e_1 e_2 \frac{1}{x} + m_1 m_2 \frac{1}{x} \right) e^{-M_D r T} \\ x &= 2\pi\nu r T, \end{aligned} \quad (112)$$

for r larger than the core of size $x_0/(2\pi\nu T)$ for all combinations except between dyons and their antidyons. See Table 2 for the charges. For the dyon antidyon potential we use

$$\begin{aligned} \Delta S_{D\bar{D}} &= -2 \frac{8\pi^2\nu}{g^2} \left(\frac{1}{x} - 1.632 e^{-0.704x} \right) e^{-M_D r T} \\ x &= 2\pi\nu r T. \end{aligned} \quad (113)$$

We include the core for both dyon antidyon interactions, but also for dyon-dyon interactions due to the lack of a repulsion, which otherwise destroys the simulation (LL , MM , $\bar{L}\bar{L}$, $\bar{M}\bar{M}$, $L\bar{L}$ and $M\bar{M}$). We hope that such an

interaction can be found due to corrections to the metric between dyons of the same type.

$$\begin{aligned}\Delta S_{DD} &= \frac{\nu V_0}{1 + \exp[\sigma T(x - x_0)]} \\ x &= 2\pi\nu rT.\end{aligned}\tag{114}$$

	M	\bar{M}	L	\bar{L}
$g^2 S_{cl}/(8\pi^2)$	ν	ν	$1 - \nu$	$1 - \nu$
Q_T	ν	$-\nu$	$1 - \nu$	$\nu - 1$
e	1	1	-1	-1
m	1	-1	-1	1

Table 2: (Same as Table 1) Quantum numbers of the four different kinds of instanton-dyons for SU(2) gauge theory. The rows are classical action S_{cl} , topological charge Q_T , electric charge e and magnetic charge m . The antidyons have a bar over the letter.

5.3 The setup

Like in [33], instead of the usual toroidal box with periodic boundary conditions in all coordinates, our simulations have been done on a S^3 sphere (in four dimensions), to simplify treatment of the long range Coulombic forces. In this pilot study we fix the total number of dyons to 64. We do not use supercomputers or clusters, relying instead on multiple cores of a standard GPU of one standard computer.

The radius of the sphere together with the ratio of M dyons to L dyons have been used to change their density.

Iteration of the system is defined as a loop in which each dyon has had its position changed and the new action has then been accepted with the probability of $\exp(-\Delta S)$ via the Metropolis algorithm. The typical number of iterations for equilibration is 400 and productive runs after equilibration are typically 1600 iterations.

In order to get the free energy we also use a standard method. One can differentiate with respect to an auxiliary parameter λ introduced in front of

the action and get

$$e^{-F(\lambda)/T} = \int Dx \exp(-\lambda S(x)) \quad (115)$$

$$\frac{\partial F}{\partial \lambda} = T \langle S \rangle. \quad (116)$$

Since the free energy at $\lambda = 0$ is known analytically, one can integrate up to get the free energy at $\lambda = 1$. When we do this we of course need to be careful about regions with a quick change in the action.

For the calculation of $\det G$ it has been observed by Bruckmann et al [45] that it only makes sense if all eigenvalues are positive. It was observed [45] that, for randomly placed dyons this is typically not the case, unless density is very low. In [46] this issue has been discussed further, with a conclusion that the Diakonov determinant can remain positive definite at higher densities needed, but only provided certain correlations in the dyon locations are enforced. We have therefore used the Householder QR algorithm together with tri-diagonalization of the matrix G [43] to find the eigenvalues. We also redefine the potential as follows:

If all eigenvalues are positive

$$V_D = -\log[\text{Det}(G)] : V_D < V_{max} \quad (117)$$

$$V_D = V_{max} : V_D > V_{max} \quad (118)$$

and for one or more negative eigenvalues

$$V_D = V_{max}. \quad (119)$$

The excluded volume from the regions of negative eigenvalues are there, yet at the same time we do not create a region where the configuration can be trapped inside the region of negative eigenvalues. Excluded volume induces strong variation of the free energy at small λ : so we found it necessary to integrate the free energy up to $\lambda = 0.1$ finely with 10 points. From $\lambda = 0.1$ to $\lambda = 1$ we use 9 points. $V_{max} = 100$ was used.

In the simulation, all interactions are assumed to have Yukawa-like large distance behavior with certain Debye screening mass M_D . Since our “box size” can be defined as the distance between poles of our sphere, $\pi * r$. In the smallest box we have a box size of about 4 units. The smallest Debye mass employed is, in the same units, 2. Thus the exponential tails are $e^{-M_D r} = e^{-8}$, and all long range artifacts are well suppressed.

That finite volume effects are not important was tested on a few configurations as shown in Fig. 17, since it is not possible to do it for all configurations due to the computational power needed. We find that the configurations do indeed give the same results for double the volume in the area of interest, and only at densities higher than explored in this dissertation do we see a difference. The difference at higher densities is due to the sharpened behavior of $\langle S(\lambda) \rangle$, and should be fixed in case one want to do higher total number of dyons, by increasing the density of points in the integration to obtain the free energy F .

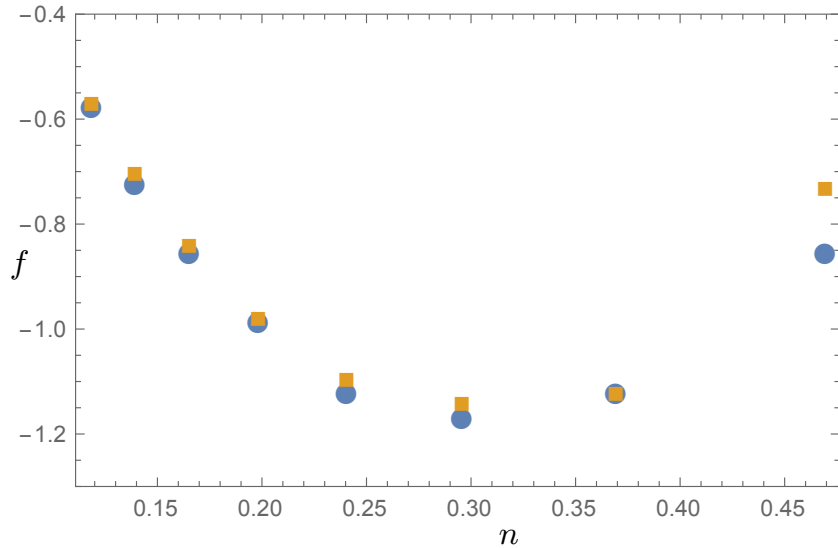


Figure 17: Free Energy density f as a function of density n for $N_{Total} = 64$ (sphere) and $N_{Total} = 128$ (square) at $\nu = 0.5$, $M_D = 2$, $S = 6$ and $n = n_M = n_L$. Volume effects are seen to not be important in the region of interest around $n = 0.3$ and difference is expected to come from the sharper shape of $\langle S(\lambda) \rangle$ in the case of $N_{Total} = 128$, which require a higher amount of points to obtain the free energy F .

5.4 The dyon weights in the partition function

To obtain the contribution of the dyons to the partition function we start from the KvBLL caloron partition function [26] as shown in eq. (64), though

without the linear term in the exponential

$$\begin{aligned}
Z_{KvBLL} &= \int d^3 z_1 d^3 z_2 T^6 C \left(\frac{8\pi^2}{g^2} \right) \left(e^{-\frac{8\pi^2}{g^2}} \right) \left(\frac{1}{Tr_{12}} \right)^{\frac{5}{3}} \\
&\times (2\pi + 4\pi^2 \nu \bar{\nu} Tr_{12}) (2\pi \nu Tr_{12} + 1)^{\frac{8\nu}{3}-1} \\
&\times (2\pi \bar{\nu} Tr_{12} + 1)^{\frac{8\bar{\nu}}{3}-1} \exp(-V_3 T^3 \frac{4\pi^2}{3} \nu^2 \bar{\nu}^2). \tag{120}
\end{aligned}$$

Taking the limit to very dilute situation we find that all powers of Tr_{12} not in the exponential cancel, and we end with

$$\begin{aligned}
Z_{KvBLL} &= \int d^3 z_1 d^3 z_2 T^6 C \left(\frac{8\pi^2}{g^2} \right) \left(e^{-\frac{8\pi^2}{g^2}} \right) \\
&\times (2\pi \nu)^{\frac{8\nu}{3}} (2\pi \bar{\nu})^{\frac{8\bar{\nu}}{3}} \\
&\times \exp(-V_3 T^3 \frac{4\pi^2}{3} \nu^2 \bar{\nu}^2). \tag{121}
\end{aligned}$$

The term in the exponential is the Gross-Pisarski-Yaffe (GPY) holonomy potential. The Diakonov determinant, which we have included, is seen to return to a product of the holonomies in the dilute limit

$$\lim_{Tr_{12} \rightarrow \infty} \det G = \prod_i 4\pi \nu_i. \tag{122}$$

By comparison we see that we have to take equation (121) and divide by equation (122) in order to get the correct weight for our partition function. We thus end up with the partition function for a M and L dyon given by

$$\begin{aligned}
Z_{KvBLL} &= \int d^3 z_1 d^3 z_2 T^6 C \left(\frac{8\pi^2}{g^2} \right) \left(e^{-\frac{8\pi^2}{g^2}} \right) \\
&\times \frac{(2\pi)^{8/3}}{(4\pi)^2} \nu^{\frac{8\nu}{3}-1} \bar{\nu}^{\frac{8\bar{\nu}}{3}-1} \\
&\times \exp(-V_3 T^3 \frac{4\pi^2}{3} \nu^2 \bar{\nu}^2). \tag{123}
\end{aligned}$$

We redefine the constant Λ so the equation is easier to work with

$$\begin{aligned}
Z_{KvBLL} &= \int d^3 z_1 d^3 z_2 T^6 \frac{\Lambda^2}{(4\pi)^2} \left(\frac{8\pi^2}{g^2} \right)^4 e^{-\frac{8\pi^2}{g^2}} \\
&\times \nu^{\frac{8\nu}{3}-1} \bar{\nu}^{\frac{8\bar{\nu}}{3}-1} \exp(-V_3 T^3 \frac{4\pi^2}{3} \nu^2 \bar{\nu}^2). \tag{124}
\end{aligned}$$

5.5 Units and holonomy

The main physical quantity of the problem is the temperature T : it defines the magnitude of the $A_4^3 = 2\pi\nu T$ (holonomy), the physical size of the dyons and every other dimensional parameter of the problem. Yet, precisely because of its omnipresence in the theory, one can (excluding temperature corrections to the coupling constant) cancel all powers of T . At this level, our theory has only dimensionless input parameters. Most of them, the dimensionless *dyon densities*, *holonomy* and the *the Debye screening mass*, will be defined selfconsistently, from the minimum of the free energy. The remaining input will be the *instanton action parameter* S , used in many plots in the text.

Standard euclidean formulation of the gauge theory at finite temperature T introduces periodic (Matsubara) time τ defined on a circle with a period equal to the inverse temperature $1/T$. The exponential of the gauge invariant integral over this circle, known as the Polyakov line

$$P = \frac{1}{N_c} \text{Tr} \left[\text{Path} \left(\exp[i \oint A_4^3(\sigma^3/2) d\tau] \right) \right], \quad (125)$$

is gauge invariant due to periodicity. Here σ^3 is the 3rd Pauli matrix.

As a function of temperature its expectation value $\langle P \rangle$ changes from 1 at high T to (near) zero at the deconfinement temperature T_c . In SU(2) gauge theory which we will discuss, $\langle P \rangle = \cos(\nu\pi)$, and the holonomy parameter (or just holonomy, for short) ν changes from 0 to 1/2. What remains unknown is the physical origin of this potential.

Perturbatively, the effect of the holonomy is the appearance of nonzero masses of quarks and (non-diagonal) gluons, and the corresponding Gross-Pisarski-Yaffe holonomy potential [42]

$$\frac{V_{GPY}(\nu)}{T^4 V_3} = \frac{(2\pi)^2 \nu^2 \bar{\nu}^2}{3}, \quad (126)$$

where V_3 is the 3-volume of the box and

$$\bar{\nu} = 1 - \nu \quad (127)$$

is “dual holonomy”. We proceed in the text to use dimensionless units for volume $\tilde{V}_3 = T^3 V_3$, densities $n_M = \frac{N_M}{V_3}$, $n_L = \frac{N_L}{V_3}$, distances $rT = x$ and free energy density $\frac{F}{TV_3} = f$. Potential V_{GPY} has a minimum at trivial holonomy

$\nu = 0$ and a maximum at confining holonomy $\nu = 1/2$, thus disfavoring confinement.

In the *next* approximation the so called quantum loop effects are incorporated. As is well known, they lead to a running coupling constant. Thus the action parameter (and all others, of course) become a function of the basic physical scale given by the temperature T . For example, recalling classical instanton action and the asymptotic freedom formula

$$S(T) = \frac{8\pi^2}{g^2(T)} = b \cdot \ln\left(\frac{T}{\Lambda}\right), \quad b = \frac{11}{3}N_c, \quad (128)$$

with the power given by the one-loop beta function. If so, the semiclassical factors defining the caloron density now depend on T , basically as a power

$$\frac{n_{calorons}(T)}{T^4} \sim e^{-S} \sim \left(\frac{\Lambda}{T}\right)^b. \quad (129)$$

Since the caloron density has been measured on the lattice at different T , one can test this expression against the lattice data. In fact it does work, see Fig. 1 of Ref. [32], which confirms that the topological solitons remain semiclassical at the temperatures we discuss.

The value of the parameter Λ in the expression for S above is chosen such that $T = 1$ at the critical temperature.

5.6 The dyon back reaction: holonomy potential

Lattice gauge simulations had shown how the peak of the holonomy distribution shifts to its confining value at $T < T_c$. The corresponding effective potential $V(\nu, T)$ has been numerically studied and parameterized, used in various models such as the so called Polyakov-Nambu-Jona-Lasinio model (PNJL).

Now our task is to derive this potential, stemming from the back reaction of the instanton-dyons. We add the perturbative GPY potential V_{GPY} eq. (126) to the dyon free energy obtained from our simulations and determine the total free energy of the system (obviously, assuming that there are no other relevant non-perturbative contributions). The dyon-induced partition function is further split into two factors: one containing all factors which depend on parameters unchanged in the simulations, and the second one related to dyons's collective variables.

$$Z = Z_{unchanged} Z_{changed}. \quad (130)$$

The weight for one caloron ($L + M$ pair) was explicitly calculated in [26]: at zero holonomy it agrees with the instanton result by 't Hooft. Part of the answer is the factor coming from the metric volume element \sqrt{g} in the space of L, M collective variables. Later Diakonov [27] combined this result with the previously known answer for the metric of two monopoles of the same kind (e.g. M, M pair) into an elegant expression for any number of L, M dyons now called Diakonov determinant $\det G$.

Taking the dilute limit $r_{12} \rightarrow \infty$ in both cases, both formulas reduce to the same r_{12} dependence and one finds that the caloron weight from [26] needs to be divided by the factor $(4\pi\nu)(4\pi\bar{\nu})$ (see section 5.4)

$$\begin{aligned}
Z_{unchanged} &= \frac{\Lambda^2}{(4\pi)^2} \left(\frac{8\pi^2}{g^2} \right)^4 e^{-\frac{8\pi^2}{g^2} \nu^{\frac{8\nu}{3}-1} \bar{\nu}^{\frac{8\bar{\nu}}{3}-1}} \\
&\times \exp(-\tilde{V}_3 \frac{4\pi^2}{3} \nu^2 \bar{\nu}^2).
\end{aligned} \tag{131}$$

Note that at the trivial holonomy $\nu \rightarrow 0$ limit, $Z_{unchanged}$ is $\sim 1/\nu$: it is to be canceled by the diagonal part of $\det(G)$.

We need to do the simulation for different amount of M and L dyons. As discussed in section 2.7, we divide the weight into a M part and a L part, and sum over all number of particles

$$\begin{aligned}
Z_{unchanged} &= \sum_{N_M, N_L} \exp(-\tilde{V}_3 \frac{4\pi^2}{3} \nu^2 \bar{\nu}^2) \\
&\times \left[\frac{1}{N_M!} \left(\Lambda \tilde{V}_3 \left(\frac{8\pi^2}{g^2} \right)^2 e^{-\frac{\nu 8\pi^2}{g^2} \nu^{\frac{8\nu}{3}-1} / (4\pi)} \right)^{N_M} \right]^2 \\
&\times \left[\frac{1}{N_L!} \left(\Lambda \tilde{V}_3 \left(\frac{8\pi^2}{g^2} \right)^2 e^{-\frac{\bar{\nu} 8\pi^2}{g^2} \bar{\nu}^{\frac{8\bar{\nu}}{3}-1} / (4\pi)} \right)^{N_L} \right]^2,
\end{aligned} \tag{132}$$

where we use that the amount of dyons and antidyons are the same. We

simplify this as

$$\begin{aligned}
Z_{unchanged} &= \sum_{N_M, N_L} \exp\left(-\tilde{V}_3 \frac{4\pi^2}{3} \nu^2 \bar{\nu}^2\right) \\
&\times \left[\frac{1}{N_M!} \left(\tilde{V}_3 d_\nu\right)^{N_M} \right]^2 \left[\frac{1}{N_L!} \left(\tilde{V}_3 d_{\bar{\nu}}\right)^{N_L} \right]^2 \\
d_\nu &= \Lambda \left(\frac{8\pi^2}{g^2}\right)^2 e^{-\frac{\nu 8\pi^2}{g^2}} \nu^{\frac{8\nu}{3}-1} / (4\pi). \tag{133}
\end{aligned}$$

$Z_{changed}$ is the interactions explained in section 5.2 and thus also depends on the number of particles

$$\begin{aligned}
Z_{changed} &= \frac{1}{\tilde{V}_3^{2(N_L+N_M)}} \int D^3x \det(G) \exp(-\Delta D_{DD}(x)) \\
\Delta f &\equiv -\log(Z_{changed})/\tilde{V}_3, \tag{134}
\end{aligned}$$

normalized such that $Z_{changed} = 1$ for no interactions included. Dyon 2-point interactions ΔD_{DD} is a sum over all classical corrections for the different dyon to dyon combinations

$$\Delta D_{DD} = \sum_{j>i} \Delta S_{D_i D_j}. \tag{135}$$

Combining $Z_{changed}$ with $Z_{unchanged}$ we get in the limit $\tilde{V}_3 \rightarrow \infty$

$$\begin{aligned}
Z &= \sum_{N_M, N_L} \exp\left(-\tilde{V}_3 \left[\frac{4\pi^2}{3} \nu^2 \bar{\nu}^2 - 2n_M \ln \left[\frac{d_\nu e}{n_M} \right] \right. \right. \\
&\quad \left. \left. - 2n_L \ln \left[\frac{d_{\bar{\nu}} e}{n_L} \right] + \Delta f \right] \right). \tag{136}
\end{aligned}$$

For $\tilde{V}_3 \rightarrow \infty$ the partition function is completely dominated by the maximum of the exponent. In this limit, finding the free energy corresponds to finding the minimum of

$$\begin{aligned}
f &= \frac{4\pi^2}{3} \nu^2 \bar{\nu}^2 - 2n_M \ln \left[\frac{d_\nu e}{n_M} \right] \\
&\quad - 2n_L \ln \left[\frac{d_{\bar{\nu}} e}{n_L} \right] + \Delta f. \tag{137}
\end{aligned}$$

Note that as the dyon density increases, it changes its shape, producing a non-trivial minimum at $\nu \neq 0$. Furthermore, at high density this minimum moves to $\nu = 1/2$, the confining value.

5.7 Self Consistency

The partition function we simulate depends on several parameters, changed from one simulation set to another. Those include (i) the number of the dyons N_M, N_L ; (ii) the radius of the S^3 sphere r ; (iii) the action parameter S ; (iv) the value of the holonomy ν , (v) the value of the Debye mass M_D ; (vi) the auxiliary factor λ , which is then integrated over as explained in section 5.3.

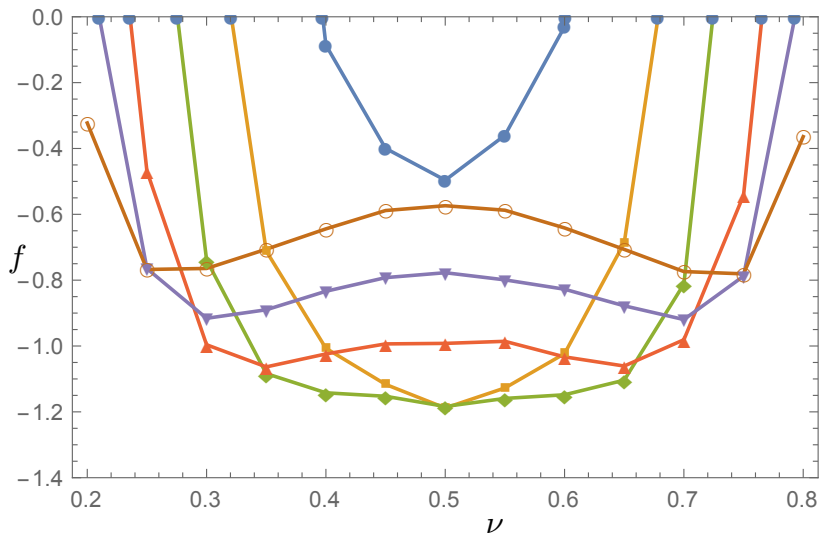


Figure 18: Free Energy density f as a function of ν at $S = 6$, $M_D = 2$ and $N_M = N_L = 16$. The different curves corresponds to different densities. ● $n = 0.53$, ■ $n = 0.37$, ◆ $n = 0.27$, ▲ $n = 0.20$, ▼ $n = 0.15$, ○ $n = 0.12$. Not all densities are shown.

In principle, the aim of our study is to obtain the dependence of the free energy on all of those parameters (i-v). While the practical cost of the simulations restricts the number of points one can study, we still had generated more than hundred thousand runs and multiple plots. However, most of it neither can nor should be included. Since our physics goal is to understand the back reaction of the dyon ensemble on the holonomy, we study the range of holonomies, from $\nu = 0$ to $\nu = 1/2$, and only then locate its minimum. As for the Debye mass, we will find it from the potential and

then show only the “selfconsistent” input set.

What we actually need to describe at the end is not the free energy in the whole multi-dimensional space of all parameters, but the location of the free energy minima. The resulting set should be of co-dimension 1, since the original physical setting of the problem, the gauge theory at finite temperature, has only one input parameter, T .

Using the definition of the Debye mass $\frac{g^2}{4\pi^2} \frac{\partial^2 f}{\partial^2 \nu} = M_D^2$ for fixed density we get the configurations response to changing the holonomy which is the Debye mass. We require that the used value for the Debye mass is the same as the one found from the derivative of f , or atleast not more than 0.4 below the used value.

The results shows that as the Debye mass goes towards zero around the phase transition. The only configuration that is consistent with this is that of equal M and L dyons.

5.8 The physical results

We now show only the results which fulfill the self-consistency requirement. Without fermions the results are symmetric in $\nu \rightarrow 1 - \nu$ and we therefore only show for $\nu \leq 1/2$. We have included the Diakonov determinant, though its impact is not too great due to the not so small Debye mass which has been calculated using 3 points. The results here are shown for a wall of $x_0 = 2$, which was chosen in order to have a large enough density of dyons to overcome the perturbative potential, without completely making the GPY potential irrelevant. We used $\Lambda = 1.5$ to obtain a phase shift around $S = 6$. Action is related to temperature as explained in section 5.5. This should of course be fitted to numerical data, but the present data on dyons does not have a high enough efficiency of detection to do this. The action goes up to $S = 13$, beyond this value the number of L dyons become too close to 1, and we would need a higher total of dyons to proceed.

Due to the repulsive Coulomb term between dyons and antidyons of different type, the free energy preferred to have a large Debye mass due to cutting off this repulsion. This meant that when the free energy spectrum as a function of holonomy for a fixed density becomes flat, the small Debye mass created a rise in energy. This resulted in a small jump in holonomy, since the configurations with holonomy $\nu = 0.5$ but with slightly higher density than the flat ones, would end up with a smaller free energy. As a result we do not get a completely smooth transition, though that is hidden by the size

of the errors as seen in Fig. 19 and it also means that at $S = 6$ the Debye mass never goes completely to zero, as shown in Fig. 20, and the density goes slightly more up also as shown in Fig. 21.

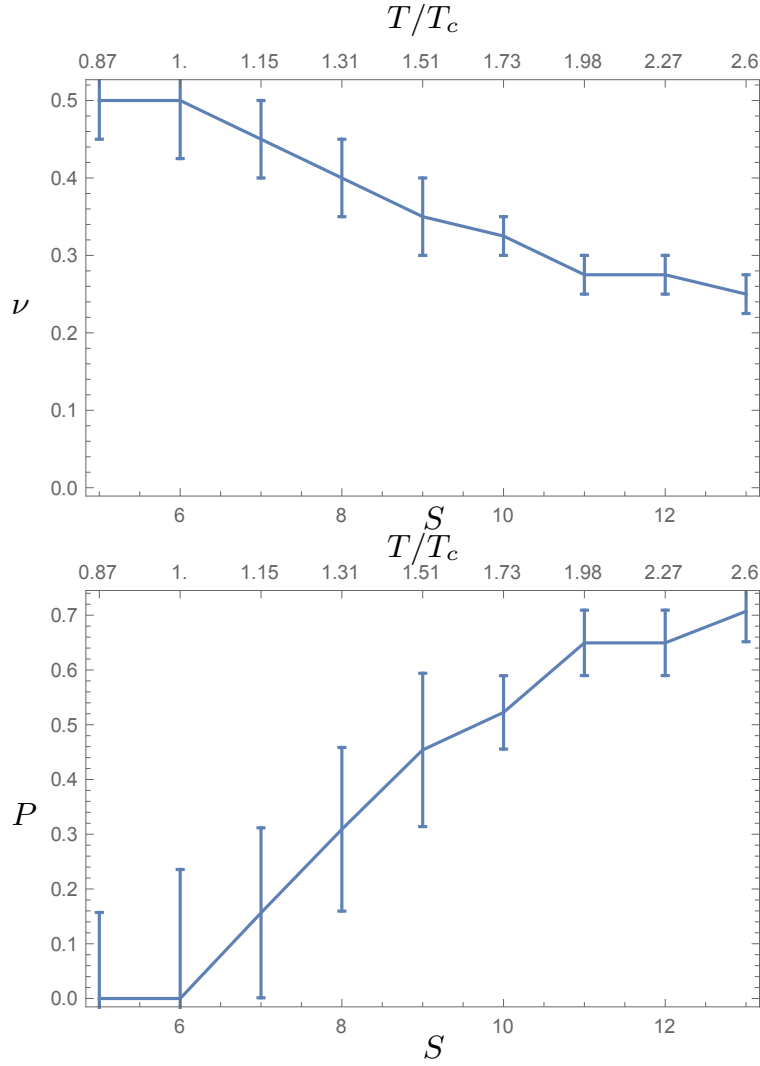


Figure 19: Self-consistent value of the holonomy ν (upper plot) and Polyakov line (lower plot) as a function of action S (lower scales), which is related to T/T_c (upper scales). The error bars are estimates based on the fluctuations of the numerical data.

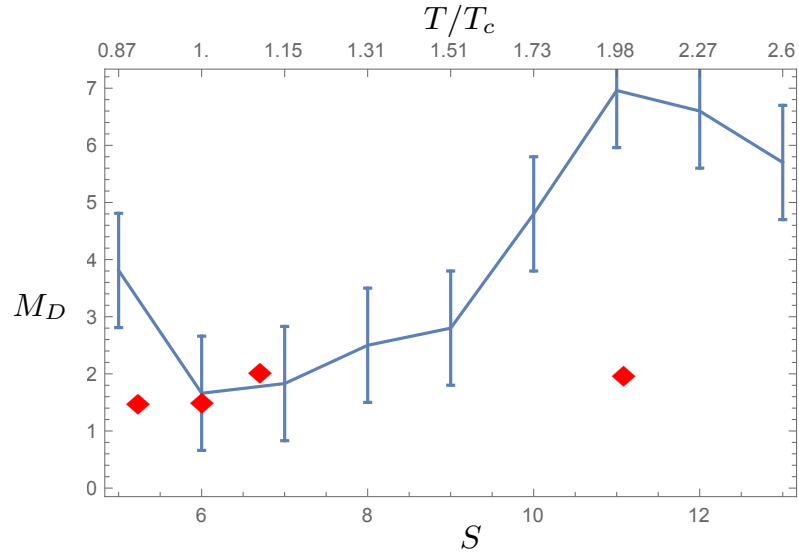


Figure 20: Self-consistent value of the Debye Mass M_D as a function of action S (lower scale) which is related to T/T_c (upper scale). The error bars are estimates based on the fluctuations of the numerical data. Points represent lattice data from [47] as a function of T/T_c .

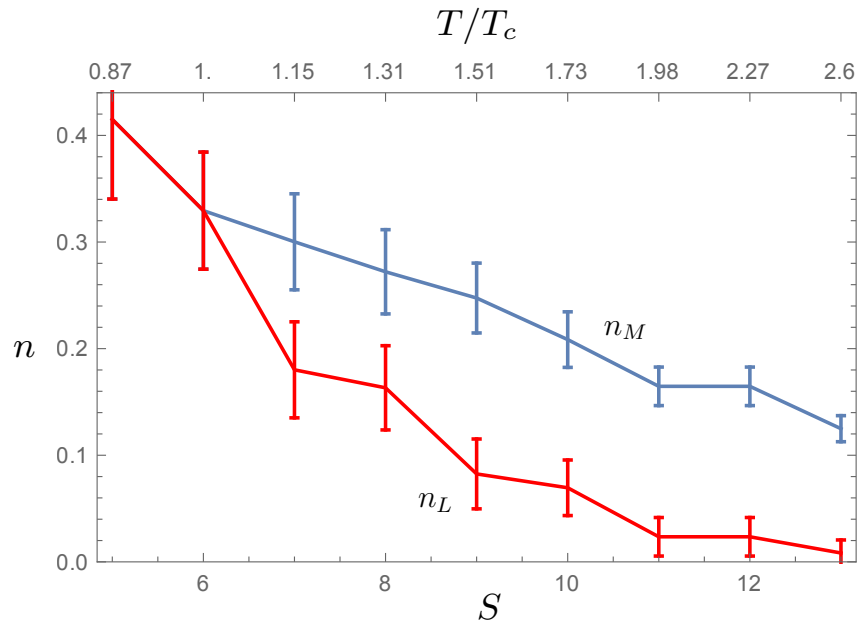


Figure 21: Density n of M and L dyons as a function of action S (lower scale) which is related to T/T_c (upper scale) for M dyons (higher line) and L dyons (lower line). The error bars are estimates based on the density of points and the fluctuations of the numerical data.

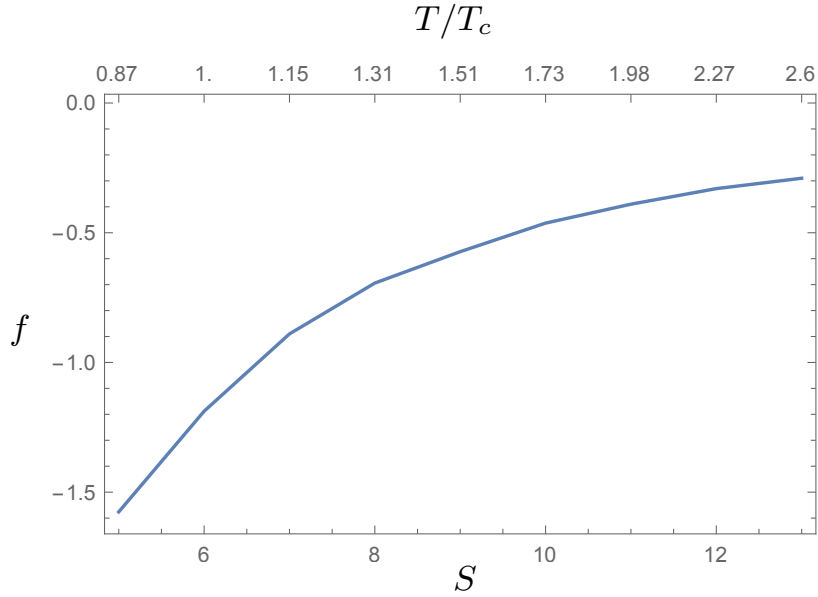


Figure 22: Self-consistent value of the free energy density f as a function of action S (lower scale) which is related to T/T_c (upper scale).

When we are in the confined region we observe the free energy for a fixed density as a single minimum in the middle at $\nu = 0.5$. As the action S increases, the density of dyons decrease and it becomes more favorable to have some bigger, but lighter dyons, thus shifting the minimum away from the confining value of the Polyakov loop, $P = 0$, as can be seen in Fig. 23 for $S = 6, 7, 9$. This, at the same time, makes the lighter M dyons more abundant than the more heavy L dyons.

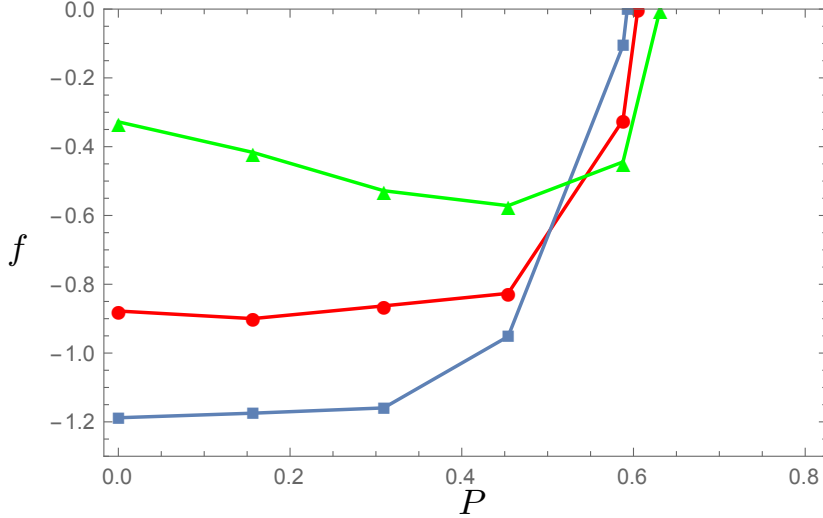


Figure 23: (Not-self-consistent in holonomy ν) free energy density f , here shown as a function of the value of the holonomy (in form of the Polyakov loop P) at $S = 6, 7, 9$. The lower the action the lower the minimum of the free energy.

Due to the size of the Debye mass, the correlation functions behaves as a liquid with a cutoff at small range. We show the case for $S = 6$ in Fig. 24 for MM and ML . Note the correlation function C_{MM} vanishes at small distances due to the core. The other correlation function C_{ML} for ML , displays attraction even at small distances, tripling the density at $r = 0$. For $S = 6$, the integrated number of particles in the region in which the correlation function $C_{ML}(r) > 1$ is 0.50 particles, while for C_{MM} it corresponds to 0.34 particles: thus the difference is not that large.

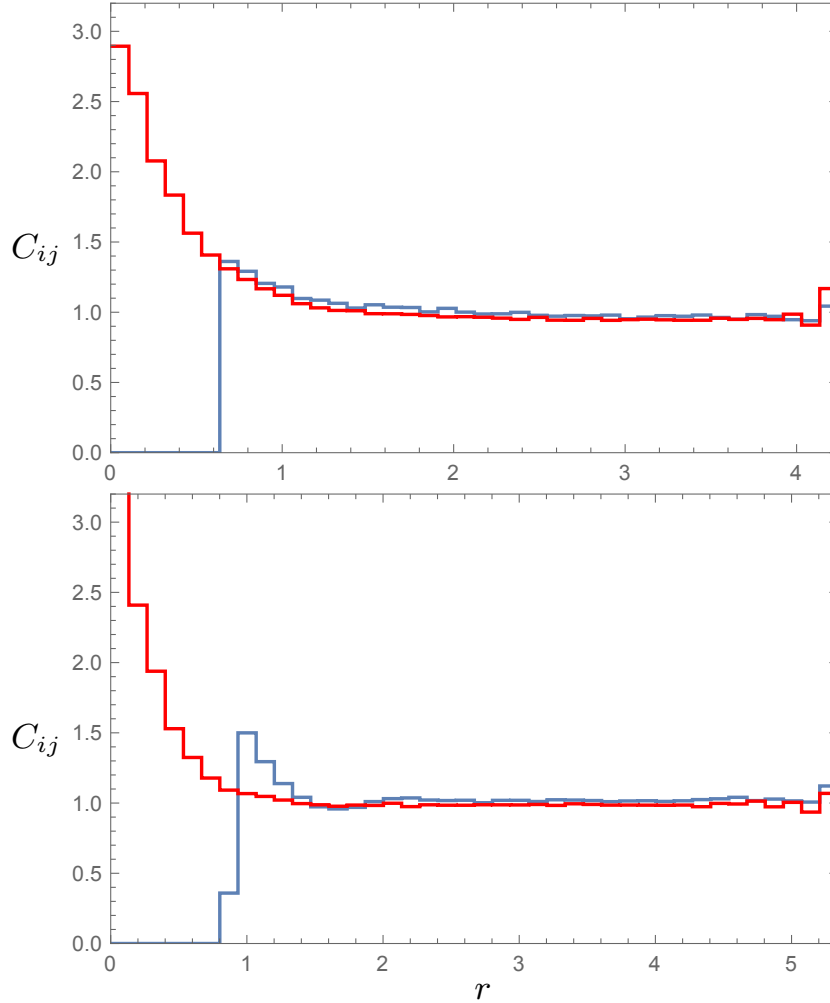


Figure 24: Correlation function C_{ij} for MM and ML for $S = 6$ (upper) and $S = 9$ (lower). In the *MM* case the correlation function vanishes at small distances due to the core.

5.9 Possible improvements

In this round of simulations we have been able to describe how the deconfinement phase transition happens. We were reaching for a self-consistent description of the system, in which all parameters are at the values corre-

sponding to the free energy minima.

Yet the self-consistency of the calculation remains in a way incomplete. In this subsection we make one more step towards it, but, as we will soon see, further ones may perhaps be needed.

We started this work with an idealized classical solution minimizing classical Yang-Mills action, the BPS solution, with zero holonomy potential. Quantum fluctuations in one-loop order generates the GPY potential. Furthermore, our ensemble of many dyons also contribute, resulting in a potential displaying confinement. The calculated Debye mass is of the right magnitude.

One may now wonder how the presence of the holonomy potential affects the dyon solution itself. Let us add a (simplified) potential

$$V_{MD} = \frac{M_D^2}{2} \left(v - \frac{1}{2} \text{Tr}(\tau_3 U_4) \right)^2 \quad (138)$$

and look for the action minimum. For technical reasons, instead of solving nonlinear differential equations, we minimized the action using the gradient flow for a single dyon on the lattice. The resulting action as a function of the Debye mass is shown in Fig. 25 and the shape of the solutions in Fig. 26. One can see, that the role of a nonzero Debye mass is to suppress the tails of the fields. This, in turn, somewhat increases the action.

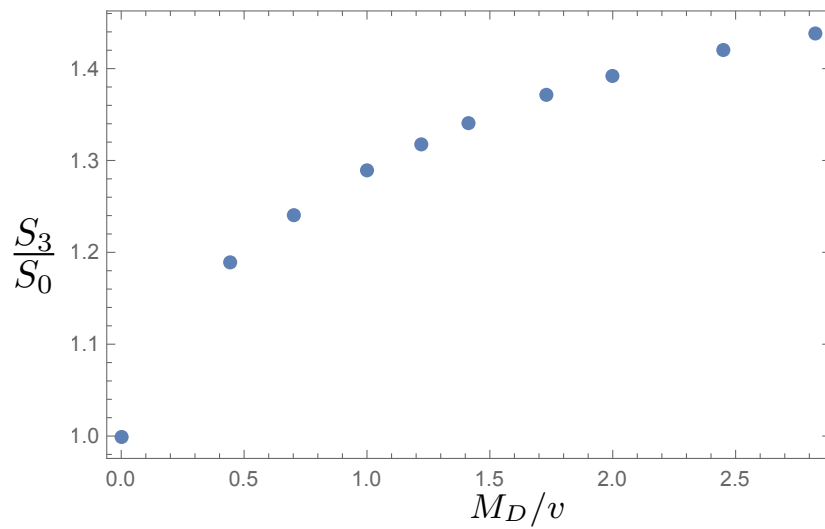


Figure 25: Action S_3 of a single dyon as a function of Debye mass over holonomy M_D/v in the potential described by eq. (138) normalized by the action S_0 for $M_D = 0$.

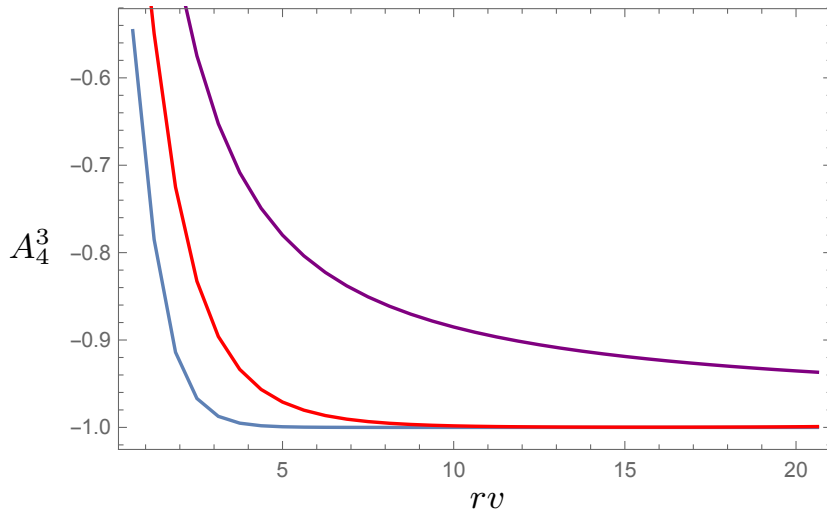


Figure 26: Higgs field A_4^3 of a single dyon, along the z -axis, through the center of the dyon for different Debye masses. From top to bottom: $M_D/v = 0$, $M_D/v = 0.45$ and $M_D/v = 1.41$.

To illustrate the effect of the increased dyon action on the ensemble, consider an example. For the confined holonomy $\nu = 0.5$ at T_c with $M_D = 3$ we get an action of 32 per dyon, compared to 25 for $M_D = 0$. As a result the free density of dyons becomes 2.3 times smaller.

Further improvements may be done including higher order quantum corrections. We have just demonstrated that the action and size of a dyon are modified by the holonomy potential. Obviously, other ingredients, such as the zero mode metric and the nonzero mode determinant, are modified as well.

Another important observation is the following. For the pure holonomy, in the bulk, the field strengths and thus classical action are zero. The GPY potential is non-zero as a result of a one loop calculation [42]. Two-loop correction has been calculated recently [48] and the result is proportional to the first order result, with the factor $1 - 5/S + \dots$, where $S = 8\pi^2/g^2$. One finds therefore that for the values of the parameter $S \sim 6 - 10$ we work with, this two-loop correction is not small: so the holonomy itself is *not* classical, it is subject to strong quantum fluctuations.

Two-loop and three-loop corrections to instantons are only calculated so far in quantum mechanical models, and similar calculations for gauge theory instantons and dyons are of interest. We do not expect those to be as large as for the holonomy potential: in quantum mechanics it is of the type $1 - 1/S$ instead.

6 Dyons and Fermions

In this section we focus on including fermions in the fundamental representation into the ensemble of interacting dyons.

The instanton-dyons have a certain number of zero modes prescribed by the topological index theorem. Topology ensures that any smooth deformation of the objects themselves does not shift fermionic eigenvalues from zero. The fermions will be included through the corrections to fermionic zero modes due to overlap between self-dual and anti-self-dual sectors, which break the zero modes and create a zero mode zone (ZMZ), when the ensemble is dense enough. The main physical phenomenon associated with ZMZ is the spontaneous breaking of the $SU(N_f)$ chiral symmetry, “chiral breaking” for short. For an ensemble of instantons, this phenomenon has been studied in great detail in the 1980s and 1990s, for a review see [9].

Physical (antiperiodic in time direction) fermions have zero modes on the L dyons. The zero modes produce the simplest effect of the dynamical fermions, binding of the $\bar{L}L$ dyon pairs into “molecules”, studied by Shuryak and Sulejmanpasic [39]. The first numerical simulations with fermions were done by Faccioli and Shuryak [33], who studied 1, 2 and 4 flavor theory with the $SU(2)$ color: they found chiral symmetry breaking in the first two cases, but the last one, $N_f = 4$ appeared marginal. Many technical aspects in this section follows their setting.

We follow the idea in these paper in order to obtain the chiral condensate from the eigenvalue distribution of the zero mode zone. Since the simulations were done at finite volume, there are finite volume effects on the eigenvalue distributions that affect the chiral condensate, which we have to understand. We obtain the shape of the zero mode zone and finite volume effects from random matrix theory, which enable us to extract the chiral condensate from the volume scaling behavior of the zero mode zone. Similar to previous section, we then find the dominating free energy, which give the Polyakov loop and density of dyons and now also the chiral condensate as a function of coupling constant/temperature.

This section is structured as follows: in section 6.1 we describe the physics of the fermionic zero modes and the technical tool, the hopping matrix, used to evaluate the fermionic determinant. We then explain the general setting of the interactions in section 6.2. After that we show how the chiral condensate is obtained from the eigenvalue distribution in section 6.3 and the mass gap

is discussed in section 6.3.3. The data sets used and how they were analyzed are explained in section 6.4. We end with the physical results in section 6.5, where we show, among others, the Polyakov loop and the chiral condensate's dependence on temperature.

6.1 The Zero Mode Zone

The main approximation made by us, similar to what was done in the instanton ensemble, is that the set of all fermionic states is translated to the subspace spanned by zero modes.

In this subspace, the determinant of the Dirac operator can be viewed as a sum of closed fermionic loops with “hopping amplitudes” between dyons and antidyons. Since sectors that are self-dual or anti-self-dual have its eigenvalues protected, then the overlap of L and L dyons or \bar{L} and \bar{L} dyons have to be zero. The resulting form of the “hopping matrix” is

$$\hat{\mathbf{T}} \equiv \begin{pmatrix} 0 & \mathbf{T}_{ij} \\ -\mathbf{T}_{ji} & 0 \end{pmatrix}. \quad (139)$$

Each of the entries in \mathbf{T}_{ij} is a “hopping amplitude” for a fermion between the i -th L -dyon and the j -th \bar{L} -antidyon. The diagonal matrix elements are zero, and therefore a single or many infinitely-separated dyons will have zero determinant and “veto” such configurations. However, nonzero non-diagonal hopping matrix elements make the determinant nonzero.

We define the individual hopping amplitude as the matrix element of the Dirac operator between different zero mode eigenfunctions

$$T_{ij} = \langle i | \not{D} | j \rangle, \quad (140)$$

where i and j are zero modes belonging to i -th L and j -th \bar{L} dyons. If the gauge field in the Dirac operator is a sum of two dyons, using the equations of motion for both zero modes, one can reduce the covariant derivative to the ordinary derivative.

Including a mass term, changes the hopping matrix by a constant m times the identity matrix.

Compared to section 5, the only addition to the partition function used in this section, is the determinant of the Dirac operator for N_f flavors, approximated by the determinant of the hopping matrix

$$\left(\det(\hat{\mathbf{T}}) \right)^{N_f}. \quad (141)$$

Basically, $\det(\hat{\mathbf{T}})$ can be seen as a set of loop diagrams, connecting all L-dyons and antidyons of the ensemble. It can either be dominated by short loops, including small number (2,..) dyons, to be referred to as a “molecular regime”, or by very long loops, including finite fraction of the ensemble (“collectivized regime”). The former has unbroken and the latter broken chiral symmetry. It is the purpose of our simulations to determine, as a function of the dyon density, the weights of such short and long loops.

6.1.1 The hopping amplitudes

We follow [39] and use a simple interpolation formula

$$T_{ij} = c \frac{e^{-\bar{v}r/2}}{\sqrt{1 + \bar{v}r/2}}, \quad (142)$$

where $\bar{v} = 2\pi T - v$. Based on a change of variable it has been found that the constant c should depend on holonomy as \bar{v} which gives

$$T_{ij} = \bar{v}c' \frac{e^{-\bar{v}r/2}}{\sqrt{1 + \bar{v}r/2}}. \quad (143)$$

Of course there are many other ways one can choose T_{ij} such that it in the large r limit on a log scale goes as $\bar{v}/2$. We therefore tried to obtain the shape and constant c' from doing first order perturbation theory.

By doing a first order correction, it was found that the factor c was dependent on the orientation of the Dirac string, since it was not fixed. The overlap without any of the gauge transformations explained in section 4 was therefore used to understand the shape. The integral done was

$$\int d^3x \psi(r_2)\psi(r_1)\left(\frac{H(r_1)}{2} + K(r_1)\right), \quad (144)$$

where H and K are the part of A_4 and A_i respectively that only depends on distance and not direction, as shown in [39]. $\psi(r)$ is the amplitude of the zero mode solution in [39]. The shape found to correspond very well to the integral was

$$T_{ij} = \bar{v}c' \exp\left(-\sqrt{11.2 + (\bar{v}r/2)^2}\right). \quad (145)$$

We will therefore also look into what kind of effect this choice of T_{ij} has.

We compare the two choices in Fig. 27.

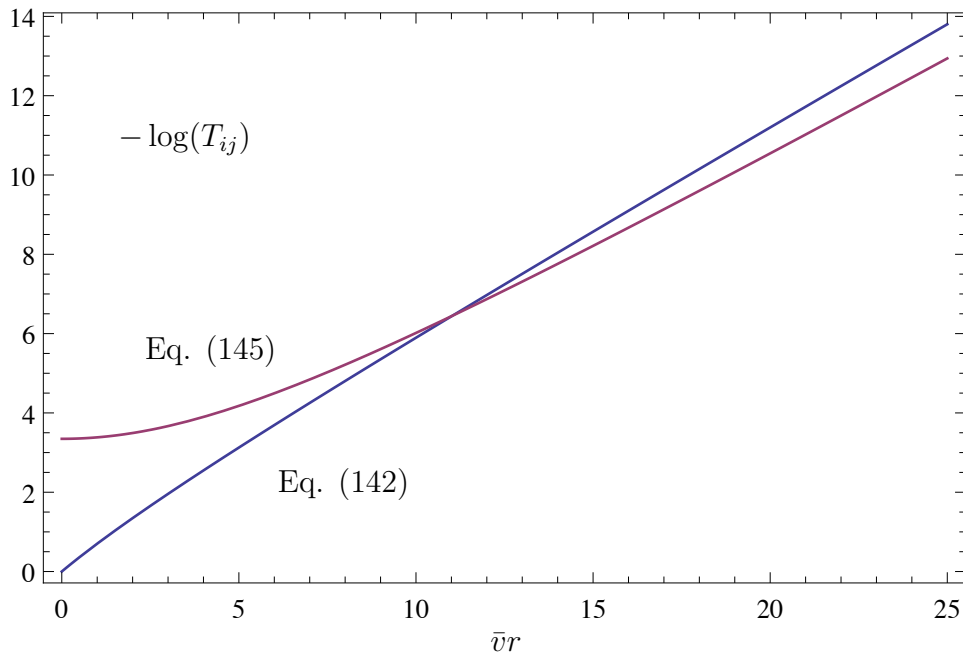


Figure 27: The matrix element of the hopping matrix, as $-\log(T_{ij})$ versus the distance, in units of \bar{v} . The two different curves corresponds to eq. (142) and (145), respectively.

6.2 The general setting

The setup is almost the same as in section 5, with the difference being the inclusion of the fermionic determinant in the zero modes approximation. This factor creates an additional fermion-induced interaction between the L type dyons.

The dimensionless holonomy $\nu = v/(2\pi T)$ is related to the expectation value of the Polyakov loop through the ($SU(2)$) relation

$$P = \cos(\pi\nu). \quad (146)$$

We seek to minimize the free energy

$$f = \frac{4\pi^2}{3}\nu^2\bar{\nu}^2 - 2n_M \ln \left[\frac{d_\nu e}{n_M} \right] - 2n_L \ln \left[\frac{d_{\bar{\nu}} e}{n_L} \right] + \Delta f, \quad (147)$$

where the first term is the perturbative Gross-Pisarski-Yaffe-Weiss holonomy potential, the next terms contain semiclassical independent dyon contributions, with

$$d_\nu = \Lambda \left(\frac{8\pi^2}{g^2} \right)^2 e^{-\frac{\nu 8\pi^2}{g^2}} \nu^{\frac{8\nu}{3}-1} / (4\pi) \quad (148)$$

and $\Delta f \equiv -\log(Z_{changed})/\tilde{V}_3$ is defined via the partition function studied numerically

$$Z_{changed} = \frac{1}{\tilde{V}_3^{2(N_L+N_M)}} \int D^3x \det(G) \exp(-\Delta D_{DD}(x)) \times \prod_i \lambda_i^{N_f}. \quad (149)$$

The last factor is the fermionic determinant, now written as the product of all eigenvalues of the hopping matrix $\hat{\mathbf{T}}$.

We just remind the expressions here without too many comments.

$$G = \delta_{mn} \delta_{ij} (4\pi\nu_m - 2 \sum_{k \neq i} \frac{e^{-M_D T |x_{i,m} - x_{k,m}|}}{T |x_{i,m} - x_{k,m}|} + 2 \sum_k \frac{e^{-M_D T |x_{i,m} - x_{k,p \neq m}|}}{T |x_{i,m} - x_{k,p \neq m}|}) + 2\delta_{mn} \frac{e^{-M_D T |x_{i,m} - x_{j,n}|}}{T |x_{i,m} - x_{j,n}|} - 2\delta_{m \neq n} \frac{e^{-M_D T |x_{i,m} - x_{j,n}|}}{T |x_{i,m} - x_{j,n}|}. \quad (150)$$

Dyon 2-point interactions ΔD_{DD} is a sum over all classical corrections for the different dyon to dyon combinations

$$\Delta D_{DD} = \sum_{j>i} \Delta S_{D_i D_j}, \quad (151)$$

where $\Delta S_{D_i D_j}$ is the correction to the action between dyon i and dyon j . If the two dyons are a dyon and its antidyon, we have for distances larger than x_0

$$\begin{aligned}\Delta S_{D\bar{D}} &= -2 \frac{8\pi^2\nu}{g^2} \left(\frac{1}{x} - 1.632e^{-0.704x} \right) e^{-M_D r T} \\ x &= 2\pi\nu r T.\end{aligned}\tag{152}$$

For the rest of the combinations we have

$$\begin{aligned}\Delta S_{DD} &= \frac{8\pi^2\nu}{g^2} \left(-e_1 e_2 \frac{1}{x} + m_1 m_2 \frac{1}{x} \right) e^{-M_D r T} \\ x &= 2\pi\nu r T,\end{aligned}\tag{153}$$

where the charge is given by Table 3. For distances smaller than x_0 we have a core between dyon pairs of the types LL , MM , $\bar{L}\bar{L}$, $\bar{M}\bar{M}$, $L\bar{L}$ and $M\bar{M}$

$$\begin{aligned}\Delta S_{DD} &= \frac{\nu V_0}{1 + \exp[\sigma T(x - x_0)]} \\ x &= 2\pi\nu r T,\end{aligned}\tag{154}$$

where x_0 is the size of the dyons core. We work with $x_0 = 2$. It is important to note that for M type dyons one has to use ν and for L type dyons one has to use $\bar{\nu} = 1 - \nu$.

	M	\bar{M}	L	\bar{L}
$g^2 S_{cl}/(8\pi^2)$	ν	ν	$1 - \nu$	$1 - \nu$
Q_T	ν	$-\nu$	$1 - \nu$	$\nu - 1$
e	1	1	-1	-1
m	1	-1	-1	1

Table 3: (Same as Table 1) Quantum numbers of the four different kinds of instanton-dyons for $SU(2)$ gauge theory. The rows are classical action S_{cl} , topological charge Q_T , electric charge e and magnetic charge m . The antidyons have a bar over the letter.

6.3 Eigenvalue distributions and the chiral condensate

The Banks-Casher relation tells us that in the infinite volume limit, the chiral condensate for massless fermions is proportional to the density of eigenvalues at zero value

$$| \langle \bar{\psi} \psi \rangle | = \pi \rho(\lambda)_{\lambda \rightarrow 0, m \rightarrow 0, V \rightarrow \infty}. \quad (155)$$

For any system with a finite volume, the typical size of small eigenvalues is of size $1/V$ and the density will always be 0 at $\lambda = 0$ and $m = 0$. We see this behavior in our ensemble as seen for zero mass in Fig. 28 and 29. We also find that a finite mass, as in Fig. 30 and 31, has the effect of allowing eigenvalues around zero, and if the mass is large enough, smooth the maximum of the eigenvalue distribution into the region around $\lambda = 0$.

To understand finite volume effects on the distribution, one may study those using chiral random matrix theory, for review see [34]. In principle, using expressions obtained in this framework one can recover the value of the chiral condensate in the infinite volume case.

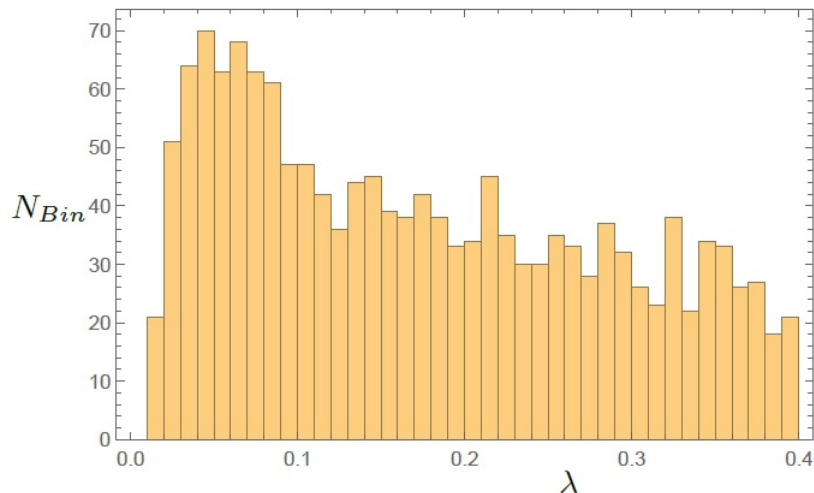


Figure 28: Eigenvalue distribution for $n_M = n_L = 0.47$, $N_F = 2$ massless fermions at $S = 7$.

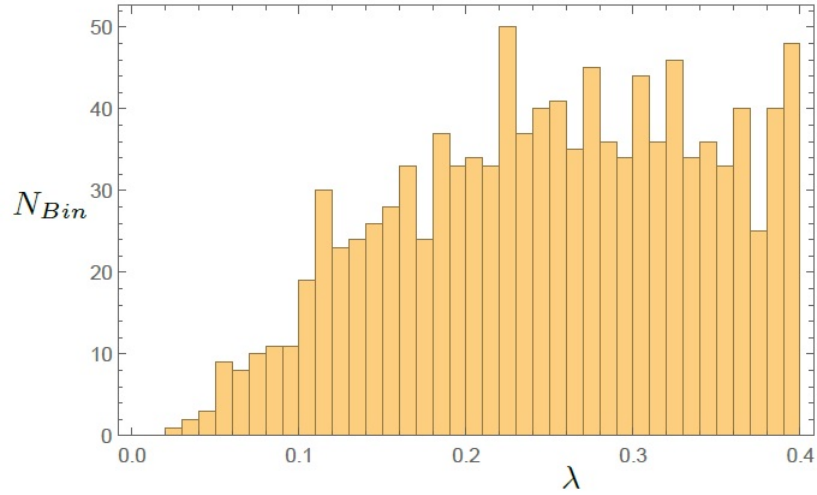


Figure 29: Eigenvalue distribution for $n_M = n_L = 0.08$, $N_F = 2$ massless fermions at $S = 7$.

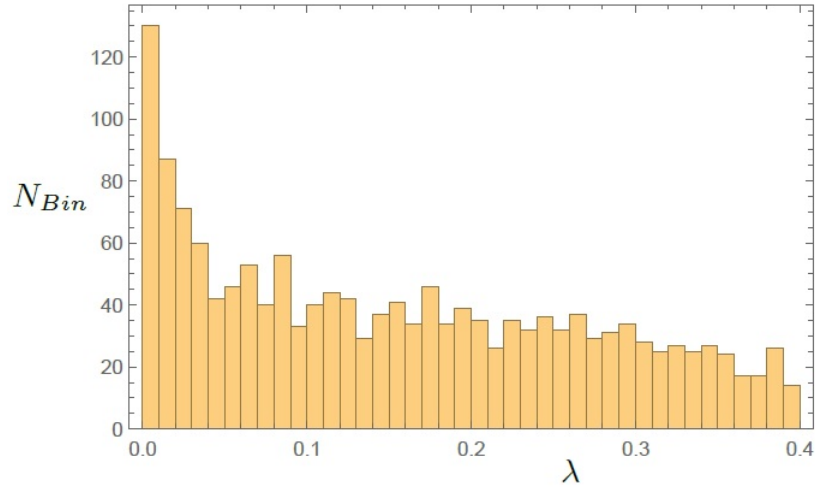


Figure 30: Fermionic eigenvalue distribution for $n_M = n_L = 0.47$, $N_F = 2$, $m = 0.01$ at $S = 7$.

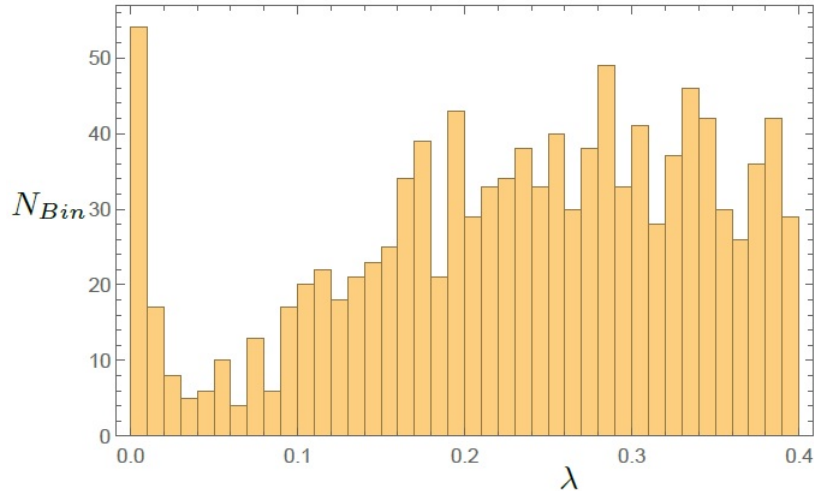


Figure 31: Fermionic eigenvalue distribution for $n_M = n_L = 0.08$, $N_F = 2$, $m = 0.01$ at $S = 7$.

We will be determining the chiral condensate by two different methods:

(i) The first one is based on the part of the eigenvalue distributions with the smallest λ . It requires an understanding of the *finite volume* effects on the distribution. This understanding we obtain from analytic random matrix results. We explain this approach in section 6.3.1.

Vanishing of the condensate is used to define the ensemble parameters corresponding to chiral symmetry breaking transition, $T_{\bar{\psi}\psi}$.

The second strategy (ii) we will use, is based on the determination of the so called *gap width* in the distribution, near $\lambda = 0$: we will refer to it as T_{gap} . This approach is explained in section 6.3.3.

Ideally, both critical temperatures should coincide, defining the temperature of chiral symmetry breaking T_χ .

6.3.1 The finite size effects

To understand finite volume effects we performed simulations for 64 and 128 dyons, at the same density. (The volume of the sphere with 128 dyons being 2 times larger than the sphere of the 64 ones.) The quark mass in both simulations were set to zero. An example of the resulting eigenvalue distributions are shown in Fig. 32.

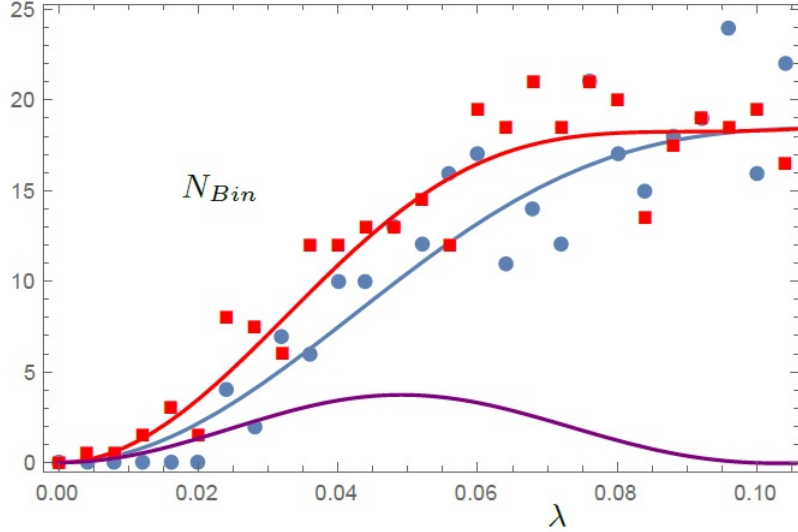


Figure 32: The points are the eigenvalue distribution for 64 (blue circles) and 128 (red squares) dyons at $S = 8$ and density of dyons $n_M = 0.33$, $n_L = 0.20$, $N_F = 2$. The curves are the fit with eq. (156) with $\Sigma_{2,64} = 1.30 \pm 0.06$ and $\Sigma_{2,128} = 1.28 \pm 0.06$ and the scaling as $\Sigma_{1,64} = 0.79 \pm 0.05$ and $\Sigma_{1,128} = 0.51 \pm 0.04$ for these two cases, respectively. The lower purple line is the difference between the two fits. Eq. (157) gives $\Sigma = 0.38 \pm 0.13$, while the maximum of the difference between the two curves gives $\Sigma = 0.3$ after normalizing the difference with the volume (note: This approach of using the maximum of the difference between the two volumes, has not been used to analyze the data, but is simple used here to visualize the effect).

We fit the distribution of the eigenvalues with the form taken from random-matrix theory [34] for $SU(2)$ gauge group for massless fermions given by

$$\rho(x) = V\Sigma_2 \left[\frac{x}{2} (J_2(x)^2 - J_1(x)J_3(x)) + \frac{1}{2} J_2(x) \left(1 - \int_0^x dt J_2(t) \right) \right], \quad (156)$$

where $x = \lambda V \Sigma_1$ and J_n are the Bessel functions. Both the scaling factor $V \Sigma_1$ and the overall factor $V \Sigma_2$ should be proportional to the value of the chiral condensate Σ . In the limit $V \rightarrow \infty$ the formula gives $\rho(0) \propto V \Sigma_2$ as required.

Ideally, the parameter values for two different volumes should agree. When the fits for different volumes were done, we found that the values for parameter Σ_2 agree very well indeed. (This is related to the fact that the height of the distributions at the r.h.s. of Fig. 32 do agree.)

Note that the main difference between the two distributions is a shift to the left for bigger volume. This is expected in larger volume clusters of a condensate inside which quark propagation gets larger, and the eigenvalues smaller. The formula from random matrix theory, prescribes a particular “mesoscopic” scaling with the volume. However, the fit by this formula produces values of Σ_1 which are not the same. This indicates that, at least our smaller volume, is not yet in the range in which the expected large volume scaling applies.

The physics behind this behavior is as follows: there are basically two components of the ensemble, generating two different dependencies on the volume. As we already mentioned in the introduction, there is collectivized dyons, producing the condensate, and dyon-antidyon pairs. The former component produces eigenvalue distribution shifting with the volume, while the latter contribution is volume-independent .

The existence of two components lead us to construct a value of Σ out of all four parameters of the fit given by

$$\Sigma = \Sigma_2(2\Sigma_1^{128}/\Sigma_1^{64} - 1). \quad (157)$$

In the case of only almost zero modes, from the collectivized dyons, doubling the volume should double $V\Sigma_1$. In the opposite case of only dyon-antidyon pairs, $V\Sigma_1$ should be unchanged. As can be seen in Fig. 32 the situation is sometimes in between the two extremes. The expression (157) is an interpolation between the two regimes. This resulting value of Σ will be used in the plots to follow, such as showing the temperature dependence of the condensate. We show Σ_2 , $2\Sigma_1^{128}/\Sigma_1^{64} - 1$ and Σ for the results in section 6.5.1 in Fig. 33.

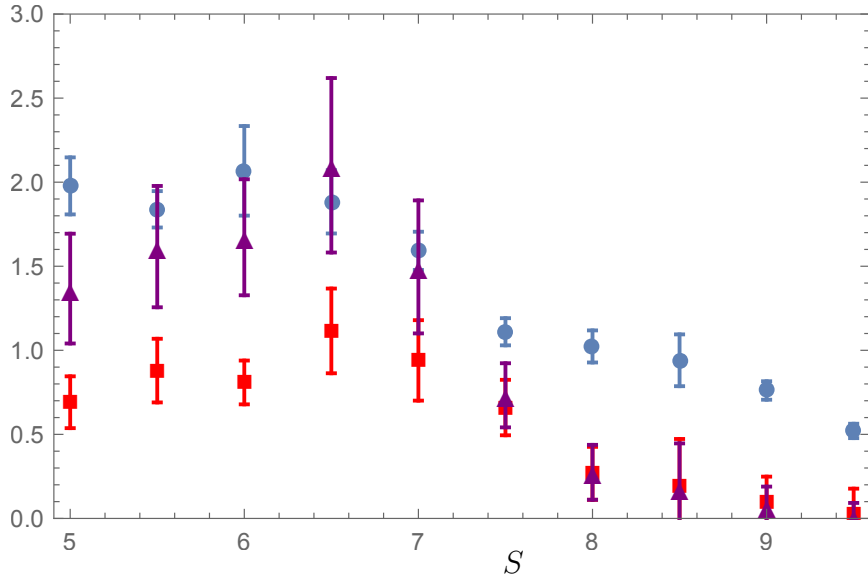


Figure 33: Σ_2 (blue circle), $2\Sigma_1^{128}/\Sigma_1^{64} - 1$ (red square) and Σ (purple triangle) as a function of input action $S = 8\pi^2/g^2$ for the results in section 6.5.1. It is observed how the rise in Σ_2 and $2\Sigma_1^{128}/\Sigma_1^{64} - 1$ are correlated, while, $2\Sigma_1^{128}/\Sigma_1^{64} - 1$ goes to zero for higher S while Σ_2 does not. Condensates are scaled by 0.5.

As the density increases, it is seen how the scaling becomes closer and closer to that of the volume, as expected from eq. (156), such that the limit to infinite volume gives the chiral condensate as $\rho(0)$.

6.3.2 The effect of the quark mass

Nonzero quark mass moderates the distribution of the smaller eigenvalues. Furthermore, for $\lambda < m$ the fermions are effectively decoupled, and thus the distributions should be the same as for a quenched (no dynamical quarks) theory. The latter is known to produce a singularity at $\lambda \rightarrow 0$ observed in the instanton liquid simulations and on the lattice already in the mid-1990s.

Our simulations with the mass 0.01 produce eigenvalue distributions shown in Fig. 30 and 31. Note that, in contrast to the zero mass case, one finds a peak near zero eigenvalue. Eigenvalues outside of the range of the mass, $\lambda > m$ behave as in the massless case, as can be seen by comparing to Fig. 28 and 29. In the range of $\lambda = m$, the distribution is smoothed due to the

singularity at $\lambda \rightarrow 0$. The same behavior is seen on the lattice [49], even when a gap appears.

6.3.3 Gaps of the eigenvalue distribution

At high temperatures, or very dilute dyon ensembles in our model, the chiral symmetry remains unbroken. As it has been shown in multiple lattice simulations, in this case the Dirac eigenvalue distribution develops a finite gap, between $\lambda = 0$ and the point where the eigenvalue distribution starts to rise. Vanishing of this gap therefore provides another way of observing the location of chiral symmetry breaking. Not to confuse it with the critical temperature of chiral symmetry breaking. Not to confuse it with the critical temperature obtained from the other method, we call this temperature T_{gap} .

The procedure used is explained by an example shown in Fig. 34: we fit the distribution by a straight line, and use its intersection with the x-axis as the measure for the gap.

The fact that a gap appears, means that the lowest excitations are not massless.

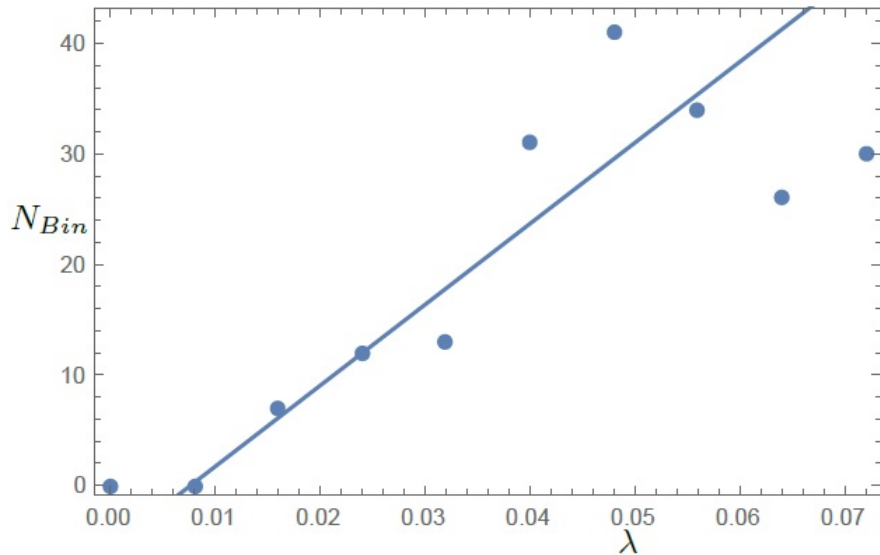


Figure 34: The eigenvalue distribution for 64 dyons at $S = 7.5$, $\nu = 0.434$, $N_F = 2$, $n_M = 0.43$ and $n_L = 0.22$. A straight line has been fitted through point 3 to 6 from the left. The gap size is defined as the cross point with the x-axis.

6.4 Data and analysis

The setting has already been explained above. An “update cycle” is defined as a sequence of Metropolis updates of all coordinates of all dyons. Each “run” consisted of 4000 such “update cycles”, out of which the typical thermal relaxation time was of the order of 500 cycles. The “useful data” selected were the mean action values collected for the last 1000 cycles.

The free energy of the model, depending on its parameters, is determined from the integrated expectation value of the action $\langle S(\lambda) \rangle$, following a standard approach

$$e^{-F(\lambda)} = \int Dx e^{-\lambda S} \quad (158)$$

$$F(1) = \int_0^1 \langle S(\lambda) \rangle d\lambda + F(0). \quad (159)$$

An example of the λ dependence of $\langle S(\lambda) \rangle$ is illustrated in Fig. 35. The quick descent in the expectation value of the action at small λ required more measurement points in the range $\lambda = 0..0.1$. We therefore had a step size of $1/90$ until $\lambda = 0.1$, while for larger lambda the step size is increased to 0.1 . These values, shown in the upper two rows of Table 4, constitute 19 runs.

The next three rows of Table 4 correspond to three parameters of the model used for free energy minimization. (Those are the value of the holonomy ν , the radius of the system defining the total dyon density and the number of M dyons N_M .) This three-dimensional space was explored systematically, in a lattice form defined by min and max values and a step defined in the Table. This was done for all values of the two remaining “input parameters”, the Debye mass M_d and classical action S . This gives 67200 different combinations.

	Min	Max	Step size
λ	0	0.1	1/90
λ	0.1	1.0	0.1
ν	0.175	0.525	0.025
r	1.05	2.00	0.05
N_M	16	26	2
M_d	3	6	1
S	5	9.5	0.5

Table 4: The input parameters used for the final run.

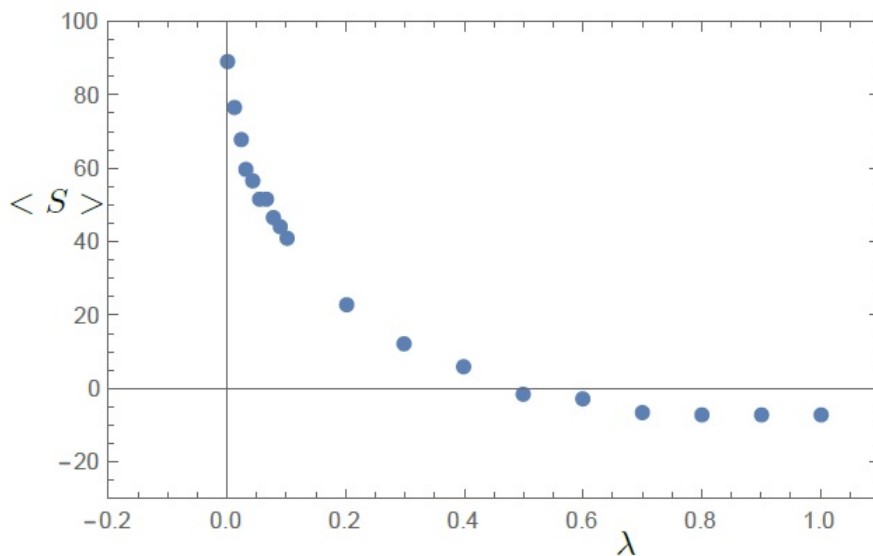


Figure 35: A typical example of the expectation values of the action $\langle S \rangle$ obtained from the simulation as a function of λ . Contribution to the free energy from the overall constant $F(0)$ is not included.

6.4.1 Data Analysis

After the integration over lambda is done, the values of the free energy for each combination of parameters are determined. The main part of the data analysis is the fit, defining dependence of the free energy in the 3-dimensional

space (of two dyon densities and holonomy) near its minimum. We therefore fit this set of data with a 3-dimensional parabola

$$f = (w - w_0)M(w - w_0) + f_0, \quad (160)$$

which has 10 variables. w and w_0 are 3D vectors with w containing the variables holonomy ν , radius r , and number of M dyons N_M and w_0 describing the correction to the point that were the minimum. M is a 3 times 3 matrix with $M = M^T$ containing the coefficients for the fit.

This expression was fitted to free energy values of $5^3 = 125$ points from a cube, containing 5 points around the minimum in each direction. The resulting values of the 10 parameters fitted are used as follows:(i) w_0 and its uncertainties give the values of densities and holonomy at the minimum, plotted as results below; (ii) the diagonal component of M in the holonomy direction was converted into the value of the Debye mass M_d . An additional requirement of the procedure, to make the ensemble approximately self-consistent, is that the Debye mass from the fit should be within ± 0.5 of the used input Debye mass value.

To obtain the chiral properties, such as the Dirac eigenvalue distributions and its dependence on dyon number and volume, we only used the “dominant” configurations for each action S , defined as follows. Since N_M is always an integer, we use the value closest to that obtained from the fit. The eigenvalue distributions are then analyzed as explained in section 6.3.

6.5 Physical Results

We use two parameterizations of the hopping matrix element. We perform simulations with both sets. The parameterizations themselves are explained in section 6.1.1. The physical results are, respectively, split up into two subsections, one for each choice of T_{ij} . Since the overall constant c' is unknown, values of c' have been chosen, such that the transition happens around $S = 7.5$. We are actively trying to obtain c' from numerical simulations. While the different T_{ij} 's behave similar for large distances, the behavior is different around zero. This also means that the constant c' can be different in the two cases. For these results c' was chosen such that the density of L dyons didn't become too small, while having a smooth Polyakov loop that went to zero in the range of $S = 5 - 10$.

The plots below have two scales, on their bottom and top. The former one shows the “instanton action” parameter S , one of the major parameters

of the model controlling the diluteness of the ensemble. We also indicate at the top the corresponding temperature, relative to the critical temperature T_c , chosen as $S = 7.5$. It should be noted that this is a choice, and is done in order to set a scale. The real input is the action S or the coupling constant g . The temperature is found from the running coupling constant.

$$S(T) = \frac{8\pi^2}{g^2(T)} = b \cdot \ln\left(\frac{T}{\Lambda}\right), \quad b = \frac{11}{3}N_c - \frac{2}{3}N_F. \quad (161)$$

This top temperature scale is approximate and should only be used for qualitative comparison to other models and lattice data.

6.5.1 Parameterization A for T_{ij}

The results in this subsection are for

$$T_{ij} = \bar{v}c' \exp\left(-\sqrt{11.2 + (\bar{v}r/2)^2}\right). \quad (162)$$

Minimizing the free energy gives the dominating parameters for a specific action S or Temperature T . This is done for $\Lambda = 4$ and $-\text{Log}(c') = -2.60$. This gives the holonomy, the density Fig. 36, and Debye mass Fig. 39. The dominating configurations have been analyzed using the methods described in section 6.3 in order to obtain the chiral condensate, which is shown together with the Polyakov loop in Fig. 37 and is also compared to the gap in Fig. 38.

We observe a smooth transition towards zero expectation value of the Polyakov loop P as temperature decreases. We also observe a non-zero value of the chiral condensate as temperature decreases. This is a more abrupt change, though in some way still smooth. Its inflection point (change of curvature) is found around $S = 7.5$, though the transition happens between $S = 6.5 - 8$. Below $S = 7$ the results fluctuate around a constant.

The chiral symmetry breaking can also be observed through the shrinking of the gap around zero as shown together with the chiral condensate in Fig. 38. Again, thinking of the inflection points of the two curves, we conclude from it that the critical temperature for the chiral condensate and the gap do coincide within errors, at the same $S = 6.5 - 8$ point.

Confinement and chiral symmetry are therefore different phenomena, but are both triggered by the increase in the density of dyons.

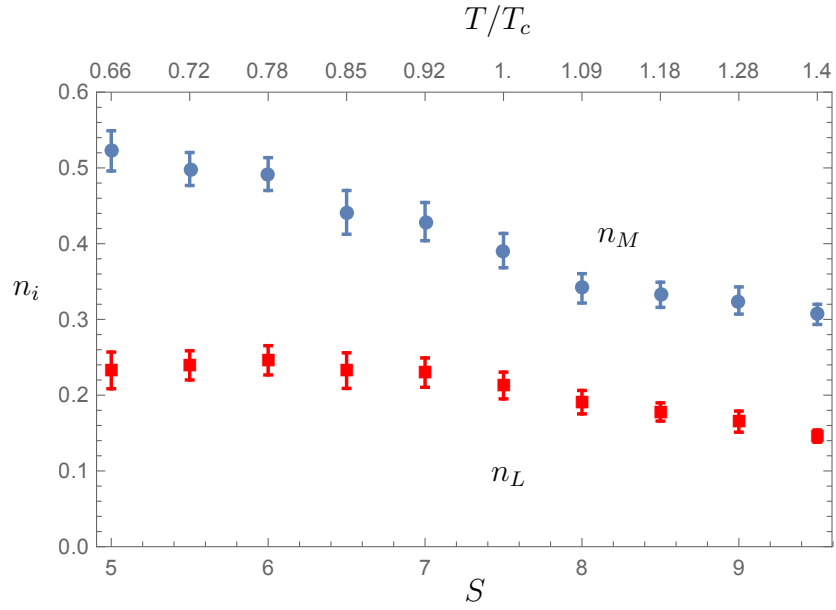


Figure 36: Parameterization A: The density of the M (blue circles) and L (red squares) dyons as a function of action $S = 8\pi^2/g^2$ or temperature T/T_c .

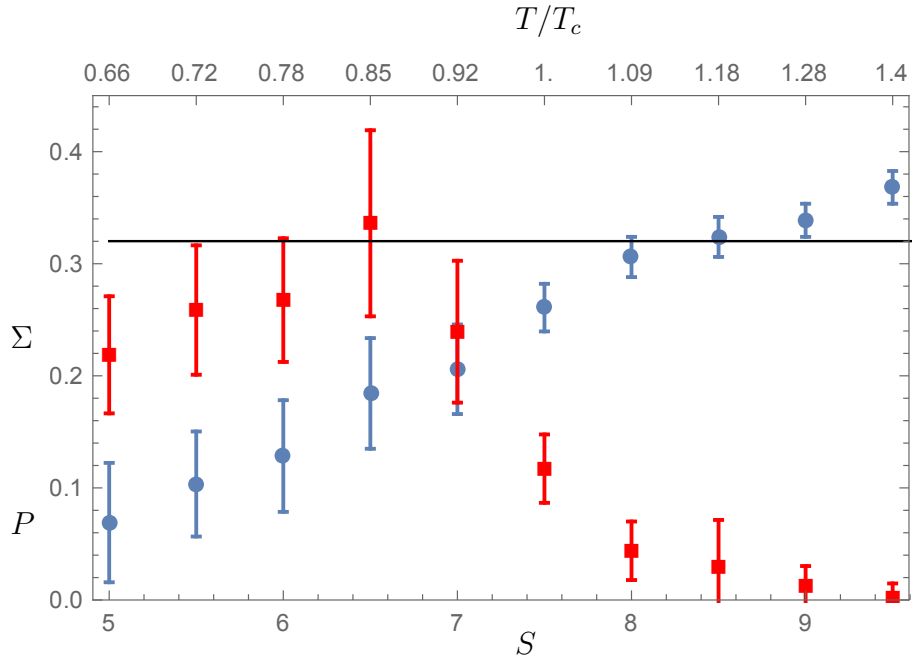


Figure 37: Parameterization A: The Polyakov loop P (blue circles) and the chiral condensate Σ (red squares) as a function of action $S = 8\pi^2/g^2$ or temperature T/T_c . A clear rise is seen around $S = 7.5$ for the chiral condensate. Σ is scaled by 0.08. The black constant line corresponds to the upper limit of Σ under the assumption that the entire eigenvalue distribution belongs to the almost zero mode zone, i.e. the maximum of Σ_2 .

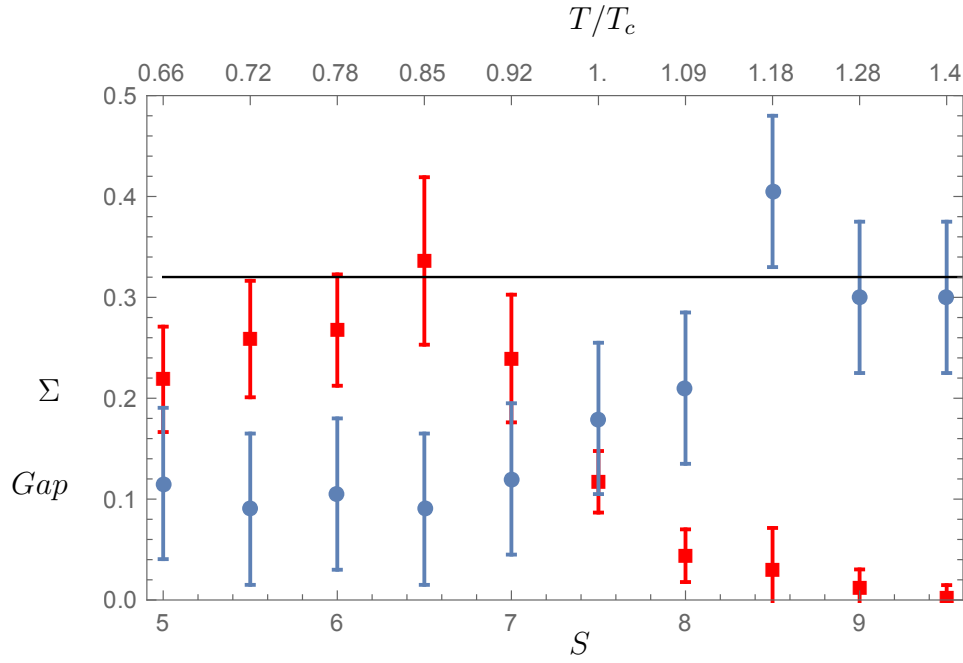


Figure 38: Parameterization A: The gap scaled up 15 times (blue circles) and the chiral condensate Σ (red squares) as a function of action $S = 8\pi^2/g^2$ or temperature T/T_c . A clear rise/fall is seen around $S = 7 - 7.5$. We get a critical temperature from $S = 6.5 - 8$ for the condensate and $S = 6.5 - 8$ for the gap. Σ is scaled by 0.08. The black constant line is defined in the caption of Fig. 37.

The Debye mass, Fig. 39, as compared to some lattice results [50], is seen to be around 66% too large. Newer lattice results [51] though show that the Debye mass might be larger than our obtained value.

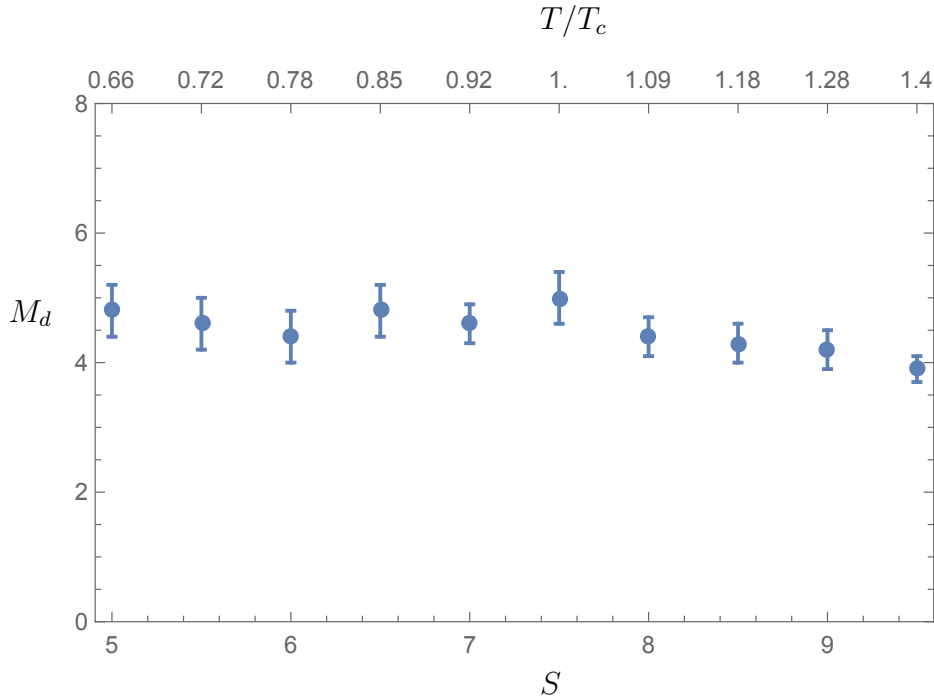


Figure 39: Parameterization A: Debye mass M_d as a function of action $S = 8\pi^2/g^2$ or temperature T/T_c .

6.5.2 Parameterization B for T_{ij}

The results in this subsection are for

$$T_{ij} = \bar{v}c' \frac{e^{-\bar{v}r/2}}{\sqrt{1 + \bar{v}r/2}}, \quad (163)$$

with $-\log(c') = -0.388$ and $\Lambda = 3.2$.

Just as for the other choice of T_{ij} discussed in the previous subsection, we obtain the parameters of density, Fig. 40, holonomy (Polyakov loop Fig. 41), and Debye mass, Fig. 43, as a function of temperature by minimizing the free energy. The chiral condensate Fig. 41 and 42, and gap width Fig. 42, have been obtained from configurations with the parameters obtained by minimizing the free energy. The main difference between the two choices of T_{ij} comes from the behavior around $r = 0$. The almost exponential behavior as shown in eq. (163), means that L dyons become more likely at high

densities. The other thing is that it is harder to make the different elements in T_{ij} of similar size, which results in a scaling behavior of the chiral condensate that only becomes around $37\% \pm 10\%$ of the volume, and not 100% as with parameterization A. This does not mean that the chiral condensate which we show in Fig. 41 does not exist, but it does mean that we need a larger volume in this case to obtain a cleaner result. It also means that the overlap between almost zero modes and dyon-antidyon pairs was larger.

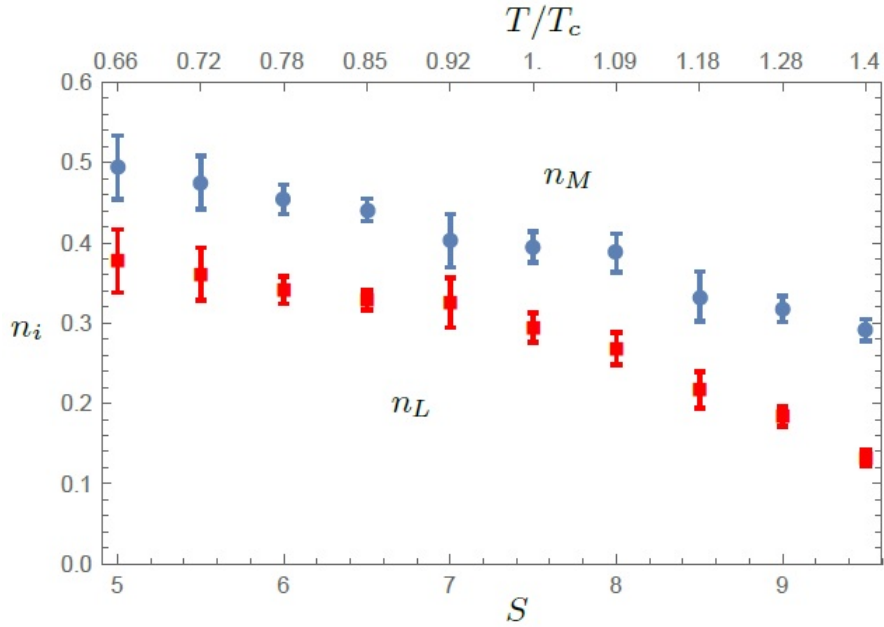


Figure 40: Parameterization B: The density of the M (blue circles) and L (red squares) dyons as a function of action $S = 8\pi^2/g^2$ or temperature T/T_c .

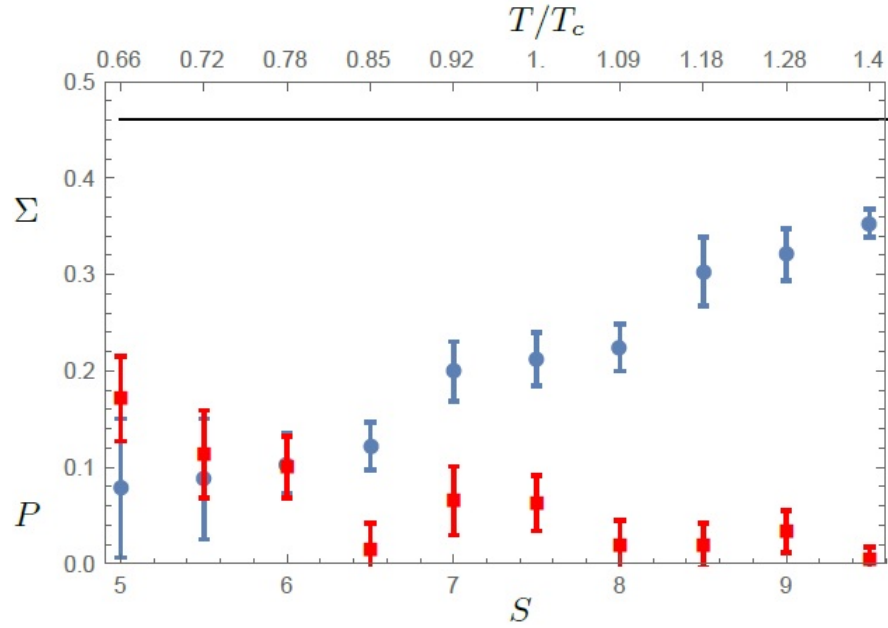


Figure 41: Parameterization B: The Polyakov loop P (blue circles) and the chiral condensate Σ (red squares) as a function of action $S = 8\pi^2/g^2$ or temperature T/T_c . Σ is scaled by 0.1. The black constant line is defined in the caption of Fig. 37.

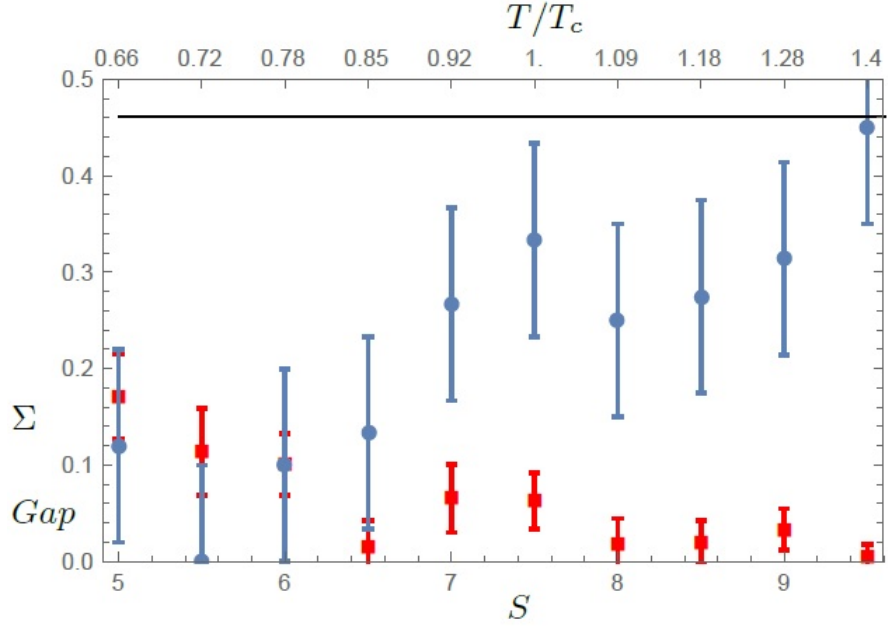


Figure 42: Parameterization B: The gap scaled up 20 times (blue circles) and the chiral condensate Σ (red squares) as a function of action $S = 8\pi^2/g^2$ or temperature T/T_c . A fall is seen around $S = 7$ for the gap, while it goes close to zero around $S = 5 - 6.5$. At $S = 5 - 6$ the chiral condensate starts to consistently become different from zero. It should be noted in this case that $2\Sigma_1^{128}/\Sigma_1^{64} - 1$ never becomes larger than $37\% \pm 10\%$. Σ is scaled by 0.1. The black constant line is defined in the caption of Fig. 37.

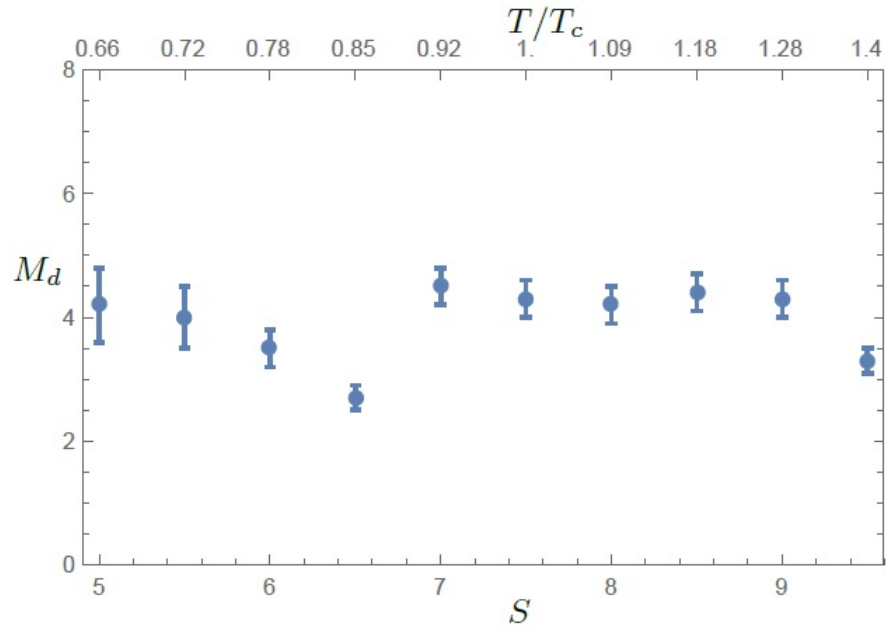


Figure 43: Parameterization B: Debye mass M_d as a function of action $S = 8\pi^2/g^2$ or temperature T/T_c .

7 Dyons and Boundary conditions

In this section we explore the effect of changing the boundary conditions of the fermions. We look at the Z_2 fermions in the standard representation in $SU(2)$ where one fermion flavor is anti-periodic and one fermion flavor is periodic. This changes the behavior of the zero modes of the dyons. We now have that each of the dyons have one zero mode, but with different flavors. This restores center symmetry and changes the behavior of the ensemble dramatically. The main results are again the Polyakov loop, the chiral condensate and the dyon densities as a function of coupling constant. We now have two chiral condensates, one for each flavor. We see that each of the chiral condensates behave as a one flavor chiral condensate, in both volume dependence and shape of the zero mode zone of fermionic eigenvalues.

7.1 Z_{N_c} -symmetric QCD and the instanton-dyons

Let us start this section by reminding that in the framework of the original instanton model most of the phenomena caused by changing the boundary conditions, would be impossible to explain. The number of zero modes of the instanton is prescribed by the topological index theorem and is independent on the periodicity condition.

On the other hand, after it has been recognized that instantons has to be split into instanton-dyons, the situations changes dramatically. Quarks with different boundary angles can be coupled to different types of dyons. Dialing different values of those angles, one can see the consequences from which it will eventually be possible to understand the dynamical role of those objects.

The “ Z_{N_c} -symmetric QCD” proposed by Kouna et al does indeed have outstandingly simple symmetry properties in the instanton-dyon model: *each quark flavor has zero modes with a different type of instanton-dyon*. This means that each quark flavor has its own “dyon plasma” with which it interacts. In this model the number of colors and flavors must match, $N_f = N_c$, so the number of quark and dyon types match as well.

Furthermore, in the low T , near and below T_{deconf} the holonomy values tends to the symmetric “confining” value, at which all types of the dyons obtain the same action. This fact indeed made the model Z_{N_c} -symmetric.

In the opposite limit of high T , the holonomy moves to a trivial value, and the actions of different dyons become distinct. This implies that each

quark flavor has its own “dyon plasma” with distinct densities, leading to flavor-dependent transition temperatures T_χ .

One more qualitative idea is related to the values of the holonomy at $\nu = z$ for $\psi(t + 1/T) = \psi(t) \exp(2\pi zi)$. Those are values at which the zero modes jump from one kind of dyon to the next. This happens by “delocalization” of the zero mode, which means that at such particular holonomy values the zero modes become long-range. Since in this case the “hopping” matrix elements, describing quark-induced dyon-dyon interactions, get enhanced, one may also expect that the chiral condensate is effectively strengthened.

7.2 The setting of the simulations

Let us remind the setting used in our simulations with instanton-dyons. Certain number of them, 64 or 128, are placed on the 3-dimensional sphere. Its radius thus control the density. Standard Metropolis algorithm is used to numerically simulate the distribution defined by classical and one-loop partition function. We study the simplest non-Abelian theory with two colors $N_c = 2$, which has a single holonomy parameter $\nu \in [0, 1]$. Free energy is calculated and the adjustable parameters of the model, the value of the holonomy ν and densities of M and L type dyons, are placed at the minimum.

In this section we work with one periodic flavor and one anti-periodic flavor, such that each dyon couple to a different flavor of quarks as explained in section 2.5.1. The partition function is therefore Z_2 symmetric, under $\nu \leftrightarrow \bar{\nu} = 1 - \nu$ and $M \leftrightarrow L$ replacement. A distinct *symmetric phase* has minimal free energy at the symmetric point $\nu = 1/2$, and equal number of L, M dyons. *Asymmetric phase* has free energy with two minima, away from the center $\nu = 1/2$: by default the spontaneous breaking of Z_2 is assumed to happen to smaller values of ν , so that at high T it goes to zero.

Following section 6 we use the following parameterization of the overlap between zero modes

$$T_{ij} = v_k c' \exp\left(-\sqrt{11.2 + (v_k r/2)^2}\right), \quad (164)$$

where v_k is $v = 2\pi\nu T$ for M dyons, and v_k is $\bar{v} = 2\pi\bar{\nu}T = 2\pi(1 - \nu)T$ for L dyons, due to the shape of the zero modes, as seen in section 2.5.1. The three constants in the model is the same as previous section and is: $x_0 = 2$ for the dimensionless size of the core. $\Lambda = 4$ for the overall constant and $-\log(c') = -2.6$ for the constant on T_{ij} .

The only change in the interactions, compared to section 6, is in the fermionic determinant for which we do the following change

$$\left(\det(\hat{\mathbf{T}}(x_L, x_{\bar{L}}, \bar{\nu}))\right)^2 \rightarrow \left(\det(\hat{\mathbf{T}}(x_L, x_{\bar{L}}, \bar{\nu}))\right) \left(\det(\hat{\mathbf{T}}(x_M, x_{\bar{M}}, \nu))\right), \quad (165)$$

where x_i are the positions of all i dyons.

The simulation has been done using standard Metropolis algorithm. An update of all $N = 64$ or 128 dyons corresponds to one cycle. Each run consists of 3000 cycles. Free energy is measured by the standard trick in eq. (115), involving integration over the interaction parameter from zero to one. The simulation was done on a S^3 circle, its volume is $V = 2\pi^2 r^3$: we use r in some places below.

The input “action parameter” S defines the instanton-dyon amplitude, and literally corresponds to the sum of the L and M dyon actions in semiclassical amplitude. In one loop approximation it is related to the temperature T by the asymptotic freedom relation

$$S = \left(\frac{11N_c}{3} - \frac{2N_f}{3}\right) \log\left(\frac{T}{\Lambda_T}\right). \quad (166)$$

In section 5 and 6 we approximately related the constant Λ_T to the phase transition temperature T_c : we do not do it in this section because there is no single phase transition in the theory we study now.

The varied parameters of the model include (1) The holonomy ν which is related to the Polyakov loop as $P = \cos(\pi\nu)$ and (2,3) The densities of M and L dyons n_M, n_L . After the free energy is found for each run, the values of these parameters, corresponding to its minimum, are fitted and used.

Other parameters include (4) The Debye mass, which is used to describe the falloff of the fields: its value is kept “self consistent” by a procedure explained in section 5.7. Finally we mention (5) the auxiliary interaction variable which is then integrated in order to obtain the free energy F .

The organization of the numerical sets were done as follows. An initial survey found the areas of interest, corresponding to minima of the free energy and most important variations of the results. Then the final set of simulations has been performed: its parameters are summarized in the Table 5. In total 1170000 individual runs were done for the final set of data, from which the plots were made.

The main part of the data analysis consists of finding the minima of the free energy and getting the Debye mass self consistent. To do the former

	Min	Max	Step size
λ	0	0.1	1/90
λ	0.1	1.0	0.1
ν	0.05	0.55	0.025
r	1.2	1.8	0.05
N_M	3	18	2
M_d	1	3.5	0.5
S	5	9.5	0.5

Table 5: The input parameters used for the final set of simulations. The step sizes given are some standard ones: yet some areas were given extra attention. For example around $N_M = 4$ where the step size was 1.

we fit data sets for the free energy near its minima with a 2-dimensional parabola

$$f = (w - w_0)M(w - w_0) + f_0, \quad (167)$$

which has 6 variables. w and w_0 are 2D vectors with w containing the variables holonomy ν and radius r and w_0 describing the position of the minimum. M is a 2 times 2 matrix with $M = M^T$ containing the coefficients for the fit.

The fit was done on free energy values of $5^2 = 25$ points from a square, containing 5 points around the minimum. The 6 parameters from the fit are used as follows:(i) w_0 and its uncertainties give the values of densities and holonomy at the minimum, plotted as results below; (ii) the diagonal component of M in the holonomy direction was converted into the value of the Debye mass M_d . An additional requirement of the procedure, to make the ensemble approximately self-consistent, is that the Debye mass from the fit should be within ± 0.25 of the used input Debye mass value.

To obtain the chiral properties, such as the Dirac eigenvalue distributions and its dependence on the amount of dyons and volume, we only used the “dominant” configurations for each action S.

The results reported below, compare new results, for Z_2 -symmetric QCD explained above, to the “old” ones, from section 6.5.1, for $N_c = N_f = 2$ QCD with antiperiodic fundamental quarks.

7.3 The holonomy potential and confinement

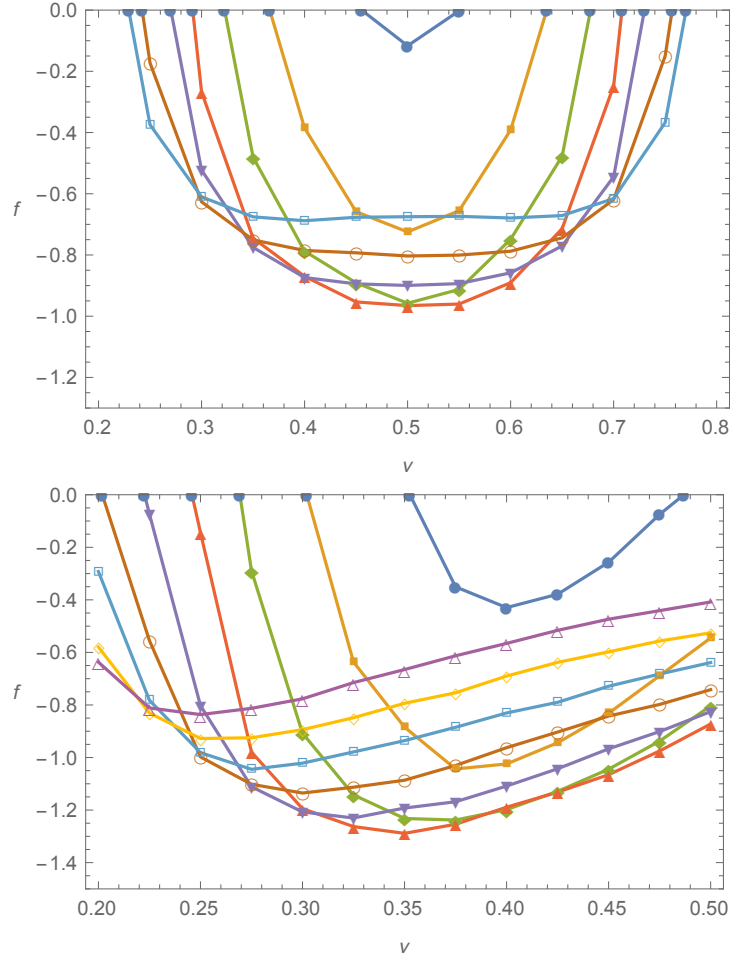


Figure 44: Free energy density as a function of the holonomy parameter ν . The upper plot is for the Z_2 -symmetric model and lower plot is for the model in which all quarks are anti-periodic. Different curves are for different dyon densities. The densities are $(0.47, \bullet)$, $(0.37, \blacksquare)$, $(0.30, \blacklozenge)$, $(0.24, \blacktriangle)$, $(0.20, \blacktriangledown)$, $(0.16, \circ)$, $(0.14, \square)$, $(0.12, \diamond)$, $(0.10, \triangle)$. Not all densities are shown. In both cases the action parameter is $S = 8.5$, and both dyon types are equally represented $n_M = n_L$. Note the dramatic difference of the holonomy potentials for these two cases: the Z_2 potential is symmetric (for equal dyon densities), while the periodic quarks produce an asymmetric minimum, and thus slide smoothly towards smaller holonomies (to the left) as the dyon density decreases.

The free energy density obtained from the simulations are shown in Fig. 44 as a function of the holonomy value. Both for standard (lower plot) and Z_2 -symmetric QCD (upper plot). At high density of the dyons one finds a symmetric minimum for the Z_2 -symmetric model. As the density decreases, one finds behavior very different from both that of the quenched case (no quarks) with two minima or in standard QCD, with broken center symmetry.

While symmetry remains intact, with the decreasing density (larger S) the minima of the potential become very flat and wide. (A slight appearance of the minima can be seen for the smallest density which is not nearly as strong as in the quenched case). We interpret this as an appearance of a large domain of “mixed phase”, a coexistence of many different configurations with different properties and different ν , but degenerate free energy. The confining minimum in the middle is also found to be dominant for much larger range of densities.

Translating the location of the minimum to the mean Polyakov line, we plot the results in Fig. 45. It shows that while the two models under consideration have very similar behavior at high densities of the dyons (smaller S or the left side of the plot), in the Z_2 -symmetric model there appears a strong jump in P , from about 0.2 to 0.6. Note that the intermediate point with large error bar should be interpreted not as an uncertainty of the value, as the usual error bar, but rather as reflection of the fact that in the ensemble the intermediate values of P are all feasible, due to flatness of the holonomy potential. In other words, this point is rather a vertical part of the curve, indicative of strong first-order transition. This conclusion is consistent with lattice studies in [36] for $SU(3)$, in which the authors show some hysteresis curve for P , with a similar strong jump.

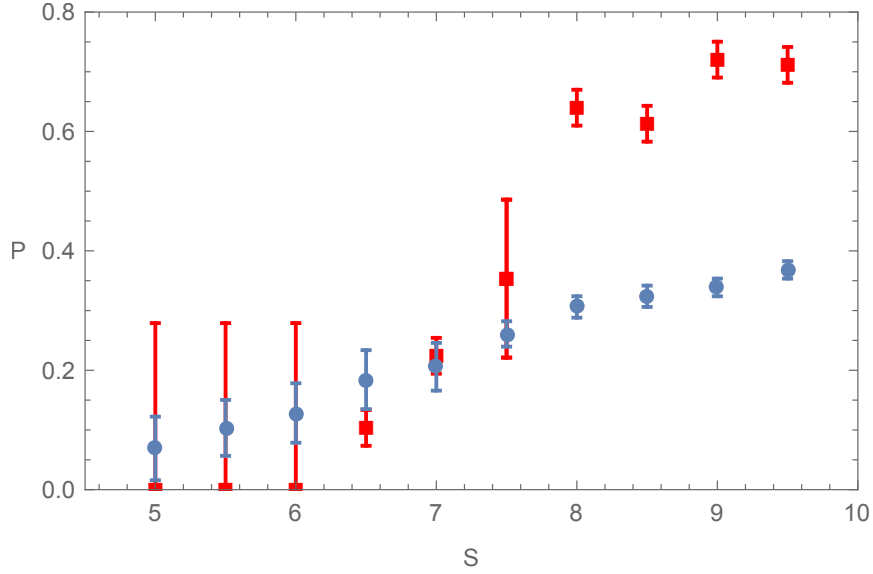


Figure 45: The mean Polyakov loop P as a function of action parameter $S = 8\pi^2/g^2$, for Z_2 -symmetric model (red squares), compared to that for the $N_c = N_f = 2$ QCD with the usual anti-periodic quarks (blue circles).

The densities of the dyons in both models are shown in Fig. 46. The upper plot for the Z_2 -symmetric model display a very symmetric confining phase at the l.h.s. of the plot (small S , dense ensembles) complemented by very asymmetric composition of the ensemble at the r.h.s. The usual QCD-like model with $N_c = N_f = 2$ in the plot below shows that the $L - M$ symmetry never holds, due to only L-dyons coupling to the zero modes, while the overall dependence on S is much less significant.

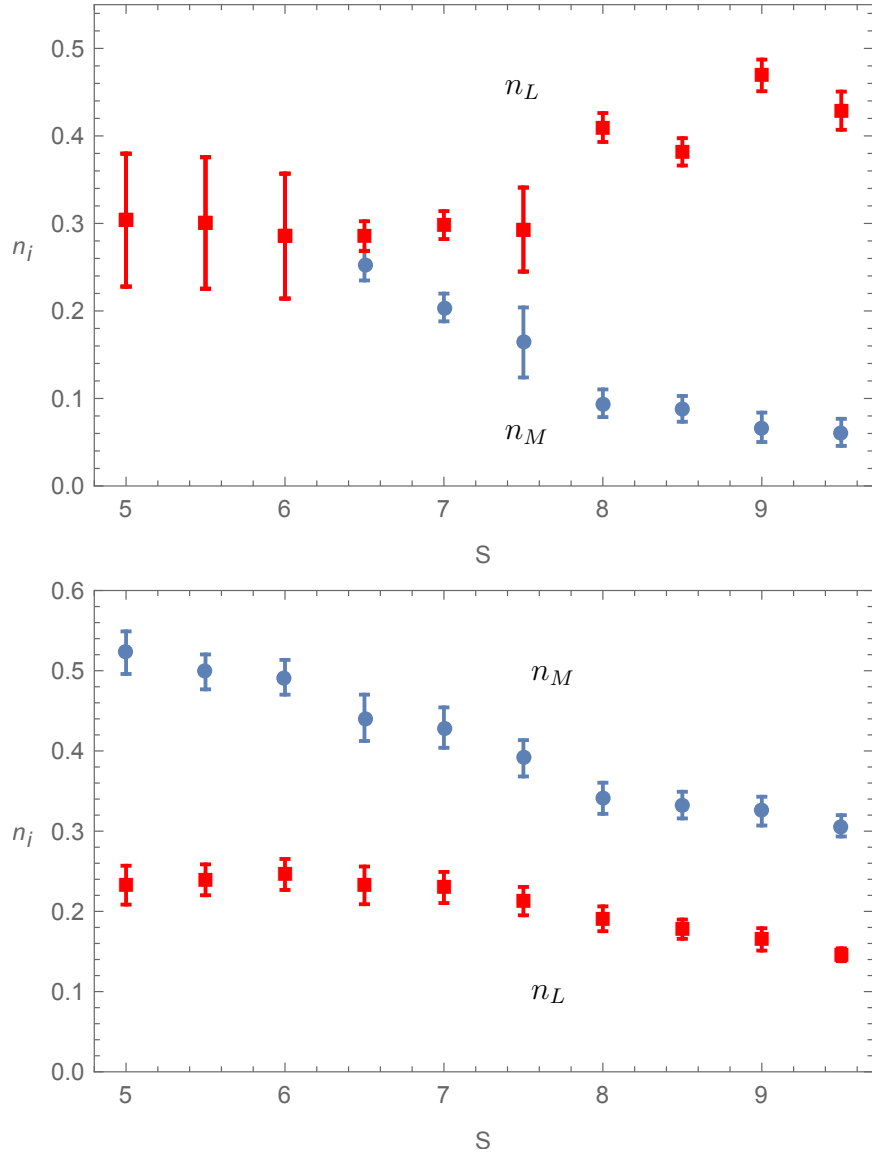


Figure 46: (upper) Densities of L dyons (red squares) and M dyons (blue circles), as a function of action parameter $S = 8\pi^2/g^2$, for the Z_2 -symmetric model. (lower) the same for the usual QCD-like model with $N_c = N_f = 2$ and anti-periodic quarks.

Lastly, the Debye mass, defined via the second derivatives of the effective

potential at the minimum, has been determined and plotted in Fig. 47, again for both models. For the Z_2 -symmetric model its values are significantly lower than for the QCD-like model. Smaller mass indicate flatter potential and stronger fluctuations.

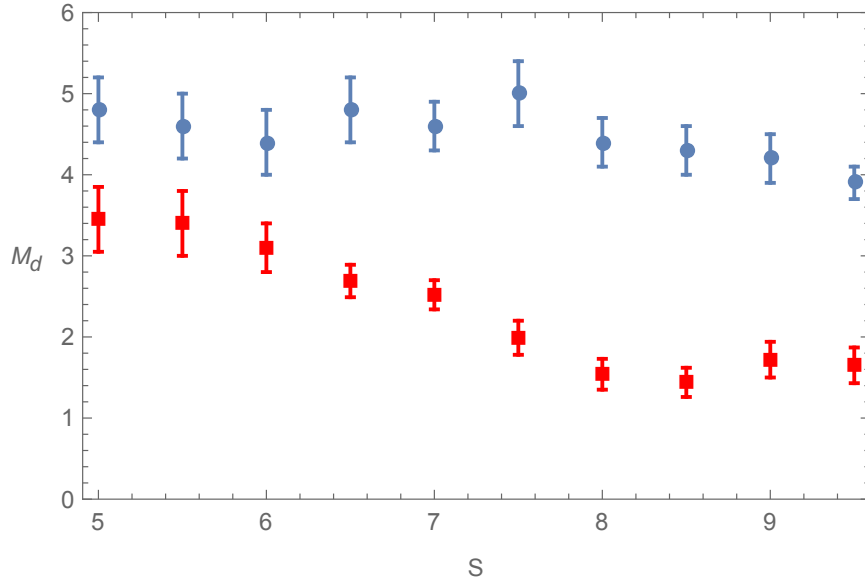


Figure 47: Debye Mass M_d as a function of action parameter $S = 8\pi^2/g^2$, for the Z_2 -symmetric model (red squares) and the usual QCD-like model with $N_c = N_f = 2$ (blue circles).

7.4 Chiral symmetry breaking

As we already explained above, the main feature of the Z_{N_c} -symmetric model with $N_f = N_c$, is that it distributes all types of quarks evenly, so that each type of dyon possesses zero modes with one quark flavor. This is in contrast to the usual QCD, in which all quarks are antiperiodic and thus all have zero modes only with twisted L -type dyons.

The simplest examples considered in this section are two $N_c = N_f = 2$ theories, the Z_2 -symmetric model and the two color QCD. In the former case the partition function includes two independent fermionic determinants, one for M and one for L dyons, with a single quark species each. In the latter,

one has a square (two-species) of the determinant of hopping matrix over the L -dyons only.

Here we remind well known facts about chiral symmetry breaking in such cases, and the consequences for such determinants. Theories with a single quark flavor have only a single $U_A(1)$ symmetry, broken explicitly by the fermionic effective action. Indeed, it includes terms $\bar{\psi}_L\psi_R$ or $\bar{\psi}_R\psi_L$ directly coupling components with opposite chiralities. So, there are no chiral symmetries to break, and condensates are always nonzero, proportional to density of the topological objects.

The case with two or more flavors is different: There is the $SU(N_f)$ flavor symmetry, which can be either broken or not, depending on the strength of the $2N_f$ -quark effective interaction.

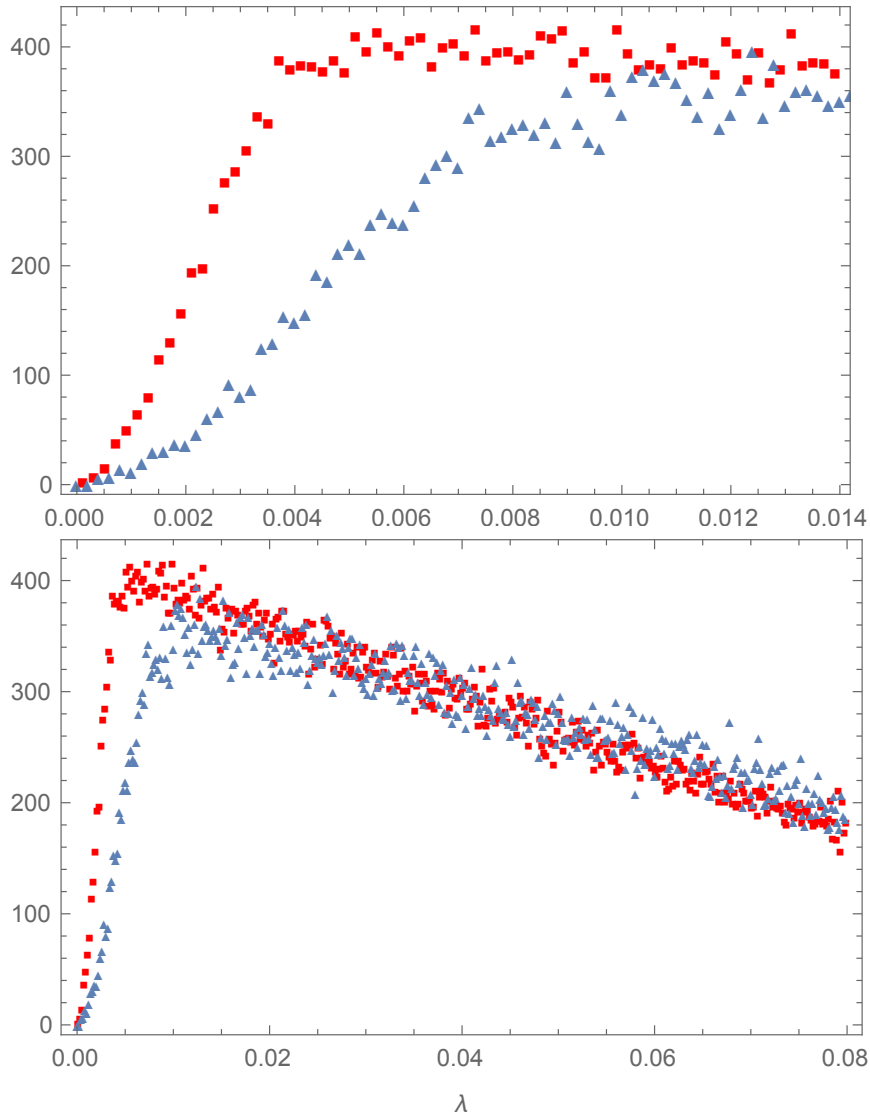


Figure 48: The Dirac eigenvalue distribution $\rho(\lambda)$ for ensembles of 64 (Blue triangle) and 128 (Red square) dyons, for the Z_2 -symmetric model at $S = 6$. The upper plot shows the region of smaller eigenvalues, in which one can see the finite volume “dip”, of a width which scales approximately as $1/V_4$ as expected. The lower plot shows the same data sets, but in a wider range of eigenvalues: it displays the “inverse cusp” shape of the distribution discussed in section 7.4.1.

7.4.1 Dirac eigenvalue distribution

Differences in chiral breaking mechanisms in these two models, indicated above, also manifest themselves in the Dirac eigenvalue distribution.

For $SU(N_f)$ flavors with $N_f \geq 2$ a general Stern-Smilga theorem [52] states that the eigenvalue distribution at small λ has the so called “cusp” singularity

$$\rho(\lambda) = \frac{\Sigma}{\pi} \left(1 + \frac{|\lambda|\Sigma(N_f^2 - 4)}{32\pi N_f F_c^4} + \dots \right). \quad (168)$$

For $N_f > 2$ the coefficient is positive, this is known as “direct cusp”, and was also observed, both on the lattice and in the instanton models. In the particular case $N_f = 2$ this cusp is absent: this fact can be traced to the absence of symmetric d^{abc} structure constant in the case of $SU(2)$ group. Indeed, both the calculations done in the instanton liquid framework (for examples and references see [9]) and in section 6 of the $N_f = 2$ theory had produced “flat” eigenvalue distribution

$$\rho_{N_f=2}(\lambda) \sim \text{const.} \quad (169)$$

In the $N_f = 1$ case the distribution have a singularity at $\lambda = 0$ of the form of the “inverse cusp”, $\sim -|\lambda|$. The Stern-Smilga derivation does not apply, but the theorem has been rederived for general N_f using partially quenched chiral perturbation theory in [53].

Our results for the Z_{N_c} -QCD under consideration shown in Fig. 48 also show the “inverse cusp” with linear behavior of $\rho(\lambda)$. (We use this fact to extrapolate $\rho(\lambda)$ to $\lambda \rightarrow 0$ and to extract the value of the quark condensate and the value of the coupling constant F_c .) In the other model, the $N_c = N_f = 2$ QCD, such “inverse cusp” is absent, see section 6.

So far our discussion assumed an infinite volume limit, in which case the Dirac eigenvalue spectrum extends till $\lambda = 0$. However, it is well known that any finite-size systems, with 4-volume V_4 , have the smallest eigenvalues of the order $O(1/V_4)$. This creates the so called “finite size dip”, in the eigenvalue distribution, also clearly visible in Fig. 48(upper). One can see that doubling of the volume, from 64 to 128 dyons at the same density, reduces the width of this dip roughly by a factor two, as expected.

As the holonomy jumps away from its confining value 0.5, the dyon densities become different. Unlike the fundamental quarks, where the holonomy goes down, the densities of L dyons become larger than that of M dyons. The total density goes down, but the reduction in M dyons leaves space for a few more L dyons. This means that on one hand the density is larger for L dyons, and the zero mode density is therefore higher. On the other hand, the factor in the exponential in T_{ij} (eq. (164)) is $\bar{\nu} = 1 - \nu$ for L dyons, and ν for M dyons. This means that as ν becomes smaller, the effective density of the zero modes associated with L dyons become smaller, while the zero modes associated with M dyons get an increased effective density. It is therefore the interplay between these two effects, that control which of the condensates are largest. This results in what we show in Fig. 49, where the M dyon condensate appears to be slightly larger than the L dyon condensate, and both condensates decrease slightly in accordance with the total density of dyons. It is also observed that each gas of zero modes effectively works as a $N_f = 1$ ensemble, with non-vanishing condensates even at the lowest densities we studied ¹ (the r.h.s. of the plot). The standard model, $N_c = N_f = 2$ QCD, has a condensate shown by black triangles: it clearly has chiral symmetry restoration: At $S > 8$ we detected no presence of a condensate.

¹It should be noted that the chiral condensate is harder to study, as the amount of dyons in the simulation becomes small, which happens for M dyons when there is a large asymmetry in the density. This explains the larger error bars for one of the condensates and why we stopped our studies at those particular parameters.

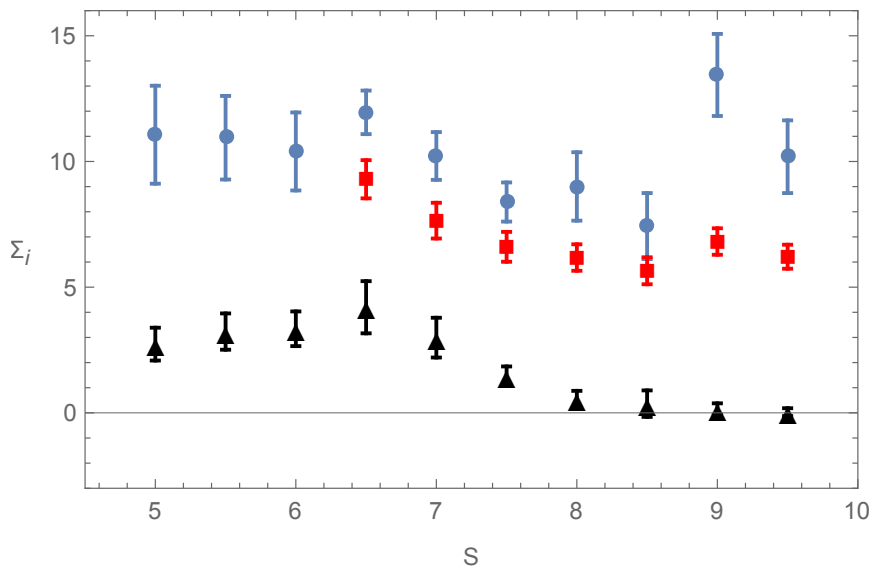


Figure 49: Chiral condensates Σ_i generated by u quarks interacting with L dyons (red squares) and d quarks interacting with M dyons (blue circles) as a function of action $S = 8\pi^2/g^2$, for the Z_2 -symmetric model. For comparison we also show the results from section 6.5.1 for the usual QCD-like model with $N_c = N_f = 2$ (black triangles).

The coupling constant F_c (Fig. 50), obtained from the slope of the eigenvalue distribution and Smilga-Stern theorem (168), is nearly density-independent: it changes by a factor of around 1.5 from $S = 5$ to $S = 9.5$. This is consistent with the behavior of the quark condensates, and similarly indicate that in the Z_2 model the chiral symmetry does not show tendency to be restored.

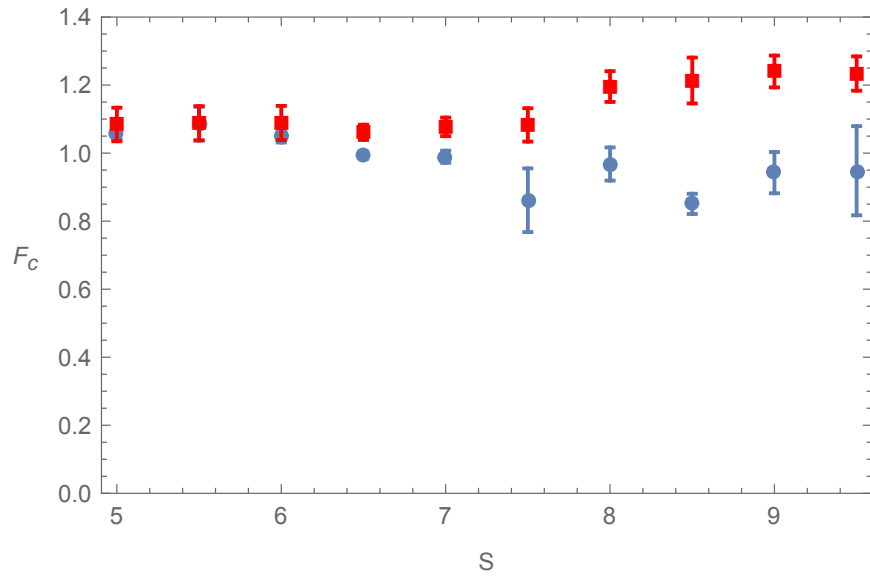


Figure 50: Coupling constant F_c from eq. (168) for the M dyon ensemble (blue circle) and the L dyon ensemble (red square) as a function of action $S = 8\pi^2/g^2$, for the Z_2 -symmetric model.

8 Conclusion

We have made an interacting ensemble of instanton-dyons for two colors and up to two quark flavors. In order to do the simulation, we first found the classical interactions for dyons with antidyons, a result that has no analytic solution. We used the streamline approach, where a dyon and an antidyon is placed a distance away from each other on a lattice, and then "cooled" such that the configuration flows towards smaller action. This showed that the dyon-antidyon classical interaction has a minimum around the size where the cores overlap, while quickly repelling away from each other when overlapping strongly. The long range was also seen to change as one over distance $1/r$ when the dyons were far from each other. As $r \rightarrow \infty$ the action approached that of two individual dyons. Due to the scale invariance of this setup, the solution was done for one specific holonomy (Polyakov loop), which then can be scaled for any value needed.

This result was important for the interacting instanton-dyon ensemble, where we attempted to explain the confinement-deconfinement transition. In the interacting instanton-dyon ensemble we used Monte-Carlo sampling for 64 interacting dyons, in order to obtain the free energy density as a function of temperature. From the free energy density we found the most likely value of the Polyakov loop P and dyon densities, also as a function of temperature.

The first ensemble was done for the quenched case (no fermions). It was seen that the repulsive core that scaled with the holonomy forced the M and L type dyons toward the same size and density, due to the symmetry $n_M \leftrightarrow n_L$ and $\nu \leftrightarrow \bar{\nu} = 1 - \nu$, which is center symmetry for $SU(2)$. For low densities the dyon interactions are not important and the dominating configuration comes mostly from minimizing the GPY potential (the energy cost of including a non-zero expectation value of A_4). At high densities (low temperature) the increased contribution to the free energy from the entropy was maximized by $\nu = 0.5$ ($P = 0$), thus causing confinement.

The next step was to include fermions. This was done with $N_f = 2$ flavors and $N_c = 2$ colors. The fermions was included through the fermionic zero mode interactions, which come from corrections to the fermionic eigenvalues, since the vacuum is not self-dual or anti-self-dual. From the corrections we also obtained the low energy eigenvalues, which was used to find the chiral condensate, the order parameter for chiral symmetry breaking. To obtain the chiral condensate we used results from random matrix theory [34], which

gave us finite volume effects.

The interacting ensemble showed us the reason why confinement and chiral symmetry breaking happens around the same temperature. As temperature decreases, the action of the dyons decrease. This increases the dyon density, which forces the Polyakov loop towards zero and the holonomy of L dyons $\bar{\nu}$ from 1 towards 0.5. This increases the range of the fermionic zero modes, since the fermionic zero modes fall off as $\exp(-\bar{\nu}r/2)$. The decreased value of the Polyakov loop therefore greatly increases the effective density of the zero modes, which becomes large enough for a non-zero chiral condensate. One can therefore say that confinement enhances the phenomena that create chiral symmetry breaking.

Last, we looked at the boundary conditions of the fermions. Lattice results have shown that this can dramatically change the confinement and chiral symmetry transitions. If dyons truly are responsible for these phenomena, then the ensemble of dyons should be able to describe this change. In terms of dyons, the fermionic boundary conditions dictate which dyon has the zero mode. We decided to work with the case of Z_2 -fermions, which have one periodic and one antiperiodic fermion, such that the M dyons had one flavor of zero modes and L dyons the other flavor of zero modes. We found that the confinement transition was an abrupt transition due to the restoration of center symmetry, which standard fermions break, but is restored for Z_N -fermions. The two chiral condensates, one for each flavor of fermions, stayed non-zero for all temperatures by balancing the densities with their respective holonomies ν and $\bar{\nu}$. Similar results was found on the lattice in [36] for $SU(3)$.

Dyons therefore give a good physical interpretation of these phenomena. It should though be mentioned that this does not mean that everything is known, as the precision in the model is still not too high, making more precise quantities impossible to extract. First step towards a more precise model has been done in my new paper with Edward Shuryak [54]. In this paper we explored correlation functions from a random ensemble of dyons. We here saw how corrections to the fermionic zero modes from L dyons overlapping with M dyons are important. A future study of the interacting instanton-dyon ensemble should therefore also include this effect.

References

- [1] R. Larsen and E. Shuryak, Nucl. Phys. A **950**, 110 (2016) doi:10.1016/j.nuclphysa.2016.03.013 [arXiv:1408.6563 [hep-ph]].
- [2] R. Larsen and E. Shuryak, Phys. Rev. D **92**, no. 9, 094022 (2015) doi:10.1103/PhysRevD.92.094022 [arXiv:1504.03341 [hep-ph]].
- [3] R. Larsen and E. Shuryak, Phys. Rev. D **93**, no. 5, 054029 (2016) doi:10.1103/PhysRevD.93.054029 [arXiv:1511.02237 [hep-ph]].
- [4] R. Larsen and E. Shuryak, Phys. Rev. D **94**, no. 9, 094009 (2016) doi:10.1103/PhysRevD.94.094009 [arXiv:1605.07474 [hep-ph]].
- [5] A. A. Belavin, A. M. Polyakov, A. S. Schwartz and Y. S. Tyupkin, Phys. Lett. **59B**, 85 (1975). doi:10.1016/0370-2693(75)90163-X
- [6] S. Vandoren and P. van Nieuwenhuizen, arXiv:0802.1862 [hep-th].
- [7] G. 't Hooft, Phys. Rev. D **14**, 3432 (1976) Erratum: [Phys. Rev. D **18**, 2199 (1978)]. doi:10.1103/PhysRevD.18.2199.3, 10.1103/PhysRevD.14.3432
- [8] G. 't Hooft, Phys. Rept. **142**, 357 (1986). doi:10.1016/0370-1573(86)90117-1
- [9] T. Schfer and E. V. Shuryak, Rev. Mod. Phys. **70**, 323 (1998) doi:10.1103/RevModPhys.70.323 [hep-ph/9610451].
- [10] M. Denissenya, L. Y. Glozman and C. B. Lang, Phys. Rev. D **91**, no. 3, 034505 (2015) doi:10.1103/PhysRevD.91.034505 [arXiv:1410.8751 [hep-lat]].
- [11] M. Denissenya, L. Y. Glozman and C. B. Lang, Phys. Rev. D **89**, no. 7, 077502 (2014) doi:10.1103/PhysRevD.89.077502 [arXiv:1402.1887 [hep-lat]].
- [12] M. Wagner, Phys. Rev. D **75**, 016004 (2007) doi:10.1103/PhysRevD.75.016004 [hep-ph/0608090].
- [13] F. Lenz, J. W. Negele and M. Thies, Annals Phys. **323**, 1536 (2008) doi:10.1016/j.aop.2007.11.009 [arXiv:0708.1687 [hep-ph]].

- [14] J. Greensite, *Prog. Part. Nucl. Phys.* **51**, 1 (2003) doi:10.1016/S0146-6410(03)90012-3 [hep-lat/0301023].
- [15] R. Hllwieser, M. Faber, T. Schweigler and U. M. Heller, *PoS LATTICE 2013*, 505 (2014) [arXiv:1410.2333 [hep-lat]].
- [16] B. J. Harrington and H. K. Shepard, *Phys. Rev. D* **17**, 2122 (1978). doi:10.1103/PhysRevD.17.2122
- [17] K. M. Lee and C. h. Lu, *Phys. Rev. D* **58**, 025011 (1998) doi:10.1103/PhysRevD.58.025011 [hep-th/9802108].
- [18] T. C. Kraan and P. van Baal, *Phys. Lett. B* **435**, 389 (1998) doi:10.1016/S0370-2693(98)00799-0 [hep-th/9806034].
- [19] P. M. Lo, *J. Phys. Conf. Ser.* **503**, 012034 (2014). doi:10.1088/1742-6596/503/1/012034
- [20] E. Poppitz, T. Schfer and M. nsal, *JHEP* **1303**, 087 (2013) doi:10.1007/JHEP03(2013)087 [arXiv:1212.1238 [hep-th]].
- [21] Y. Nambu, *Phys. Rev. D* **10**, 4262 (1974); S. Mandelstam, *Phys.Rep.* . **23C**, 145 (1976);
- [22] A. M. Polyakov, *Nucl. Phys. B* **120**, 429 (1977). doi:10.1016/0550-3213(77)90086-4
- [23] P. Gerhold, E.-M. Ilgenfritz and M. Muller-Preussker, *Nucl. Phys. B* **760**, 1 (2007) doi:10.1016/j.nuclphysb.2006.10.003 [hep-ph/0607315].
- [24] T. Schfer and E. V. Shuryak, *Phys. Rev. D* **53**, 6522 (1996) doi:10.1103/PhysRevD.53.6522 [hep-ph/9509337].
- [25] E. V. Shuryak and J. J. M. Verbaarschot, *Nucl. Phys. B* **341**, 1 (1990). doi:10.1016/0550-3213(90)90260-K
- [26] D. Diakonov, N. Gromov, V. Petrov and S. Slizovskiy, *Phys. Rev. D* **70**, 036003 (2004) doi:10.1103/PhysRevD.70.036003 [hep-th/0404042].
- [27] D. Diakonov, *Nucl. Phys. Proc. Suppl.* **195**, 5 (2009) doi:10.1016/j.nuclphysbps.2009.10.010 [arXiv:0906.2456 [hep-ph]].

- [28] J. J. M. Verbaarschot, Nucl. Phys. B **362**, 33 (1991) Erratum: [Nucl. Phys. B **386**, 236 (1992)]. doi:10.1016/0550-3213(92)90182-B, 10.1016/0550-3213(91)90554-B
- [29] J. B. Kogut, Phys. Lett. B **187**, 347 (1987). doi:10.1016/0370-2693(87)91107-5
- [30] F. Karsch and M. Lutgemeier, Nucl. Phys. B **550**, 449 (1999) doi:10.1016/S0550-3213(99)00129-7 [hep-lat/9812023].
- [31] G. Cossu, M. D'Elia, A. Di Giacomo, G. Lacagnina and C. Pica, Phys. Rev. D **77**, 074506 (2008) doi:10.1103/PhysRevD.77.074506 [arXiv:0802.1795 [hep-lat]].
- [32] E. Shuryak and T. Sulejmanpasic, Phys. Lett. B **726**, 257 (2013) doi:10.1016/j.physletb.2013.08.014 [arXiv:1305.0796 [hep-ph]].
- [33] P. Faccioli and E. Shuryak, Phys. Rev. D **87**, no. 7, 074009 (2013) doi:10.1103/PhysRevD.87.074009 [arXiv:1301.2523 [hep-ph]].
- [34] J. J. M. Verbaarschot, arXiv:0910.4134 [hep-th].
- [35] C. Gattringer, M. Gockeler, P. E. L. Rakow, A. Schafer, W. Soldner and T. Wettig, Nucl. Phys. Proc. Suppl. **106**, 492 (2002) doi:10.1016/S0920-5632(01)01757-1 [hep-lat/0110182].
- [36] T. Misumi, T. Iritani and E. Itou, PoS LATTICE **2015**, 152 (2016) [arXiv:1510.07227 [hep-lat]].
- [37] Michael E. Peskin, Daniel V. Schroeder, An Introduction To Quantum Field Theory, Westview Press, 1995
- [38] T. C. Kraan and P. van Baal, Nucl. Phys. B **533**, 627 (1998) doi:10.1016/S0550-3213(98)00590-2 [hep-th/9805168].
- [39] E. Shuryak and T. Sulejmanpasic, Phys. Rev. D **86**, 036001 (2012) doi:10.1103/PhysRevD.86.036001 [arXiv:1201.5624 [hep-ph]].
- [40] M. N. Chernodub, T. C. Kraan and P. van Baal, Nucl. Phys. Proc. Suppl. **83**, 556 (2000) doi:10.1016/S0920-5632(00)91737-7 [hep-lat/9907001].

- [41] F. Bruckmann, D. Negradi and P. van Baal, Nucl. Phys. B **666**, 197 (2003) doi:10.1016/S0550-3213(03)00531-5 [hep-th/0305063].
- [42] D. J. Gross, R. D. Pisarski and L. G. Yaffe, Rev. Mod. Phys. **53**, 43 (1981). doi:10.1103/RevModPhys.53.43
- [43] A. Cosnau, ScienceDirect 10.1016/j.procs.2014.05.072
- [44] E. V. Shuryak, Nucl. Phys. B **302**, 621 (1988). doi:10.1016/0550-3213(88)90191-5
- [45] F. Bruckmann, S. Dinter, E. M. Ilgenfritz, M. Muller-Preussker and M. Wagner, Phys. Rev. D **79**, 116007 (2009) doi:10.1103/PhysRevD.79.116007 [arXiv:0903.3075 [hep-ph]].
- [46] Y. Liu, E. Shuryak and I. Zahed, Phys. Rev. D **92**, no. 8, 085006 (2015) doi:10.1103/PhysRevD.92.085006 [arXiv:1503.03058 [hep-ph]].
- [47] V. G. Bornyakov and V. K. Mitrjushkin, Phys. Rev. D **84**, 094503 (2011) doi:10.1103/PhysRevD.84.094503 [arXiv:1011.4790 [hep-lat]].
- [48] A. Dumitru, Y. Guo and C. P. Korthals Altes, Phys. Rev. D **89**, no. 1, 016009 (2014) doi:10.1103/PhysRevD.89.016009 [arXiv:1305.6846 [hep-ph]].
- [49] V. Dick, F. Karsch, E. Laermann, S. Mukherjee and S. Sharma, Phys. Rev. D **91**, no. 9, 094504 (2015) doi:10.1103/PhysRevD.91.094504 [arXiv:1502.06190 [hep-lat]].
- [50] O. Kaczmarek and F. Zantow, Phys. Rev. D **71**, 114510 (2005) doi:10.1103/PhysRevD.71.114510 [hep-lat/0503017].
- [51] S. Borsnyi, Z. Fodor, S. D. Katz, A. Pisztor, K. K. Szab and C. Trk, JHEP **1504**, 138 (2015) doi:10.1007/JHEP04(2015)138 [arXiv:1501.02173 [hep-lat]].
- [52] A. V. Smilga and J. Stern, Phys. Lett. B **318**, 531 (1993). doi:10.1016/0370-2693(93)91551-W
- [53] J. C. Osborn, D. Toublan and J. J. M. Verbaarschot, Nucl. Phys. B **540**, 317 (1999) doi:10.1016/S0550-3213(98)00716-0 [hep-th/9806110].
- [54] R. Larsen and E. Shuryak, arXiv:1705.04707 [hep-ph].